Impact of Vacancies and Chemistry on Iron-based Electrodes for Alkali-ion Batteries

Zachary G. Neale

A dissertation
submitted in partial fulfillment of the
requirements for the degree of

Doctor of Philosophy

University of Washington

2020

Reading Committee:

Guozhong Cao, Chair
Jihui Yang
Bruce Hinds

Program Authorized to Offer Degree:
Materials Science and Engineering

University of Washington

Abstract

Impact of Vacancies and Chemistry on Iron-based Electrodes for Alkali-ion Batteries

Zachary G. Neale

Chair of the Supervisory Committee:
Guozhong Cao
Materials Science and Engineering

The exponential growth in population and worldwide prosperity during the last century is reciprocal with energy consumption. Recent environmentalism and government regulation have produced greater demand for green energies and electric vehicles. Associated with these technologies is growing demand for battery materials to support power grid operation and transportation. Conventional lithium ion batteries are at risk of supply instability of cobalt and lithium precursors, potentially making them economically unfit for certain applications. Iron-based materials for lithium-ion and sodium-ion batteries are an attractive alternative for niche applications and grid level storage due to their abundant and inexpensive precursors.

Material chemistry and structure have a strong influence on the electrochemical properties of battery electrodes such as redox potential and diffusion kinetics. Vacancy control via synthesis was investigated as a means of improving the kinetic and thermodynamic limitations of jarosite and iron hexacyanoferrate. Incorporation of divalent ions into the jarosite structure introduced cation vacancies that facilitated lithium-ion diffusion and reduced structural transformation. Cation chelation during synthesis of iron hexacyanoferrate retarded particle nucleation leading to highly crystalline structures with low vacancy concentration. Cation substitution of jarosite and

iron hexacyanoferrate was investigated for its beneficial electrochemical effects. Doping of iron hexacyanoferrate with zinc increased the redox activity of low-spin iron species, while doping of manganese increased the redox potential of high-spin iron species. These findings demonstrate the importance of materials chemistry, defects, and structure on the properties of electrode materials for alkali-ion batteries, and the same fundamentals able to be implemented in other electrochemical material systems.

Published and Submitted Papers

This dissertation largely takes from the following papers published or under review. The individual publishers explicitly allow for the reproduction of these works for this dissertation.

Neale, Z. G.; Liu, C.; Cao, G. Effect of synthesis pH and EDTA on iron hexacyanoferrate for sodium-ion batteries. *Sustainable Energy & Fuels* **2020**, 4 (6), 2884–2891. https://doi.org/10.1039/d0se00120a.

Neale, Z. G.; Barta, M. L.; Cao, G. Faster diffusion and higher lithium-ion intercalation capacity in Pb-jarosite than Na-jarosite. *ACS Applied Energy Materials*, Under Review, Submitted November 5th, 2020.

Contents

Chapter 1: Context

1.1 Global Energy and Prosperity

Prosperity is highly dependent on energy availability. In the most rudimentary sense, energy in the form of food is a limiting factor in population growth of all species. Species of all types have aggregated and relocated around sources of food and energy. Humans, being a technologically advanced species, have learned to harness energy in the form of heat and electricity, and its transformation into work which has resulted in several revolutionary eras leading to population booms.

Global energy consumption and world population are strongly related and rapidly increasing. Primary energy consumption, which includes electricity, transportation, and heat, has steadily increased nearly 2.5 petawatt hours per year between 1999 - 2019. Despite this, 13% of the world still does not have access to electricity as of 2016, and per capita electricity consumption varies over 100-fold among different nations.[1,2] In general, more affluent counties have higher energy consumption per capita; however, it is difficult to discern if readily available energy encourages economic growth or if economic growth leads energy consumption. Economic growth and its relation to energy consumption is different between developing and developed nations (**Figure 1-2**). Largely, nations with less than 100% access to electricity show proportional growth in per capita energy consumption and per capita GDP. In contrast, nations that have near ubiquitous access to electricity have shown a reversal in per capita energy consumption in recent years. The decrease in energy consumption per capita for wealthier nations could reflect changes in society such as more efficient appliances and transportation, shrinking manufacturing sector, governmental restrictions on energy use, and increasing societal attention to environmental impact.

Throughout history energy consumption had been provided through burning of biomass fuels for light and heat. However, the discovery and utilization of fossil fuels for energy has dominated the rapid rise in energy consumption since the beginning of the 20th century (**Figure 1-3a**). Coal, oil, and gas accounted for 86% of global energy consumption in 2019, equating to 136.7 petawatt hours.[3] The burning of hydrocarbons to meet energy demands remains necessary for many nations for increasing economic opportunity and prosperity due to its availability, reliability, and cost.

However, the massive use of hydrocarbons has resulted in latent and emerging consequences to health and environment. Pollution-caused disease was estimated to be responsible for 16% of all deaths worldwide in 2015.[4] Air pollution contributes to at least five million premature deaths per year, of which 64% can be attributed to fossil fuels.[5] Additionally, burning of fossil fuels and biomass unleashes massive amount of CO_2 into the air. From 10,000 BCE to 1800 CE atmospheric CO_2 concentration increased from 249 to 283 ppm; however since then CO_2 concentration has increased to 409 ppm in 2018.[6] CO_2 concentration has naturally fluctuated throughout history over the course of thousands of years, allowing for gradual adaptation. The rapid increase in the last two centuries may pose a threat to the survivability of some species unable to quickly adapt, which may lead to more severe ecological problems. Furthermore, CO_2 and other anthropogenic emissions have been linked to increasing average global temperature due to the atmospheric greenhouse effect.[7] Increasing global temperature may lead to potential environmental and ecological threats such as severe weather disasters, perturbed crop growth, disrupted food chains, and rising sea-levels displacing costal populations.[8]

Today the world is conflicted between increasing economic prosperity with increased energy consumption and reducing anthropogenic emissions. An emerging solution has been the rapid growth in renewable energy generation from solar and wind. Solar and wind energy is growing exponentially at a faster rate than other energy sources (**Figure 1-3b**) and has increased over 600% in the last 10 years compared to only 16% from other sources.[3] The rapid growth of solar and wind energy could be attributed to developing technologies in these areas, decreasing cost of manufacturing, government subsidies and restrictions, and increasing societal demand for green energy sources. However, an inherent shortcoming of solar and wind energy is its intermittent operation. Solar energy, although plentiful, is limited to generating energy only during day time, and efficiency can be severely hampered by cloud cover. Similarly, wind energy is dependent on wind speed which is not constant. These drawbacks can be countered by pairing energy generation with energy storage systems, such as grid-level battery storage.

An unintended consequence of increasing grid-level energy from solar and wind is decreased efficiency of conventional steam power plants (i.e. coal, oil, and gas). During times that solar and wind energy are able to help supply energy to the grid, conventional power plants are operated at lower loads with lower efficiencies, thus increasing the amount of CO_2 per kWh produced. The same deficiency is found when daily energy demand switches between peak and low load throughout the day. A potential solution to this deficiency is the use of grid-level battery storage in conjunction with conventional power plants. This would allow for continuous optimal operation throughout the day. During times of low demand, power plants can be used to store energy into batteries. Battery stored energy can be utilized during times of peak demand, such as in the afternoon and evening or when there is insufficient solar and wind power.

Another area of rapid energy change is in transportation. Switching from internal combustion engines to battery powered motors in conjunction with carbon-free energy sources can help reduce CO_2 emissions. The number of electric vehicles has significantly increased rapidly in the last decade, increasing over 500% in annual global sales from 2014 to 2019 (**Figure 1-4**).[9] This is in part caused by improvements to battery energy density and lowered cost of manufacturing. However, continued viability and growth of electric vehicles is potentially threatened by the fragile stability of the supply chain for battery materials. A large part of this is the cost of cathode materials for electric vehicle batteries. It is estimated for a $LiNi_{1/3}Mn_{1/3}Co_{1/3}O_2$ (NMC333) lithium ion battery chemistry and given manufacturing quantity, the cathode is 20% of the total vehicle battery cost including processing and overhead, and 50% of that is from the raw materials alone.[10] Cobalt is the most high-risk component of cobalt-based battery chemistries due to high prices, political instability, and ethical concerns of cobalt mines.

In summary, global prosperity has rapidly improved during the last century with increasing energy consumption in all forms. Developing nations have decreased the populace living without access to electricity, improving livelihood and stimulating economic opportunities. Energy demand continues to grow exponentially, and with that the creation of anthropogenic emissions with potential environmental and ecological consequences. To meet the growing demand for energy, a variety of energy sources will be used in conjunction with energy storage systems such as batteries. Inexpensive batteries of various chemistries for different applications will be vital to future energy economy.

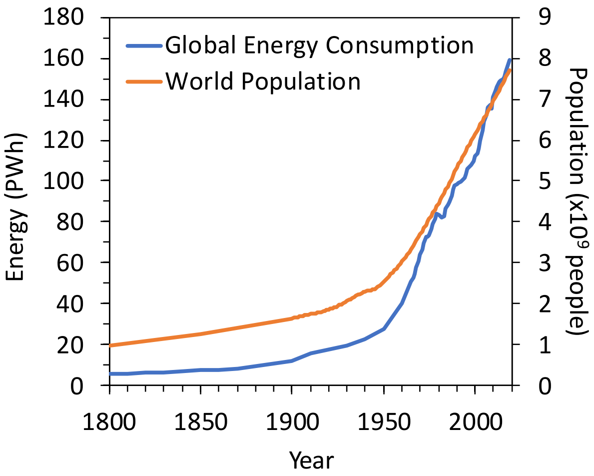

Figure 1-1. Global energy consumption in petawatt hours compared to world population in billions of people. Primary energy consumption includes electricity, heating, and transporation converted to units of kWh. Energy data published by Vaclav Smil (2017). Energy Transitions: Global and National Perspectives and BP Statistical Review of World Energy. Population data published by Gapminder, HYDE (2016) and United Nations Population Division (2019).

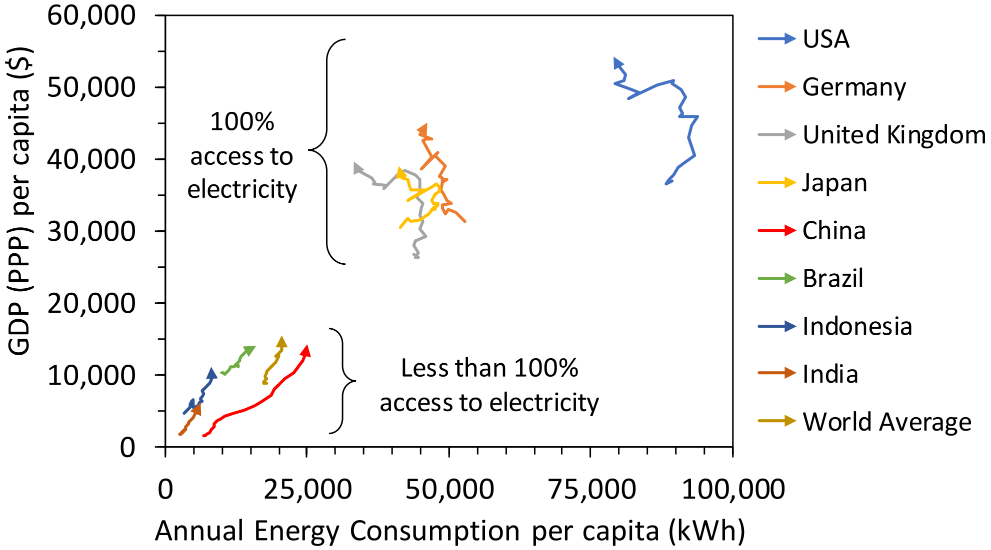

Figure 1-2. Gross domestic product (GDP) per capita of select nations versus annual energy consumption per capita between 1990 and 2017. Primary energy consumption includes electricity, heating, and transporation converted to units of kWh. Nations are catagorized into two groups: those with citizens that have 100% access to electricity since 1990, and those with less than 100% having access to electricity. China and Brazil achieved 100% access in 2015 and 2016. GDP per capita measured in 2011 international dollars based on purchasing power parity (PPP). GDP data published by World Bank – World Development Indicators. Energy consumption data published by BP Statistical Review of World Energy and provided by Our World in Data.

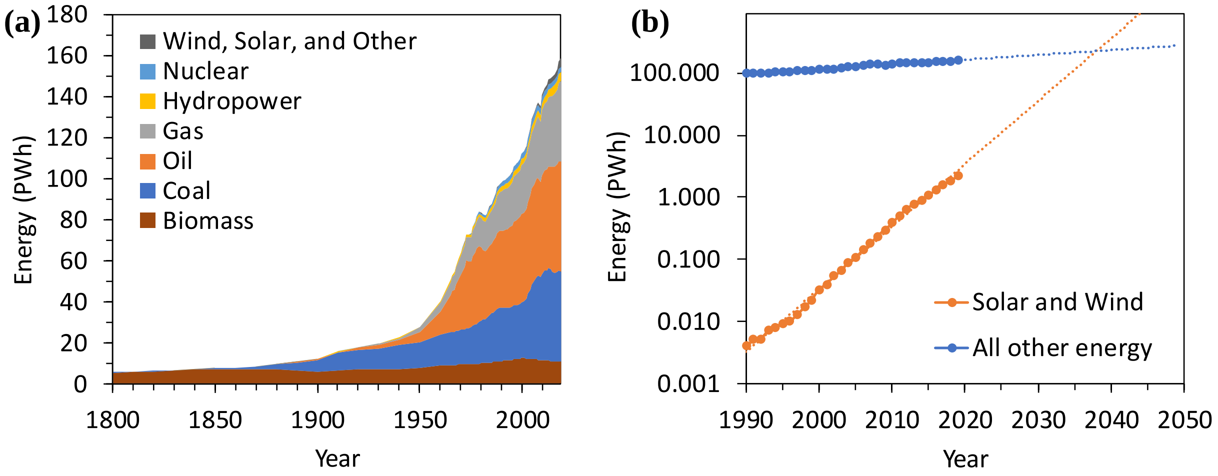

Figure 1-3. Global energy consumption by sector (a) and global energy consumption provided through solar and wind since 1990 with exponential projection (b). Energy in units of petawatt hours. Note logarithimic scale of y-axis in (b). Data published by BP Statistical Review of World Energy.

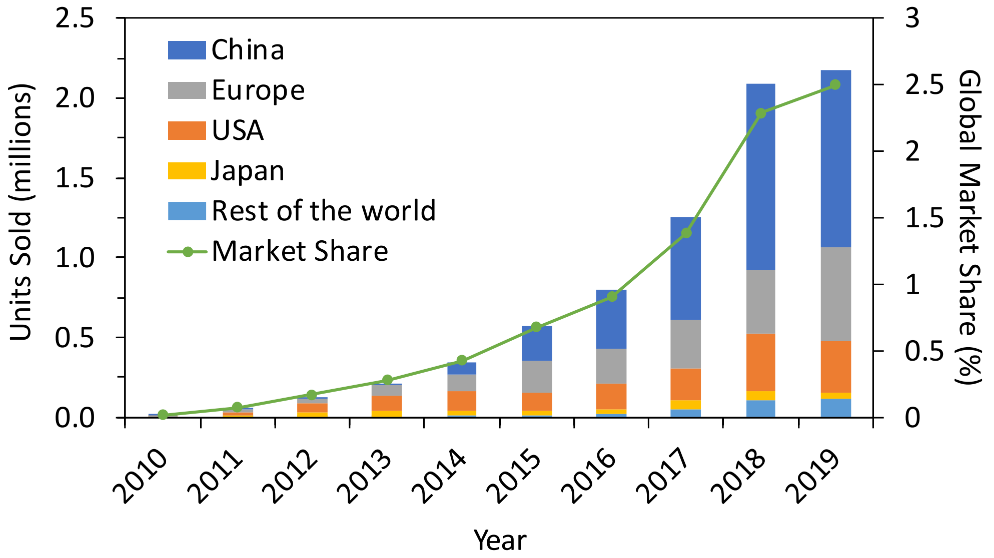

Figure 1-4. Global electric vehicles sold and percentage of market share annually between 2010 and 2019. Data published by IEA analysis based on IEA data and EV-volumes (2020).

1.2 Research Objective

There will not be a catchall battery chemistry that is economical or efficient for every application. Development of alternative battery chemistries is important to filling niche roles in the growing demand for energy storage. Iron-based battery electrodes is an attractive group of materials due to their low cost, low toxicity, and Earth abundant precursors. Despite iron's lower redox potential compared to other transition metal battery chemistries, the aforementioned reasons could still make iron-based electrodes economically competitive for applications such as residential power banks and some consumer electronics.

Crystal defects can hurt or enhance performance of battery materials. Understanding how defects can be mitigated, encouraged, and controlled in materials is important to improving their properties. Specifically, vacancies can affect ion diffusivity, redox potential, and structural stability of the crystal. Besides energy storage, the same materials could potentially be used in other electrochemical or catalytic devices in which defects can play an important role.

The objective of the following dissertation is to investigate the relationships between synthesis, chemistry, and electrochemical properties of two iron-based electrode materials. First, the polyanionic hydroxysulfate material, jarosite, is investigated as a non-aqueous lithium-ion battery cathode (Chapter 3). Cation vacancies are induced during synthesis by substituting monovalent Na^+ for divalent Pb^{2+}. Next is the investigation of iron hexacyanoferrate as a cathode for non-aqueous sodium-ion batteries. Polyanionic hexacyanoferrate vacancies are reduced by slowing particle nucleation using the chelating agent EDTA (Chapter 4). Then vacancy concentration of iron hexacyanoferrate is controlled by adjusting chelation strength through pH control (Chapter 5).

Chapter 2: Battery Background

2.1 Electrochemistry Fundamentals

Many transition metal ions can exist at several different valence states. For example, iron ions may exist as Fe^{2+} or Fe^{3+} in solution. If electrodes of the same material are being used to probe the reduction and oxidation reaction of iron ions in a hypothetical electrochemical cell containing 10 mM Fe^{2+} and 10 mM Fe^{3+} the cell potential would be measured as 0V because there is no chemical energy difference between the two electrodes, thus there is no thermodynamic driving force to make the reaction go one way or the other (**Figure 2-1a**). The two iron species are in equilibrium and no net concentration change will occur. On the other hand, if one of the electrodes is replaced with an electrode containing a different chemical environment that is separate from the Fe^{2+}/Fe^{3+} solution but ionically connected then a potential would develop between the two electrodes because of a difference in chemical potential energy between the two solutions. The cell voltage is equal to the difference in chemical potential at the electrodes divided by the charge of an electron,

$$V = \frac{\mu_a - \mu_c}{e} \tag{2-1}$$

where μ_a and μ_c is the chemical potential energy of the anode and cathode. The forward reaction indicates reduction at the cathode and oxidation at the anode.[11]

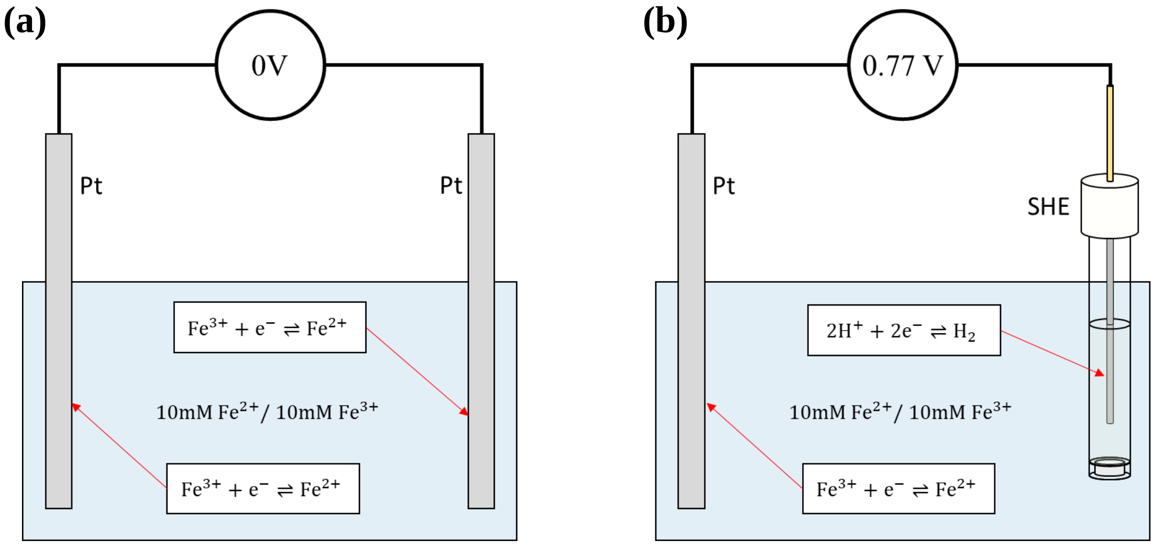

Figure 2-1. (a) Potential between two platinum electrodes and (b) between a platinum electrode and standard hydrogen electrode in a Fe^{2+}/Fe^{3+} solution.

Electrodes with standard chemistry such as the standard hydrogen electrode (SHE) are used as a reference to consistently measure voltages of other reactions. The standard reduction potential of metal ions and molecules at room temperature and pressure are measured against the SHE by convention but can easily be converted to other reference systems. Chemical species lower on the standard reduction potential chart in **Figure 2-2** have lower electrochemical potential energy (larger voltage vs SHE) and will become reduced by the oxidation of species higher on the chart. Similarly, adjusting the electrochemical potential of the platinum electrodes by use of an external power supply such as a battery will induce oxidation or reduction of species in solution. If the electrode potential is below that of the reduction potential of the ionic species then it will become reduced.

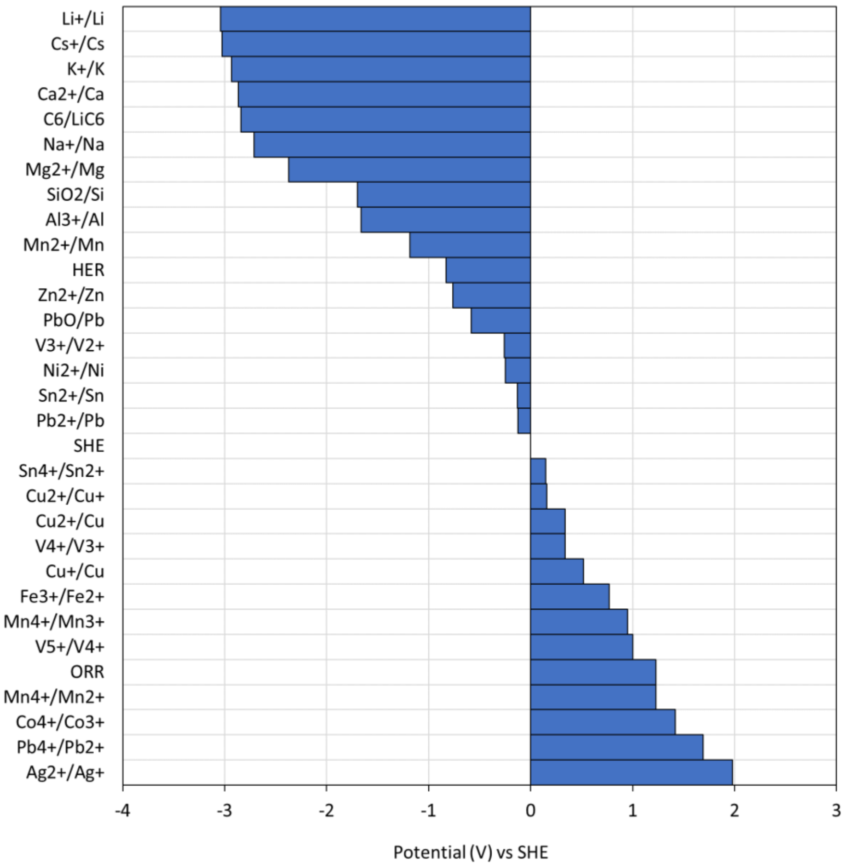

Figure 2-2. Standard reduction potentials of various metals and molecules.

Two essential requirements must be met for a redox reaction to take place. One is the transfer of electrons to or from the reaction. If the electrodes in **Figure 2-1b** are connected by a conductive wire there will be a net reduction of Fe^{3+} species at the platinum electrode and oxidation of hydrogen gas at the SHE. The second essential part for a redox reaction to occur is charge balance of the system. The entire electrochemical cell must maintain charge neutrality, i.e. the total charge of the system is zero. If the net charge of Fe ions decreases during reduction of Fe^{3+} to Fe^{2+} at the cathode, then positive charge must be maintained in the system by the dissociation of H_2 gas into H^+ ions at the anode. Similarly, when electrons are transferred to Fe^{3+} from the platinum electrode they must be replaced by electrons in the wire, which are replaced by electrons transferred from the oxidation of H_2 gas.

The activity of ion species and temperature will affect the free energy change and electrode potential of reduction through the Nernst equation;

$$E = E^o - \frac{RT}{zF} ln\, Q_r \tag{2-2}$$

where E is the electrode potential, E^o is the standard reduction potential, R is the universal gas constant, T is temperature, z is the number of electrons involved in the reaction, F is the Faraday constant, and Q_r is the ratio of the activities of products to reactants.[12] **Figure 2-3** illustrates the Nernst equation for the half-cell reduction potential of Fe^{3+}. As the concentration of reactants decreases so does the reduction potential. The standard reduction potential is the potential at room temperature when the concentration of products and reactants are equal.

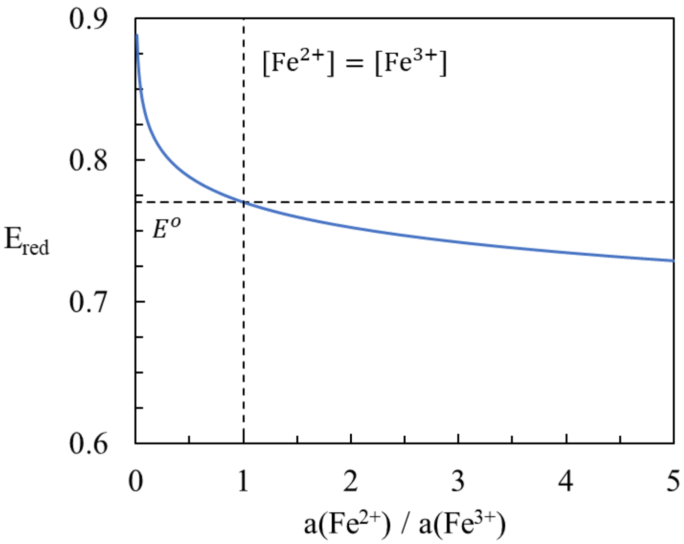

Figure 2-3. Half-cell reduction potential of Fe^{3+} versus reaction quotient. Horizontal dashed line is the standard electrode reduction potential.

To measure electrode potential against a reference electrode during an electrochemical test a 3-electrode cell is used. The cell setup involves a working electrode (WE), reference electrode (RE), and counter electrode (CE) as illustrated in **Figure 2-4**. Current only flows between the WE and CE, and potential is measured between WE and RE. This cell setup is used so that the chemistry of the reference cell does not change during the test, which would shift the reference potential. This is because no current passes between the WE and RE (actually there is a very negligible amount). The below example with platinum WE and CE submerged in 0.1M $FeCl_3$ solution is the same situation as in **Figure 2-1a**.

The equipment used to perform electrochemical tests is a potentiostat, which can control the current between the WE and CE and measure voltage between WE and RE separately. The most common types of test modes are potentiodynamic, potentiostatic, and galvanostatic. In potentiodynamic and potentiostatic tests the user prescribes how the WE-RE potential is controlled while measuring the current response between WE and CE. In actuality, the potentiostat machine controls current between WE and CE in order to maintain the prescribed WE-RE potential. For galvanostatic tests a constant current is applied between the WE and CE while the WE-RE voltage is measured.

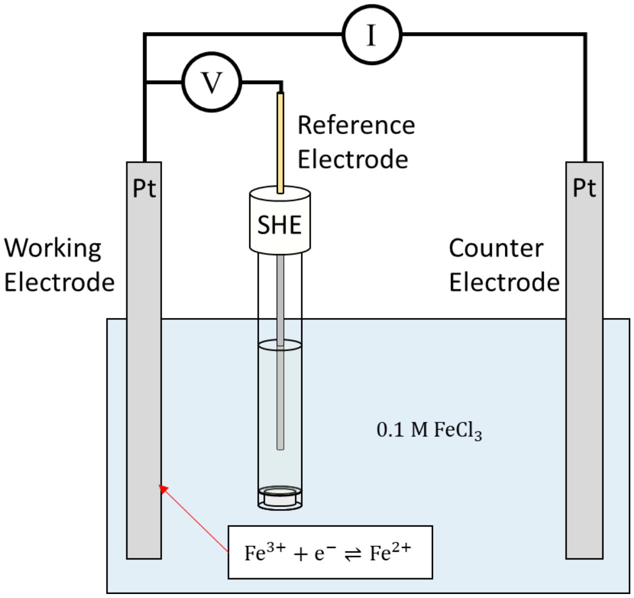

Figure 2-4. 3-electrode cell setup.

2.2 Battery Fundamentals

2.2.1 Architecture

In any electrochemical cell there exists three essential parts: (1) the cathode, (2) the anode, and (3) the electrolyte (**Figure 2-5**). In a battery it is necessary that the cathode and anode are electrically insulated from each other, otherwise they are in short-circuit and current flows between them. Therefore, a separator material is used between the cathode and anode to maintain electrical isolation, but also must maintain ionic connection.

A *full-cell* battery is one which the cell potential is affected by the state of charge of both the cathode and anode. As the battery discharges the cathode and anode chemistry may change drastically. In constructing a full-cell battery it is important to optimize the amount of cathode and anode material added such that the capacities of both sides match, otherwise anode or cathode material will be unutilized. Another challenge is that many materials are synthesized in a partially charged state which may require an additional chemical step to fully reduce or oxidize the material.

It is a widespread misconception that commercial rechargeable lithium-ion batteries contain lithium metal, instead they typically contain graphite as the anode. Non-rechargeable, or primary, lithium-ion batteries do however contain lithium metal as the anode. The problem with lithium metal anodes, as with other metal ion battery anodes, is dendrite growth over many cycles that may eventually lead to dangerous short-circuits. Although, there are emerging companies such as SolidEnergy Systems from Shanghai and Cuberg from California with the goal of creating rechargeable lithium metal batteries which would have an advantage in energy density but would require special liquid electrolytes or solid electrolytes to prevent lithium dendrite formation.

In battery research it is common to use lithium and sodium metal as the counter electrode when studying electrode materials for secondary lithium-ion and sodium-ion batteries. When these metals are used as anodes it is considered a *half*-cell battery. Research can afford to use lithium or sodium metal as a counter electrode because there is less liability of safety in non-commercial batteries, and the metal anode is suitable as a common reference electrode in order to make comparisons with other research. An excess amount of counter electrode is used compared to the working electrode active mass to guarantee that the electrode under study is the limiting capacity electrode.

A common half-cell testing setup for studying cathode or anode materials is a 2-electrode coin cell, or button cell. These cells are relatively easy to make and can provide reproduceable results. This cell design has two electrodes, the working electrode and the counter electrode. The counter electrode in a 2-electrode cell is also the reference electrode, usually the metal of the type of ion battery under study. The two electrodes are electrically isolated from each other by a separator and are ionically connected by excessive electrolyte. Porous films such as polypropylene and polyethylene membranes or glass fiber membranes are often used for lithium and sodium ion batteries. The porosity of the films allows ionic continuity of liquid electrolyte while maintaining electrical separation between anode and cathode. A disadvantage of this type of cell design is that there may be slight variations in reference potential unrelated to the working electrode during testing due to side reactions that take place at the counter electrode.

Another type of setup for testing half-cells is a 3-electrode cell setup as described in the previous section. The working electrode is the electrode under study with its potential measured

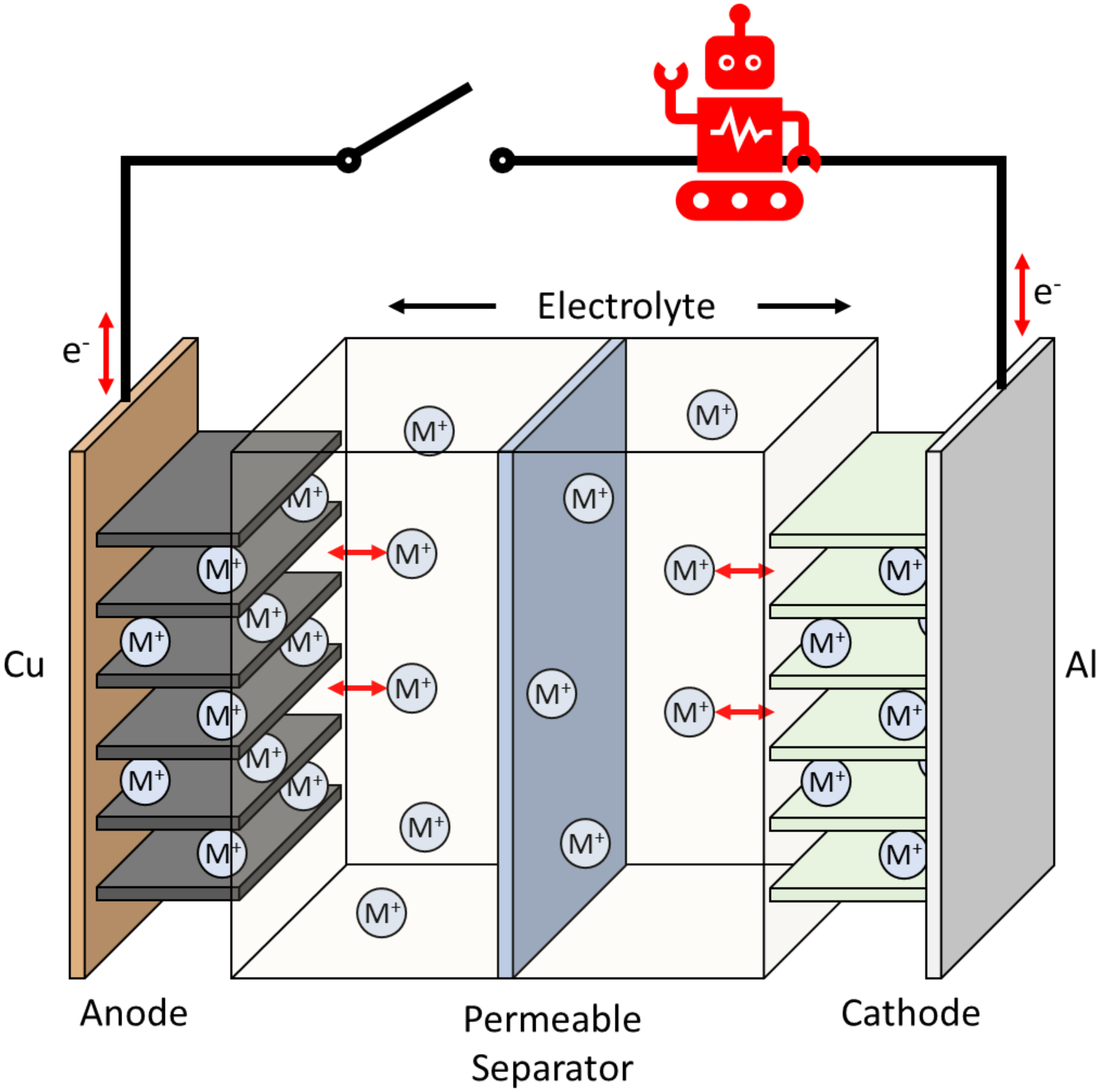

Figure 2-5. Diagram of a typical full-cell non-aqueous rechargeable monovalent ion battery.

relative to the reference electrode and its current measured against the counter electrode. An advantage of this setup is that no current passes through the reference electrode so its chemical state is unchanged during testing and can provide a constant reference potential. Typical reference electrodes include lithium or sodium metal in non-aqueous cells, or Ag/AgCl reference electrodes in aqueous cells. The counter electrode can be any material so long as it is able to provide enough current to or from the working electrode. Platinum is typically used as a counter electrode due to its chemical inertness and catalytic properties. However, it is important to consider the reactions occurring at the counter electrode that might change the chemistry of the electrolyte. For example, the counter electrode may be producing oxygen or hydrogen gas during testing which will affect the pH of the electrolyte. In most cases the change in electrolyte chemistry due to testing is minimal in comparison to the volume of solution used in a 3-electrode cell.

The selection of electrolyte is an important factor to the construction of batteries and may be restricted by the operating voltage. The solvent selected must not undergo oxidation or reduction at either of the electrodes. The solute also should not undergo reduction or oxidation for intercalation type materials. The electrolyte stability window has commonly been reported as the energy window between highest occupied molecular orbital (HOMO) and lowest unoccupied molecular orbital (LUMO). If the electrochemical potential is above the LUMO then reduction of the electrolyte will occur, and if it is below the HOMO then oxidation of the electrolyte occurs.[11] However, this definition of electrochemical stability should be used with caution as it does not always hold true. Peljo and Girault (2018) discuss their opinion on the misconception of using the HOMO-LUMO definition for electrochemical potential window.[13] The most obvious case that disagrees with this definition is that of liquid water electrolyte which has a HOMO and LUMO of -9.4 and -0.5 eV, respectively, corresponding to a voltage window between 5.5 and -3.9 V vs SHE (using -4.4 eV as the absolute energy level of SHE).[14] However, it is well known that the oxidation and reduction of water occurs well within these limits. On the other hand, the relation between LUMO energy and reduction potential of many organic solvents has been shown to be strongly linear.[15]

2.2.2 Redox Mechanisms in Battery Materials

There are three mechanisms for electrochemical charge storage in battery materials: (1) intercalation, (2) conversion, and (3) alloying. For materials containing transition metal ions the underlying principle in these mechanisms is the change in valence of metal ions. All three mechanisms require that charge neutrality is maintained in the material. If an electron is added to the material then a positive ion must be added as well, or negative ion taken away.

Intercalation

The mechanism of reversible ion intercalation was discovered by M. Stanley Whittingham in the 1970s at the Exxon Research and Engineering Company and is the typical mechanism of commercial lithium-ion batteries.[16] The dictionary definition of *intercalate* refers to the insertion of a date into a calendar, such as the addition of February 29th during leap years. Analogous to the insertion of an extra day into the calendar, ion intercalation into a crystal lattice is associated with little to no change of the crystal structure. Lack of any major phase change is advantageous to the reversibility of the intercalation reaction. However, lattice distortion caused by the insertion of ions can induce stress and volume change leading to mechanical degradation. Intercalation materials include layered compounds such as graphite, oxides like $LiCoO_2$ and V_2O_5, and chalcogenides such as MoS_2. Layered compounds can offer fast transport and storage of ions through interlayer sites. Other types of intercalation compounds include 3D ionic crystals such as α-MnO_2 and $LiFePO_4$. An example of an intercalation reaction of Li^+ into layered V_2O_5 is:

$$2Li^+ + 2e^- + V_2O_5 \rightleftarrows Li_2V_2O_5 \quad (2\text{-}3)$$

The vanadium species in V_2O_5 is V^{5+} that undergoes reduction to V^{4+} with the intercalation of Li^+ ions to produce $Li_2V_2O_5$.

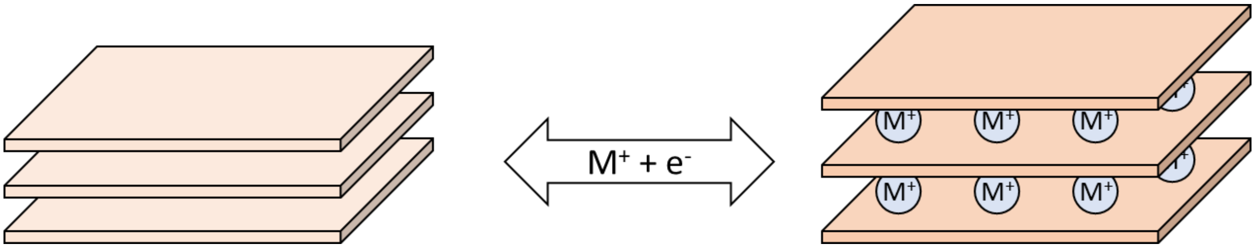

Figure 2-6. Ion intercalation mechanism into layered crystal.

Conversion

Unlike intercalation, conversion reactions are associated with total phase transformation of the initial crystal. An example of this type of mechanism is found in SnO_2 as an anode material for lithium-ion batteries (Equation (2-4)). In this reaction tin starts as Sn^{4+} in SnO_2 and is reduced all the way to Sn metal with the formation of a lithium oxide phase. This reaction is usually accompanied by several intermediate lithium rich tin oxide phases such as Li_2SnO_3 and Li_8SnO_6 that are also eventually reduced to Sn metal.[17] The complete destruction and reformation of secondary phases is accompanied by large volume change which leads to reduced cyclability of conversion type electrodes. Conversion to neutral metal generally happen at lower potentials as indicated by the metal conversion potentials in **Figure 2-2**, therefore this reaction mechanism is mostly restricted towards anode materials.

$$4Li^+ + 4e^- + SnO_2 \rightleftarrows Sn^0 + 2Li_2O \quad (2\text{-}4)$$

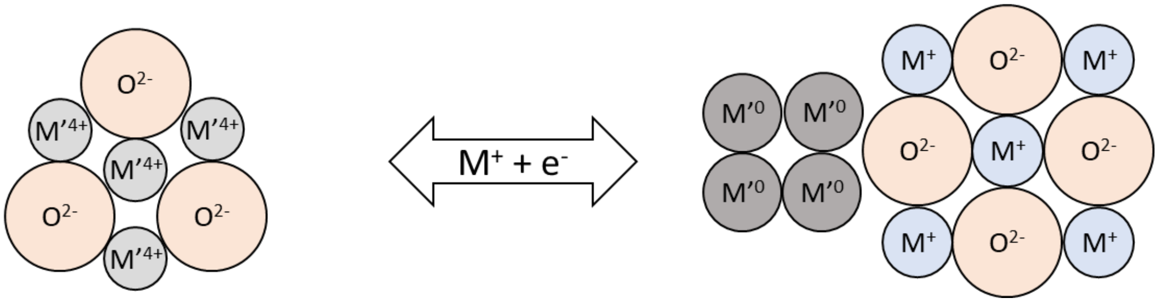

Figure 2-7. Chemical conversion reaction mechanism for metal oxide.

Alloying

Electrochemical alloying can occur in metals and metalloids. Alloying can achieve very high capacities but are accompanied by large volume changes that mechanically destroy the electrode during cycling. In contrast to intercalation and conversion, the metal ion from the electrolyte is the species being reduced since the metal can reduce no further. An example of alloying materials for lithium ion-batteries are tin and silicon.

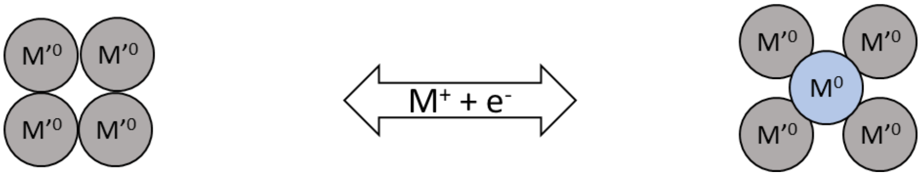

Figure 2-8. Alloying reaction mechanism for charge storage.

2.2.3 Definitions

Voltage, Current, and Resistance

The unit of voltage is the *Volt* which is equivalent to *Joules per coulomb*, in other words it can be defined as the amount of work required to move a coulomb of charge (1 electron = 1.6×10^{-19} C) between two points (or two electrodes).

Current is the number of charges that pass a point in a period of time with units of *ampere* or *coulombs per second*. It is important to note that current is not related to the speed of charge carriers, but rather the net flow of charge past a point. Unbound electrons in metal at room temperature travel quite fast in random directions (~1 million m/s), but with 0 net flow if there is no voltage applied. In contrast, when voltage is applied the net flow of electrons known as the drift velocity is on the order of micrometers to millimeters per second depending on the material, geometry, and applied voltage.

Voltage and current in a conductor are related through Ohm's law;

$$V = IR \tag{2-5}$$

where V is voltage, I is current, and R is resistance with units of Ohms (Ω) which is equivalent to *volts per ampere* and is the inverse of conductance. Materials with high resistance result in small current when voltage is applied. In battery materials resistance has an adverse effect on working voltage and should be minimized. The drop between open-circuit voltage and closed-circuit voltage is due to the Ohmic resistance in the battery and increases with increased current.

Conduction is not restricted to conducting electrons but also include mobile ionic species. Additionally, electrons bound in the valence band of insulators and semi-conductors can contribute to current through the migration of holes. Therefore, it is important to consider which charge carrier species is dominant for a given material system. For battery anodes and cathodes it is favorable that they possess both high electrical and high ionic conductivity. Every electron that is transferred in or out of a battery electrode must be accompanied by a transfer of opposite charge to or from the electrolyte.

Capacity

The quantity of electric charge stored in a battery electrode is known as the capacity with units of *coulombs*. It is important to differentiate this term from *capacitance* which is the charge divided by voltage with units of *coulombs per volt* or *farads*. Many battery applications operate under constant current conditions, and tests performed in battery literature are often performed at constant current known as galvanostatic testing, therefore it is convenient to write capacity in terms of current as *amp-hours* (i.e. 1 ampere of current run for 1 hour). If a battery electrode can be discharged at 1 milliampere for 100 hours then its capacity is 100 mAh, or 360 coulombs, which is about 0.004 moles of electrons that were exchanged. In literature, battery electrode capacity is typically normalized to the mass of electrode material labeled as specific capacity (mAh/g). A material's theoretical maximum capacity can be calculated by finding the number of available redox sites available per mass of material. For example, the material Fe_2O_3 has two Fe^{3+} ions per molecule. If both Fe^{3+} ions are reduced to Fe^{2+} and compensated by the addition of two Li^+ ions then the theoretical specific capacity could be calculated as follows;

$$Theoretical\ Specific\ Capacity\ \left(\frac{mAh}{g}\right) = n * \frac{F}{3.6\ mAh/C} * \frac{1}{M} \tag{2-6}$$

where n is the number of electrons exchanged per molecule during reduction or oxidation (2 for this example), F is the Faraday constant, 3.6 is a conversion factor between coulombs and mAh, and M is the molar mass of the molecule. Therefore, the theoretical capacity for the reduction of Fe_2O_3 to $Li_2Fe_2O_3$ is 336 mAh/g. However, this theoretical capacity says nothing about voltage, reversibility of the reaction, or stability of the new phase.

A battery's theoretical capacity is unrelated to voltage; however, electrode capacities are usually measured between a specified operating voltage, and the voltage profile throughout the battery's state of charge depends on the electrode's material chemistry. Similarly, a battery's capacity may vary depending on the magnitude of current. At higher current the side effects of overpotential are more prominent, for example there is a larger voltage drop due to ohmic resistance at high current according to Ohm’s law. A large overpotential may reduce the capacity achieved from a battery within a certain voltage range.

Energy

Energy is stored in electrodes as electrochemical potential energy and is converted into electrical energy during discharge. The units of energy are *Joules* and electrical energy for a battery can be calculated as the integral of voltage versus capacity (the area under the curve in galvanostatic plot). Since the units of capacity are already in *amp-hours*, it is convenient in literature and commercial batteries to list energy as *Watt-hours* instead of *Joules*. Energy can be normalized by dividing by mass or volume depending on the system. For example, liquid based batteries designed for grid-level energy storage such as vanadium redox-flow batteries are best described by energy per unit volume, since mass is not as important for stationary batteries.

As stated earlier, high current will influence operating voltage and capacity of the battery due to increased overpotentials, therefore energy is also reduced at higher currents.

Power

The amount of energy a battery can provide in a given amount of time is known as its power, or power density when normalized by mass or volume. The units of power are conveniently *Watts* when dividing energy by time. Applications that utilize large amounts of energy quickly such as electric motors and electromagnets require batteries with high power densities. The tradeoff between power density and energy density of a battery material is often plotted in a Ragone plot, with power density on the x-axis and energy density on the y-axis.

2.3 Iron-based chemistry for batteries

Iron is the most abundant transition metal element in the Earth’s crust, is the most mined and produced metal, and is the least expensive element per kilogram.[18,19] More importantly, soluble iron salts necessary for many syntheses are relatively inexpensive compared to similar nickel and cobalt salts, but are slightly more expensive compared to manganese salts (**Table 2-1**).

The two most common oxidation states of iron are 2+ and 3+, with a standard reduction potential at 0.771 V vs SHE.[20] Iron(III) has the electron configuration $[Ar]3d^5$, and typically forms octahedral coordination complexes in either the high-spin or low-spin state. The reduction potential of iron ions can vary greatly depending on ligand species. For example, ferric triethanolamine complex has a reduction potential of -0.859 V and ferric tripyridinetriazine at 1.484 V vs SHE.[21]

Iron forms various compounds with electrochemical activity and structures suitable for alkali-ion intercalation. The most commercially successful has been lithium iron phosphate (LFP) with formula $LiFePO_4$ which has been used in transportation and power tool applications. Research has investigated other iron systems as anodes and cathodes including oxides, chalcogenides, fluorides, polyanionic compounds, and hexacyanoferrates.

Table 2-1. Sale price of iron, manganese, nickel, and cobalt salts ranked by price per mol. Price data acquired from Sigma-Aldrich on 11/17/2020.

Chemical	Grade	CAS	Price ($/kg)	Price ($/mol)
manganese(II) sulfate monohydrate	ReagentPlus, >99%	10034-96-5	97	16
iron(II) sulfate heptahydrate	ReagentPlus, >99%	7782-63-0	102	28
manganese(II) chloride tetrahydrate	ReagentPlus, >99%	13446-34-9	202	40
iron(II) chloride tetrahydrate	Reagent Plus 98%	13478-10-9	205	41
iron(III) chloride hexahydrate	Reagent Grade >98%	10025-77-1	152	41
nickel(II) chloride hexahydrate	ReagentPlus	7791-20-0	185	44
manganese(II) nitrate tetrahydrate	purum p.a., >97%	20694-39-7	189	47
iron(III) nitrate nonahydrate	ACS reagent, >98%	7782-61-8	141	57
cobalt(II) sulfate heptahydrate	ReagentPlus, >99%	10026-24-1	223	63
nickel(II) sulfate hexahydrate	ReagentPlus	10101-97-0	310	81
cobalt(II) chloride hexahydrate	ReagentPlus, 98%	7791-13-1	472	112
cobalt(II) nitrate hexahydrate	ACS reagent, >98%	10026-22-9	580	169

2.3.1 Oxides

Various structures of metal oxides have been investigated as battery electrodes, namely the layered Li_xMO_2 type structure of NMC cathodes have become the most commercially popular due to their high energy density. Iron oxide materials have been investigated as alternative electrode materials due to their low toxicity and low cost.

$LiFeO_2$ of various crystal phases have been researched as an intercalation cathode for lithium ion batteries but suffers from irreversible voltage hysteresis upon the first charge cycle.[22] While the fist charge plateau is above 4 V, subsequent discharge and charge cycles fall between 1.5 – 3 V.[23] The oxidation state of Fe in pristine $LiFeO_2$ is 3+, meaning that the first charge is the oxidation of Fe^{3+} to Fe^{4+} with associated lithium deintercalation. It was proposed that the small Fe^{4+} ions swap coordination sites from octahedral 4a to tetrahedral 8c sites.[24] The new coordination would affect redox potential of the Fe centers and block diffusion pathways of lithium, resulting in higher diffusion resistance and lower capacity as observed. Other authors reported the presence of Fe^{2+}

after the first discharge and proposed that Fe^{4+} reacted with electrolyte upon the first charge, thus subsequent cycles associated with the $Fe^{3+/2+}$ redox pair at lower voltage.[25]

Contrastingly, $NaFeO_2$ has shown better success as an intercalation cathode for sodium ion batteries.[26] $NaFeO_2$ forms two polymorphs, O3 and P2, both of which consist of FeO_6 octahedra layers with Na ions sandwiched in between.[27] Unlike its lithium counterpart, $NaFeO_2$ displays reversible $Fe^{4+/3+}$ redox at a constant voltage plateau of 3.3 V vs Na, albeit Na extraction is restricted to 35% of its theoretical capacity due to irreversible structure change at higher voltages.[28,29]

Other iron oxides such as Fe_2O_3, and Fe_3O_4 have been of more interest as lithium ion battery anodes due to their lower redox potentials at around 0.8 V for reduction and 1.75 V for oxidation. The full conversion reaction from oxide to Fe metal and Li_2O product allows for high theoretical capacities of 1007 and 926 mAh/g for Fe_2O_3 and Fe_3O_4 respectively. However, the poor conductivity of iron oxide and severe structural transformation during lithium exchange deteriorates the cyclability of these materials. Additionally, it has been shown that Fe_2O_3 and Fe_3O_4 irreversibly change into other Fe_xO_y phase upon delithiation.[30,31] Much research on these oxides focuses on synthesizing nanostructures and carbon composites to mitigate problems with volume expansion and conductivity.[32]

2.3.2 Sulfides

Similar to iron oxides, the iron sulfides undergo conversion reactions to form metallic Fe and Li_2S, thus they also suffer from the same problems of volume expansion and cyclability.[33] Generally metal sulfides have higher conductivity and better mechanical stability than their oxides.[34] However, synthesis of iron sulfide nanoparticles necessary to counter the large volume expansion of conversion reactions is more challenging.[35] Additionally sulfide electrodes suffer from soluble polysulfides shuttling between cathode and anode, hurting coulombic efficiency.[36] Although FeS_2 has been commercially available as a primary lithium ion battery, reversibility of rechargeable iron sulfide in liquid electrolyte at room temperature has been a challenge.[37]

The main iron sulfides investigated as lithium ion battery anodes are FeS and FeS_2, boasting high theoretical capacities of 609 and 894 mAh/g, respectively. Iron sulfides exhibit slightly higher redox potentials than iron oxides. The redox chemistry of FeS_2 varies between studies, but generally exhibits two redox pairs around 1.8 and 1.3 V during reduction and 2.0 and 2.5 V vs lithium during oxidation.[35] There has been disagreement among researchers on the reaction pathway between FeS_2 and Fe + Li_2S, with the widely adopted theory being the formation of a Li_2FeS_2 intermediate phase.[36,38]

2.3.3 Fluorides

FeF_3 is electrochemically active to both lithium ion intercalation and conversion into Fe metal and LiF, obtaining a theoretical capacity of 237 mAh/g for intercalation alone and 712 mAh/g for the 3-electron reaction. Additionally, the reduction potentials at 3.4 and 2.1 V for intercalation and conversion make FeF_3 suitable as a cathode material for lithium ion batteries.[39] However, due to the insulating property of highly ionic FeF_3, only nanosized particles are able to realize full intercalation of 1 Li^+ ion to form $LiFeF_3$.[40] Similar to other conversion chemistries, the drastic structural change and volume expansion during its conversion reaction severely weaken the cyclic stability of FeF_3. Hydrated phases of FeF_3 have also been investigated as intercalation cathodes, allowing for increased cyclability at higher rates due to improved lithium ion diffusion.[41,42]

2.3.4 Polyanions

Iron-based polyanion compounds encompasses a wide variety of anion species such as phosphates, sulfates, and silicates. It has been found that the redox potential of a given iron polyanion structure is influenced by the X species via the *inductive effect* where higher electronegative X species in X-O-M next nearest neighbor coordination results in higher redox potential.[43] Iron polyanion compounds generally have poorer electrical conductivity than layered and spinel oxides, and have lower specific and volumetric energy density, thus less attractive towards portable electronic applications. However, their cyclic stability, low cost, low toxicity, and thermal stability makes the iron polyanion compounds attractive as cathodes.

The most commercially competitive iron-based lithium-ion battery cathode is lithium iron phosphate ($LiFePO_4$) with decent theoretical capacity of 170 mAh/g and moderate operating voltage of 3.5 V.[44] $LiFePO_4$ belongs to the olivine crystal family in which lithium and iron occupy octahedral sites linked to phosphorous in tetrahedral sites of an hcp oxygen anion lattice.[44] Its advantage over other transition metal phosphates like $LiMnPO_4$ is that the delithiated $FePO_4$ phase is stable and nearly identical in structure with only 6.8% volume change, allowing for good cyclic stability.[45] Another problem with $LiNiPO_4$ and $LiCoPO_4$ are the high redox potentials at 5.1 and 4.8 V vs Li^+/Li that lead to electrolyte oxidation.[46,47] However, rate performance of $LiFePO_4$ is severely hindered by its low electrical conductivity, which is typically abated by carbon coating and carbon composites.[48]

Other polyanion structures have widely been investigated chasing the success of $LiFePO_4$, with sulfate being the most promising. Substituting sulfate for phosphate requires the addition of a monovalent anion to maintain charge balance, fluorine being an appropriate choice in the synthesis of $LiFeSO_4F$ having a theoretical capacity of 151 mAh/g. This material has been synthesized in the low-termperature tavorite and high-temperature triplite structures with respective redox potentials around 3.6 and 3.9 V vs Li^+/Li.[49] Both structures are made of interconnected FeO_4F_2 octahedra with tavorite phase having corner sharing octahedra and triplite having edge sharing octahedra. Additionally, the triplite has a random disordering of Li and Fe ions.[50] The difference in redox potential between the two phases has been attributed to the lower stability of the triplite structure due its edge sharing Fe^{3+} repulsion and its *cis* F-F configuration.[49,51] Despite higher redox potential, triplite has larger polarization and poorer capacity due to larger diffusion resistance attributed to disordered Li sites.[50] The development of $LiFeSO_4F$ as a cathode material is challenged by scalable non-aqueous synthesis techniques.

Many other iron polyanion compounds have been investigated as lithium and sodium-ion battery cathodes. Some examples of lithium-ion cathodes include borates,[52] silicates,[53] oxalates,[54] jarosites,[55] and pyrophosphates.[56] Iron-based cathodes for sodium-ion batteries include alluaudite-type sulfates,[57] pyrophosphates,[58] and amorphous $FePO_4$.[59]

2.3.5 Hexacyanoferrates

Metal hexacyanoferrate (MHCF) materials encompass a wide variety of compounds with general formula $A_xM_y[Fe(CN)_6]_z*nH_2O$, where *A* represents a variety of possible interstitial cations such as Li^+, Na^+, K^+, NH_4^+, etc. introduced during synthesis or through electrochemical intercalation, and *M* can be a transition metal cation.[60] MHCF compounds have been of interest across multiple disciplines due to their unique zeolitic structure, redox activity, magnetic properties, biocompatibility, and low cost.[61] MHCF materials have been used in commercial applications and in research as pigments for paints and dyes, medicine for radiation poisoning and absorbent of radioactive ions from contaminated water supply, battery materials, electrochromic coatings, catalysts for oxygen and hydrogen evolution reactions, biomolecular sensors, and cancer theranostics.[62–67]

The iron hexacyanoferrate compound (FeHCF) is commercially known as Prussian blue, a paint pigment and medicine for cesium poisoning. Various Prussian blue analogs (PBAs) such as

MnHCF, NiHCF, CoHCF, and CuHCF have also been investigated as cathode materials for sodium-ion batteries, and other rechargeable batteries such as lithium, potassium, zinc, calcium, and ammonium.[68] These compounds typically arrange in a face-centered cubic crystal lattice of *M* cations octahedrally coordinated to the nitrogen of $[\mathrm{Fe(CN)_6}]$ octahedra anions and *A* cations located in the large interstitial sites (**Figure 2-9**).[61] In FeHCF the strong ligand field of the cyanide ion results in the C-coordinated Fe cation of $[\mathrm{Fe(CN)_6}]$ groups to take the low-spin electronic configuration while the N-coordinated Fe cation remains in the high-spin state.[69] Consequently, there exists two separate redox potentials for high-spin and low-spin Fe.[70] The crystal lattice may deviate from its cubic symmetry based on intercalant and water concentration. For example, FeHCF with high sodium content may distort to the rhombohedral phase or further to the monoclinic phase if water content is also high.[71] Furthermore, $[\mathrm{Fe(CN)_6}]$ anion vacancies and water can exist in the structure which could affect ion intercalation, redox potential, diffusion, and stability of the crystal. Anion vacancies are presumed to be accompanied by *A* cation deficiency or change in valence of Fe to maintain charge balance; however, it has been postulated that OH^- or other anions from synthesis could enter the FeHCF crystal, yet there is no concrete evidence for this.[72]

$Na_xFe[Fe(CN)_6]$ has received much attention as a cathode material for sodium ion batteries due to its high sodium ion diffusion, high reduction potential (average ~3 V vs Na), good theoretical capacity (171 mAh/g), and inexpensive iron-based precursors. However, FeHCF cathodes suffer from poor cyclability due to side reactions with the electrolyte at high voltage, coordinated water decomposition, and lattice collapse from $[Fe(CN)_6]$ vacancies.[68] It has been shown that redox activity can be increased from improving crystallinity and sodium concentration.[73–76] Additionally, doping of Ni^{2+} has shown to increase redox activity of low-spin

$[Fe(CN)_6]$, while increased concentrations of Ni^{2+} also help the cyclic stability at the expense of capacity.[68,77]

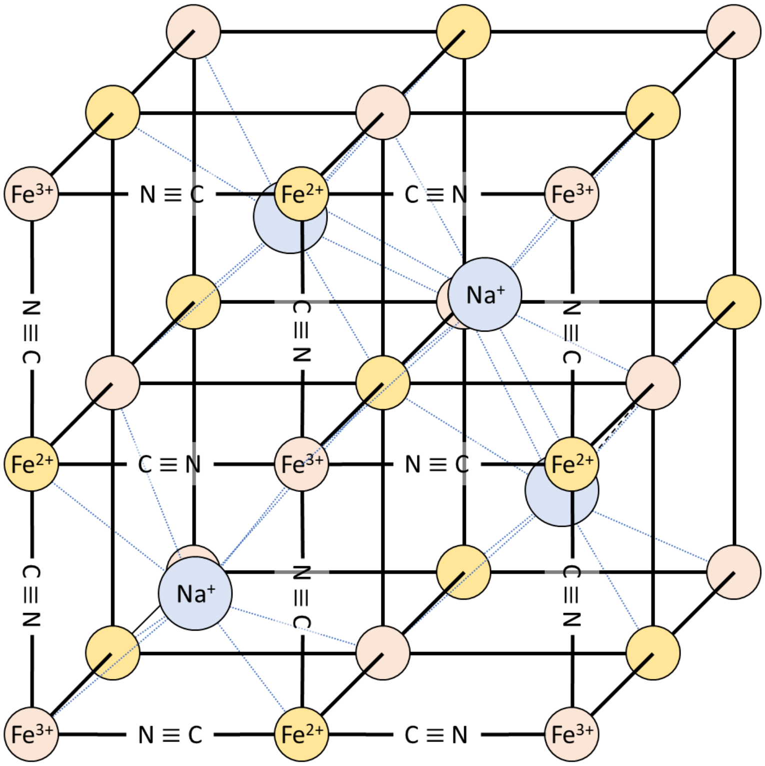

Figure 2-9. Ideal crystal structure of FeHCF. Black lines represent cyanide ligands.

2.3.6 Iron Flow Batteries

Redox flow batteries are electrochemical systems in which two redox active species exist as part of two electrolytes separated by a selective permeable membrane (**Figure 2-10**). During discharge the electrolyte species with higher reduction potential, termed the catholyte, is pumped through its cell and is reduced at the surface of its electrode. The anolyte species is pumped through the other half of the cell and oxidized at its electrode. The separating permeable membrane allows for selective ion exchange to maintain charge balance between the two electrolytes but should not allow cross-over of anolyte and catholyte species. All-liquid redox flow batteries have a separation of energy capacity and power. Energy capacity is controlled by the volume of electrolyte, while power is controlled by electrode surface area. Thus the scalability of these cells is practical for grid-level energy storage where specific and volumetric energy density is not as critical.[78]

There have been several startup energy companies focusing on flow batteries for energy storage. ESS Inc. in Wilsonville, Oregon manufactures all-iron flow batteries with an iron metal / ferrous chloride anolyte and ferric/ferrous chloride catholyte. The use of iron species provides low toxicity and low cost compared to chemistries such as the all-vanadium redox flow battery. However, the use of metallic iron electrode loses the benefit of decoupled energy and power. Additionally, the reduction potential of Fe^{2+} to Fe metal can be lower than that of the hydrogen evolution reaction in acidic media.[79]

There has been much research into other iron-based flow batteries. Generally, using different chelates of iron can alter the redox potential of the $Fe^{3+/2+}$ couple and increase solubility, allowing for all-liquid all-iron flow batteries. Chelation by EDTA, oxalate, and citrate ligands depreciates redox potential, making suitable anolytes in comparison to H_2O, Cl^-, and CN^- ligands.[80]

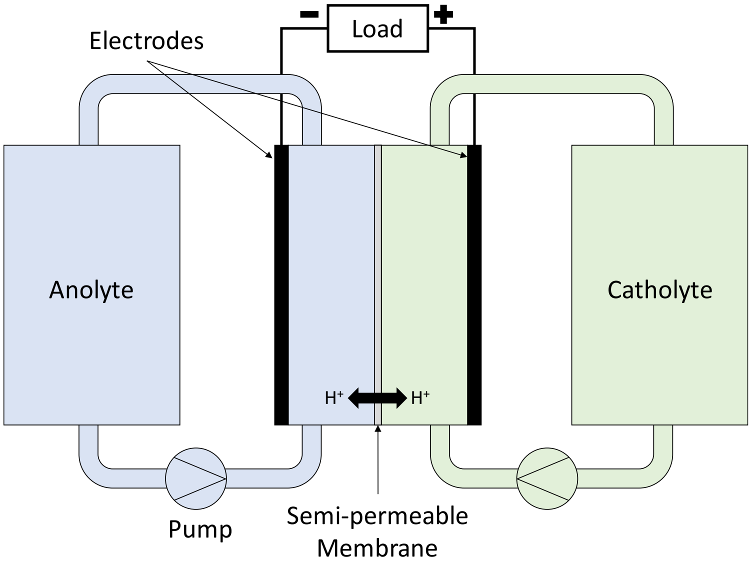

Figure 2-10. Simplified diagram of generic flow battery. Reduction and oxidation of anolyte and catholyte species occur at the surface of the electrode. Protons or sodium ions permeate through a separating membrane to maintain charge neutrality.

Reproduced in part with permission from ACS Applied Energy Materials, submitted for publication. Unpublished work copyright 2020 American Chemical Society. Submitted November 5th, 2020.

Chapter 3: Effect of vacancies on lithium-ion diffusion in Jarosite structure

Pb-jarosite, $Pb_{0.5}Fe_3(SO_4)_2(OH)_6$, is investigated for the first time as an intercalation cathode for lithium-ion batteries. Despite having a lower theoretical specific capacity than its Na-jarosite analog, $NaFe_3(SO_4)_2(OH)_6$, bulk Pb-jarosite displays higher lithium-ion capacity especially at higher current rates. The greater lithium storage is attributed to more kinetically facile diffusion of lithium in Pb-jarosite, as evidenced by PITT data indicating an average diffusion coefficient over 10 times larger. ICP-OES and XRD measurements show that the substitution of divalent Pb^{2+} into monovalent Na^+ sites result in an increased number of cation vacancies and a more open structure to facilitate lithium diffusion. Ex-situ XRD measurements show that Pb-jarosite is more resilient to the semi-reversible crystalline-to-amorphous phase transformation that occurs in Na-jarosite over many cycles. These findings demonstrate that multivalent cation substitution in jarosite materials can significantly improve their performance as intercalation cathodes.

3.1 Introduction

Natural jarosite ore has had little economic value, however there has been extensive study on the formation of jarosite by mineralogists and hydrometallurgists due to its importance in the acid leach mining industry. During acid leaching of zinc, copper, and nickel bearing ores, precipitation of jarosite in acidic media is a crucial step that allows for the physical separation of Fe^{3+} and other cations from the leach solution. As a result, these refining plants produce large amounts of environmentally hazardous jarosite waste that are stored in containment facilities or dumped on site.[81] These jarosite wastes currently provide no economic value but have been the focus of research investigating the feasibility of recycling jarosite into marketable products. For example, Karamanov, et al. studied the crystallization of high-iron content glass-ceramics based on jarosite and several researchers have explored the use of jarosite in construction materials.[82–84]

Jarosite is a family of naturally occurring minerals that belong to the alunite supergroup with general formula $DG_3(TO_4)_2(OH)_6$, where G represents Fe^{3+} cations and TO_4 represents SO_4^{2-} groups. D can represent different monovalent cations, such as K^+, Na^+, NH_4^+, and H_3O^+, or divalent cations Pb^{2+} and Hg^{2+}.[81] The substitution of a divalent cation requires charge balance of the compound by the introduction of vacancies in the D site. The Na-jarosite structure, $NaFe_3(SO_4)_2(OH)_6$, is built up of FeO_6 octahedra layers connected equatorially through $(OH)^-$ groups. SO_4^{2-} groups are shared between the poles of three FeO_6 and point into interlayers. The opposite poles of FeO_6 octahedra share with Na^+ 12-coordinate polyhedral which exist in between layers of FeO_6 octahedra. The substitution of monovalent Na^+ ions for divalent Pb^{2+} ions reduces the required number of 12-coordinate cations by half and introduces vacant sites while retaining the same jarosite crystal structure.[85]

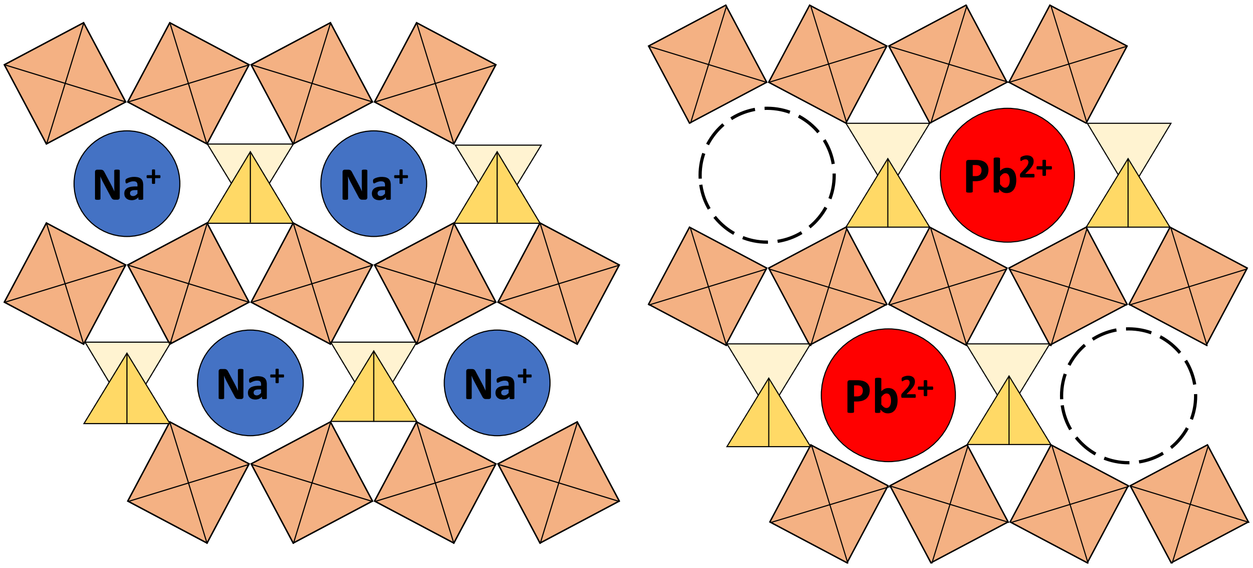

Figure 3-1. Simplified diagram of Na- and Pb-jarosite sructure showing FeO_6 octahedra (orange) interconnected equitorially by OH^- groups (not shown) and poles shared with base cornors of SO_4^{2-} tetrahedrals. Not to scale, ion size is exaggeratted.

Recycling of an environmentally hazardous waste material is an appealing aspect of jarosite and could provide it the economic advantage to make it competitive in the battery market that warrants its further investigation despite its lower energy density. Lithium and sodium intercalation into the jarosite structure was first reported by the Raveau group in 2014.[55,86] Since then there have been several other publications on nanostructured jarosite cathodes, ammonium-jarosite, and fluoride doped jarosite.[87–89] Currently, synthesized jarosite nanosheets and nanoparticles provide the best capacity over many cycles and at high currents. However, more investigation must be done on the bulk electrochemical properties of other jarosite compounds that could potentially be sourced from leach mining waste.

This study investigates the electrochemical properties of synthetic Pb-jarosite microparticles, compared to synthetic Na-jarosite. The theoretical capacities of Na-jarosite and Pb-jarosite are 165.9 and 142.2 mAh/g, respectively, when 1 Li^+ ion is intercalated for every Fe^{3+} cation. It is hypothesized that the formation of vacancies by the substitution of Pb^{2+} ion in place of Na^+ would increase the intercalation capacity of bulk jarosite by increasing diffusion kinetics of lithium ions.

3.2 Experimental

Synthesis of jarosite powders

Na-jarosite was synthesized using a precipitation procedure similar to those investigated by Dutrizac.[90] Ferric sulfate and sodium sulfate were completely dissolved in 100 mL of deionized water at a concentration of 0.1 and 0.3 M, respectively. The pH of the solution was adjusted to 1.6 at room temperature with the addition of sulfuric acid. The solution was refluxed in an oil bath at 97^oC under constant stirring for 48 hours. Afterwards, the yellow jarosite precipitate was collected and washed with hot deionized water, then dried at 80^oC under vacuum for 12 hours.

Pb-jarosite was synthesized by preparing a 100 mL solution of 0.15 M ferric sulfate and 0.08 M lead chloride. Lead chloride did not readily dissolve into solution due to its low solubility in water. Additionally, the solution contained 0.3 M lithium sulfate to increase the incorporation of Pb^{2+} into the product.[91] The pH was adjusted to 1.6 using sulfuric acid and the mixture was refluxed in an oil bath at 97°C under constant stirring for 48 hours. Afterwards a yellow precipitate was collected and washed with warm 10% ammonium acetate solution in order to leach away any lead sulfate impurities as prescribed by Dutrizac, then subsequently washed with hot water.[91] The Pb-jarosite powder was dried at 80°C under vacuum for 12 hours.

After drying, the jarosite powders were dry ball milled in polyethylene containers with 500 4-mm hardened 440C stainless steel balls for 72 hours at a speed of approximately 80 rpm.

Physical characterization

The crystal structures of Na-jarosite and Pb-jarosite powders were characterized with 1D X-ray diffraction (XRD) using a Bruker D8 Focus with Cu X-ray source with nickel filter. Ex situ XRD of cycled batteries was performed by the same method. Particle size of the jarosite powders were determined using a Horiba LA-950 particle size analyzer. The relative concentrations of Na, Pb, and Fe elements of synthesized powders was determined using inductively coupled plasma – optical emission spectroscopy (ICP-OES) with a Perkin Elmer Optima 8300. Scanning electron microscopy (SEM) images of jarosite electrodes were taken on a Sirion XL30.

Electrochemical characterization

Cathodes were prepared from jarosite powders by making a slurry of 70% active material, 20% Super P carbon powder, and 10% carboxymethyl cellulose (CMC) binder in water. The slurry was deposited onto an aluminum foil current collector via doctor blading and allowed to slowly dry at room temperature before drying under vacuum for 12 hours at 80°C. Jarosite half-cell batteries were assembled in CR2016 type coin cells with commercial lithium metal anodes (MTI Corp.) and Celgard polypropylene-polyethylene separator inside of an argon-filled glovebox with oxygen and water concentrations below 0.5 ppm. The electrolyte used was a commercial solution of 1 mol L^{-1} $LiPF_6$ in ethylene carbonate (EC) and diethyl carbonate (DEC) in a 1:1 volume ratio (Sigma-Aldrich). The assembled batteries rested for at least 12 hours before electrochemical tests.

Galvanostatic cycling was performed between 2.0 – 4.0 V versus Li^+/Li at rates between C/20 and 1C with respect to their theoretical capacities. Cyclic voltammetry was performed on batteries at 0.1 mV/s between 1.6 – 4.0 V. Electrochemical impedance spectroscopy (EIS) was performed on a Solartron instrument between 100 kHz and 0.1 Hz at an amplitude of 5 mV. Potentiostatic intermittent titration technique (PITT) was performed from 4.0 to 2.0 V at 5 mV potential steps until current decayed below C/200. PITT was preceded by two constant current-constant potential (CCCP) cycles with a constant current of C/20 and held at 2.0 and 4.0 V until current dropped below C/200.

3.3 Results and Discussion

Structure and Stoichiometry

X-ray diffraction peaks of synthesized jarosite powders fit the rhombohedral $R\bar{3}m$ jarosite crystal structure as indicated by their matching PDFs (**Figure 3-2**). $PbSO_4$ impurities were absent from Pb-jarosite after washing with a 10% ammonium acetate solution. Pb-jarosite has a larger interplanar spacing based on its larger c-axis lattice parameter of 16.86 Å compared to 16.62 Å for Na-jarosite as determined by their (006) peak positions. The expanded lattice is likely due to the larger radii of Pb^{2+} ions compared to Na^+, but also possibly contributed to from the loss of coulombic attractive forces in cation vacant sites that are coordinated by oxygen anions. The slight differences in peak intensity observed between Pb-jarosite and its reference could be caused by differences in composition. It is typical for synthetic jarosites to make solid solutions with hydronium-jarosite.[92,93]

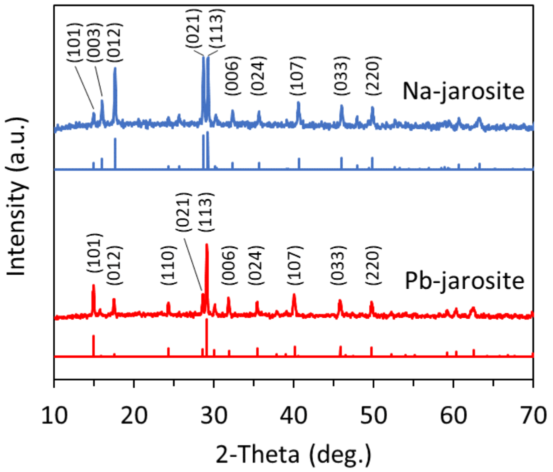

Figure 3-2. XRD patterns of as-synthesized Na-jarosite and Pb-jarosite samples compared against PDF card No. 04-015-8168 and 00-033-0759 for natrojarosite and plumbojarosite with selected peaks indexed.

Aqueous samples were prepared for ICP-OES by dissolving weighted amounts of Na-jarosite and Pb-jarosite in hydrochloric acid. Elemental concentrations were determined by measuring spectral intensity of characteristic wavelengths of selected species in comparison to standard analytes and background intensity (**Figure 3-3**). The metal cation ratio between Na, Pb, and Fe was calculated to be 0.54:0:3 and 0:0.33:3 for Na-jarosite and Pb-jarosite respectively based on concentration results from ICP-OES (**Table 3-1**). The negative concentration values for Pb in Na-jarosite and for Na in Pb-jarosite indicate the concentrations of these components are close to zero. Charge compensation for missing metal cations could be made possible by crystalline H_3O^+ ions. Additionally, the divalent Pb^{2+} substitution for monovalent Na^+ sites will introduce vacancies in the Pb-jarosite crystal. The resulting chemical formulae based on ICP-OES are

$[Na_{0.54},(H_3O)_{0.46}]Fe_3(SO_4)_2(OH)_6$ and $[Pb_{0.33},(H_3O)_{0.33}]Fe_3(SO_4)_2(OH)_6$ assuming there are no Fe^{3+} or anion vacancies. These results indicate 1/3 of 12-coordinate *D* sites are vacant in Pb-jarosite.

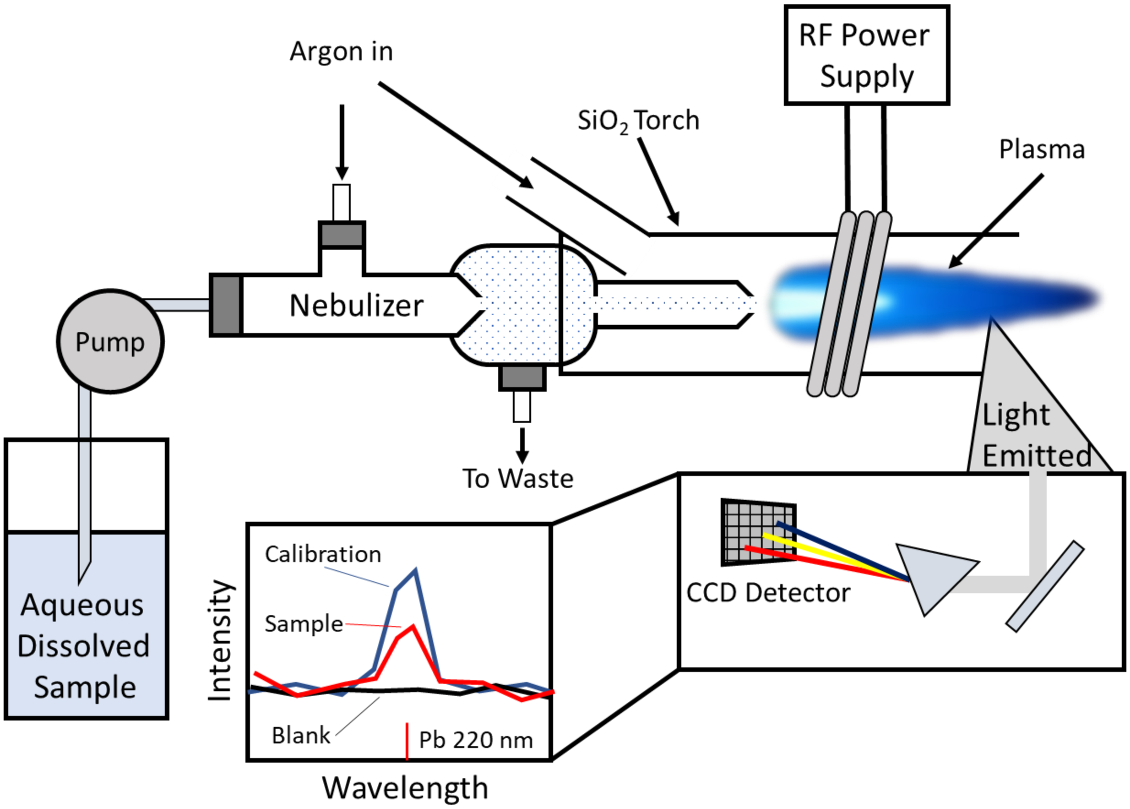

Figure 3-3. Schematic representation of ICP-OES.

Table 3-1. ICP-OES concentration results for element species Na, Fe, and Pb for Na-jarosite and Pb-jarosite.

Element	Line (nm)	Na-jarosite (mg/L)	Pb-Jarosite (mg/L)
Na	589.995	1.013	-0.119
Fe	239.562	13.68	11.39
Pb	220.353	-0.053	4.761

Laser particle size analysis and SEM of samples after ball milling reveal bulk jarosite powders with average particle size of 0.6 and 0.8 µm for Na-jarosite and Pb-jarosite, respectively (**Figure**

3-4). The refractive indices used by the particle size analyzer to measure particle size were 1.83 and 1.88 for Na-jarosite and Pb-jarosite, respectively.[94] These values from literature were measured for natural natrojarosite and plumbojarosite which may differ from synthetic analogs which could vary these results.

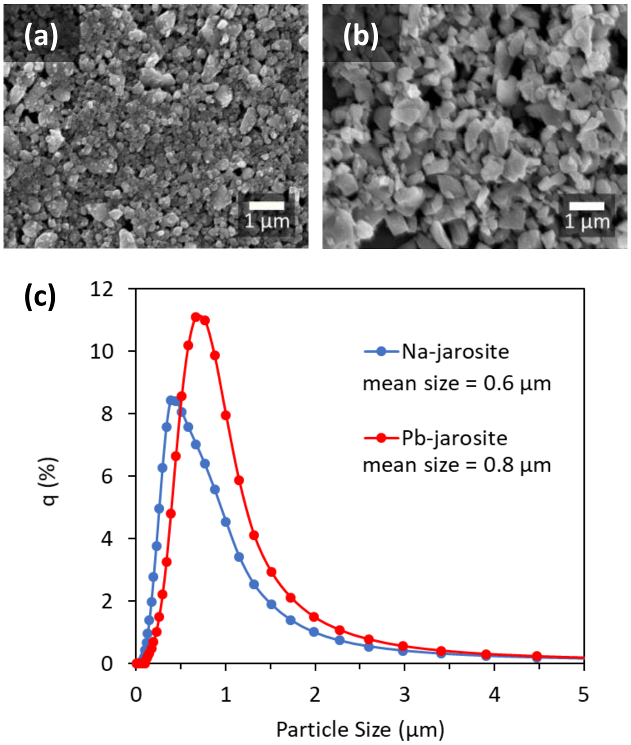

Figure 3-4. SEM micrograph of Na-jarosite (a) and Pb-jarosite (b) after ball milling. Particle size analysis of synthesized Na-jarosite and Pb-jarosite after ball milling (c).

Reduction/Oxidation Response

Cyclic voltammetry of lithium half-cells at 0.1 mV/s shows reduction peaks during the first cycle around 2.4 V for Na-jarosite and at 2.3 V and 2.5 V for Pb-jarosite (**Figure 3-5**), corresponding to lithium-ion intercalation and Fe^{3+} reduction. This is followed by oxidation peaks at around 3.0 and 2.6 V for Na-jarosite and Pb-jarosite, respectively. The redox potential is influenced by the local chemical environment of the $Fe^{3/2+}$ ion, as well as site energy of the intercalant ion. Pb has a significantly higher electronegativity than Na (1.9 vs 0.9), and the divalent Pb^{2+} ion will exhibit a larger coulombic force than monovalent Na^{+} ions. These elemental properties of Pb may draw more electron density away from neighboring oxygen ions that coordinate to $Fe^{3/2+}$ centers, thereby increasing the reduction potential of Fe^{3+} via the inductive effect.[95]

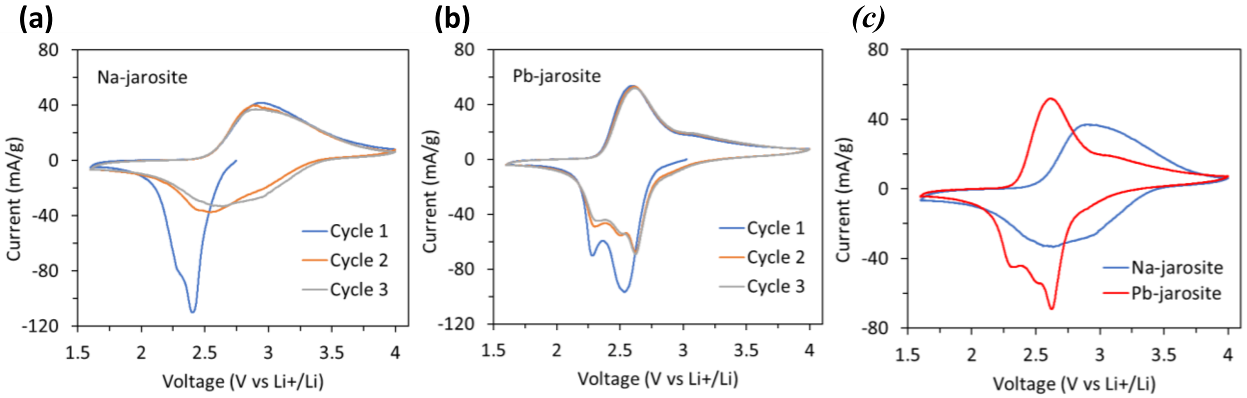

Figure 3-5. Cyclic voltammetry of Na-jarosite (a), Pb-jarosite (b), and overlayed 3rd cycle (c) at 0.1 mV/s in coin cells with lithium metal anode and 1 mol L^{-1} $LiPF_6$ in EC/DEC electrolyte.

The reduction peaks of Na-jarosite become broader and shift in redox potential upon subsequent cycles. Changing redox potential implies a changing environment of the redox active species. Na-jarosite has previously been shown to undergo a change in phase to an amorphous polymeric structure during lithium ion intercalation.[55] Broadening of CV peaks could be attributed to amorphization, resulting in a range of energy states for lithium ion insertion.[96] In contrast, the distinct redox peaks present in Pb-jarosite is indicative of a more defined chemical environment, implying a more rigid crystalline host structure upon intercalation. Additionally, a third reduction peak emerges at 2.63 V which may have been suppressed in the first cycle. The multiple reduction peaks of Pb-jarosite could arise from multiple non-equivalent Fe^{3+} centers or distinct intercalation sites for lithium ions created by the introduction of vacant sites to the crystal structure.

Galvanostatic Stability

Galvanostatic cycling was performed on batteries at a current rate of C/5 (**Figure 3-6**). The specific capacities of the first discharge were 89.8 and 91.4 mAh/g, which corresponds to 1.62 and 1.93 Li^+ intercalated per formula unit (FU) for Na-jarosite and Pb-jarosite, respectively. This illustrates increased lithium ion capacity in Pb-jarosite leading to greater specific capacity despite the increased molecular weight. The increased lithium ion capacity in Pb-jarosite could be connected to the vacancies introduced in the crystal lattice and larger interplanar spacing between $Fe(SO_4)$ layers, both contributing towards a higher lithium ion diffusion coefficient. Furthermore, the overpotential is approximated for the third cycle by taking the difference in voltage between

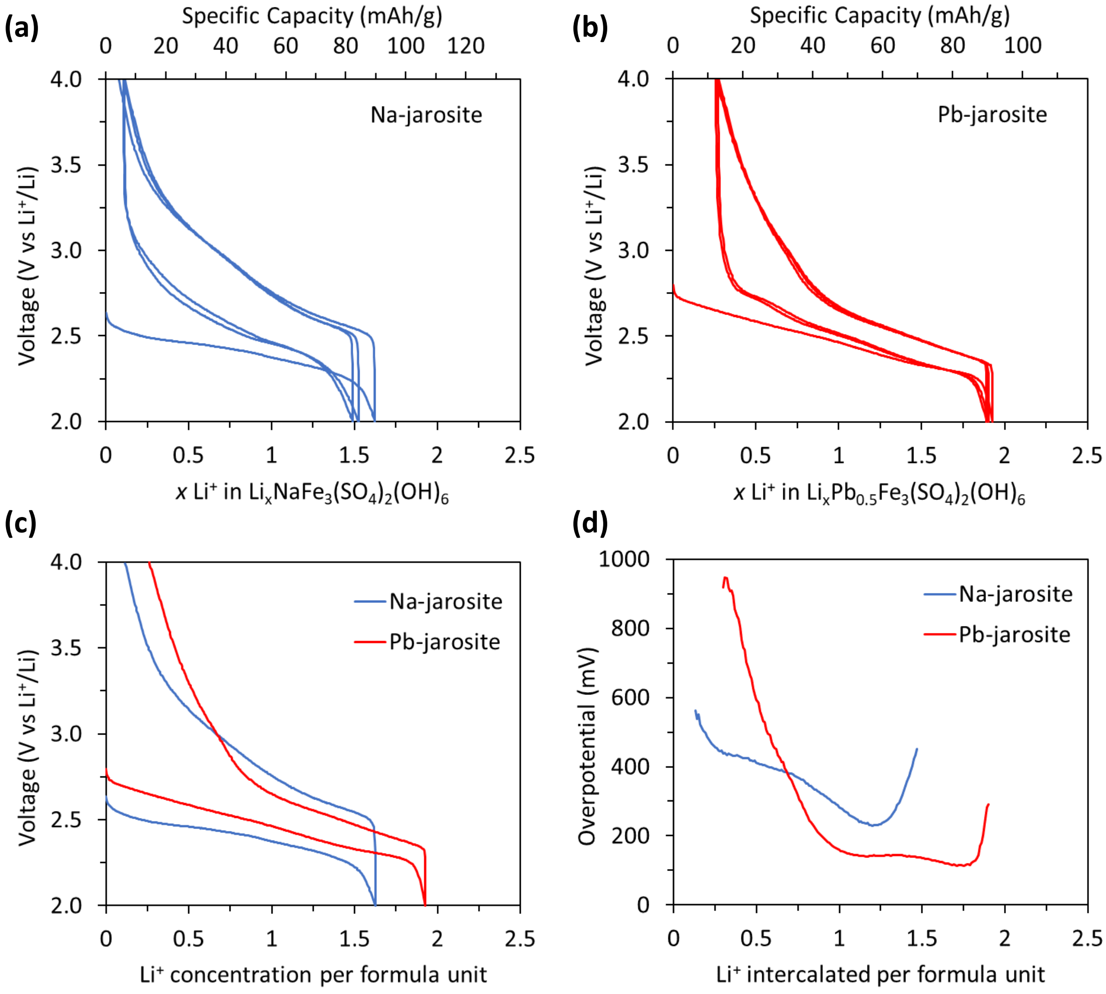

Figure 3-6. Galvanostatic cycling curves of first 3 cycles at C/5 for (a) Na-jarosite and (b) Pb-jarosite. Comparison of first cycle (c) and overpotential between discharge and charge curve of 3rd cycle (d).

charge and discharge curves (**Figure 3-6d**). The lower overpotential of Pb-jarosite at lithium concentrations greater than 0.75 indicate better intercalation kinetics and reversibility, which corroborates the small peak-to-peak separation seen in **Figure 3-5b**.

Both materials exhibit capacity loss after the first cycle, possibly due to irreversible intercalation of Li^+ remaining in the host crystal. Pb-jarosite has a larger irreversible loss as illustrated by the larger separation between the start of subsequent cycles and the y-axis in **Figure 3-6b**. This is also confirmed by a larger c-axis lattice expansion after the first cycle, increasing to 16.73 and 16.98 Å for Na-jarosite and Pb-jarosite, respectively (**Figure 3-9**). Despite lower coulombic efficiency during its first cycle, Pb-jarosite still retained a greater reversible lithium ion extraction of about 1.6 Li^+/FU compared to 1.4 Li^+/FU in Na-jarosite at a current rate of C/5.

Furthermore, the cyclic stability is higher in Pb-jarosite, retaining 90.2% of its original capacity compared to 85.0% for Na-jarosite after 50 cycles at a current of C/5 (**Figure 3-7a**). However, the galvanostatic voltage profiles significantly change for both materials upon subsequent cycling (**Figure 3-7b&c**). With each cycle the voltage profile loses its typical plateau shape and becomes more linear. This trend matches the broadening of redox peaks in CV for Na-jarosite and indicates a more solid-solution-like intercalation behavior. Additionally, CV of batteries after galvanostatic cycling generated voltammograms with broad profiles and attenuated redox peaks (**Figure 3-8**). It is evident from the transformation of voltage profiles that the local environment of the $Fe^{3/2+}$ redox center is irreversibly changing during cycling. The linear galvanostatic profile and pseudo-capacitive like voltammogram of Na-jarosite resembles the intercalation chemistry of other amorphous materials.[96] This is due to a distribution of energies created by the disordered ligand environment and intercalation sites.

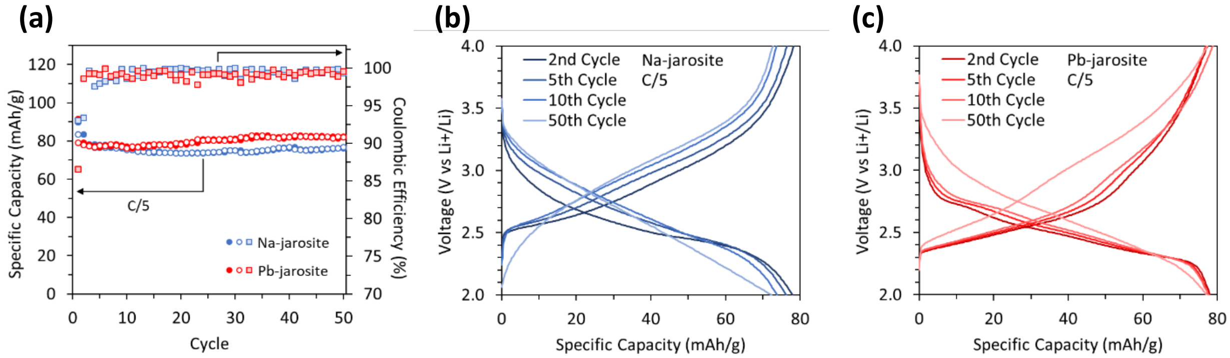

Figure 3-7. Galvanostatic cycling stability at C/5 for Na-jarosite and Pb-jarosite (a). Closed circles are discharge capacity, open circles are charge capacity, and squares are coulombic efficiency. Galvanostatic cycling curves at C/5 for Na-jarosite (a) and Pb-jarosite (b) at various cycles.

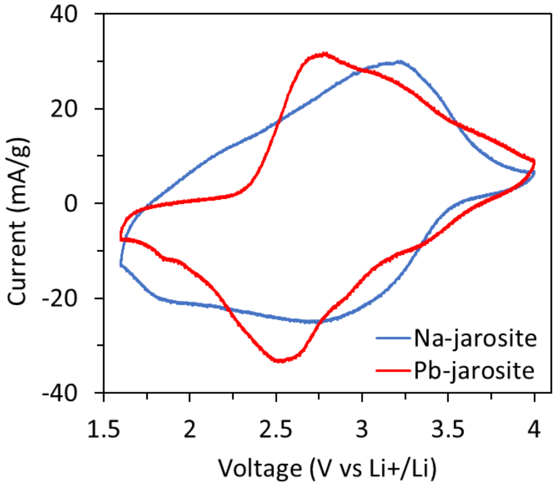

Figure 3-8. Cyclic voltammetry of Na- and Pb-jarosite after cycling.

Electrochemical induced phase transformation

It has been illustrated by Gnanavel, et al. that Na-jarosite undergoes a reversible crystalline to amorphous phase transformation upon lithium intercalation and deintercalation, suggesting that the amorphous phase is closely related in structure to crystalline jarosite.[55] However, the longevity of this reversible transformation was not investigated. To further understand how the jarosite structure changes during cycling, ex situ XRD was performed on cycled electrodes (**Figure 3-9**). Na-jarosite and Pb-jarosite both undergo a crystalline to amorphous transformation during their first discharge to 2.0 V evidenced by diminished diffraction peaks. Recharging to 4.0 V coincides with the regaining of periodic order of the crystal structure, illustrating the reversible transformation between amorphous and crystalline phases via electrochemical intercalation and deintercalation. However, this phase transformation loses reversibility upon further cycling. By the 50th charge cycle Na-jarosite has nearly lost all diffraction peaks, while Pb-jarosite still retains its strongest peaks, albeit at lower intensity.

The ability for Pb-jarosite to better revert back to its crystalline structure may be evidence of a lower energy, more stable crystal structure compared to Na-jarosite. Pb^{2+} and Na^{+} ions reside in the interstitials of large 12-coordiante oxygen icosahedron cages. The stability of ionic polyhedral generally follow the cation-anion radius ratio limits according to Pauling's rules for ionic crystals, with the critical radius ratio of 12-coordinate polyhedral being 1. Considering the Shannon ionic radii for 12-coordinate Pb^{2+} and Na^{+}, 1.49 and 1.39 Å respectively, and 1.40 Å for O^{2-}, the cation-anion ratios are 1.06 and 0.99 for Pb^{2+} and Na^{+}.[97] This illustrates Pb^{2+} would be the more stable cation in the jarosite structure and could be explanation for Pb-jarosite's improved reversion to its crystalline form upon deintercalation.

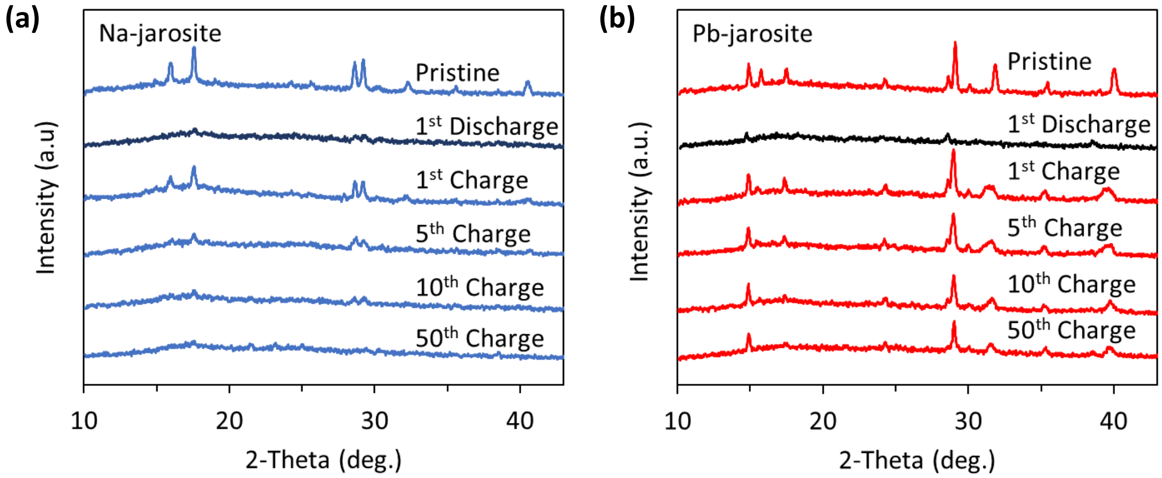

Figure 3-9. Ex situ XRD patterns of (a) Na-jarosite and (b) Pb-jarosite electrodes at various cycles.

In conjunction with ex situ XRD, jarosite electrodes were characterized with ex situ FTIR to better understand the changing chemical environment (**Figure 3-10**). The different absorption peaks can be assigned to different molecular bond vibrations and distortions.[55] In particular, the relative intensity of absorption peaks at low wavenumber corresponding to Fe-O vibrations significantly decreases after lithium intercalation in the first discharge. This has been speculated to be caused by FeO_6 distortion and conversion to FeO_5 during lithiation.[55] These Fe-O absorption peaks are restored after delithiation; however, upon subsequent charge cycles the relative intensity of Fe-O absorption peaks diminishes. The gradual loss of Fe-O bonding could be associated with the permanent transformation of the amorphous jarosite phase as shown in ex situ XRD.

The transformation of Fe-O bonding corroborates the evolving voltage profiles during galvanostatic cycling and cyclic voltammetry which occurs to a greater extent in Na-jarosite. A changing redox potential is indicative of a changing local chemical environment surrounding the Fe^{3+} redox centers. The redox potential is strongly related to the energy levels of d-orbitals in Fe ions. The energy levels of d-orbitals split when coordinated to different ligands according to crystal field theory due to the overlap between metal d-orbitals and ligand bonding orbitals. In an octahedral coordination the d_{x^2} and $d_{x^2-y^2}$ have increased energy due to closer overlap with ligands, while the d_{xy}, d_{xz}, and d_{yz} orbitals have decreased energy. The octahedral d-orbital energies can further split if the octahedral coordination becomes distorted or if ligands are removed (**Figure 3-11**). In the crystalline jarosite phase all Fe ions should exist in octahedral coordination giving more plateau like discharge curves; however, as the jarosite structure becomes amorphous and loses Fe-O bonding as illustrated in ex situ XRD and FTIR, there may exist other Fe-O coordination geometries in the material that give rise to a distribution of energy levels during discharge.

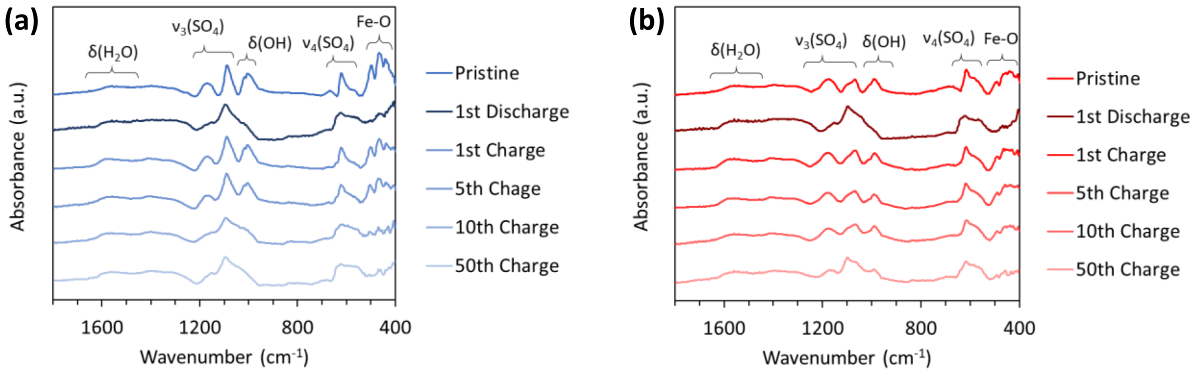

Figure 3-10. Ex situ FTIR spectra of (a) Na-jarosite and (b) Pb-jarosite electrodes at various cycles.

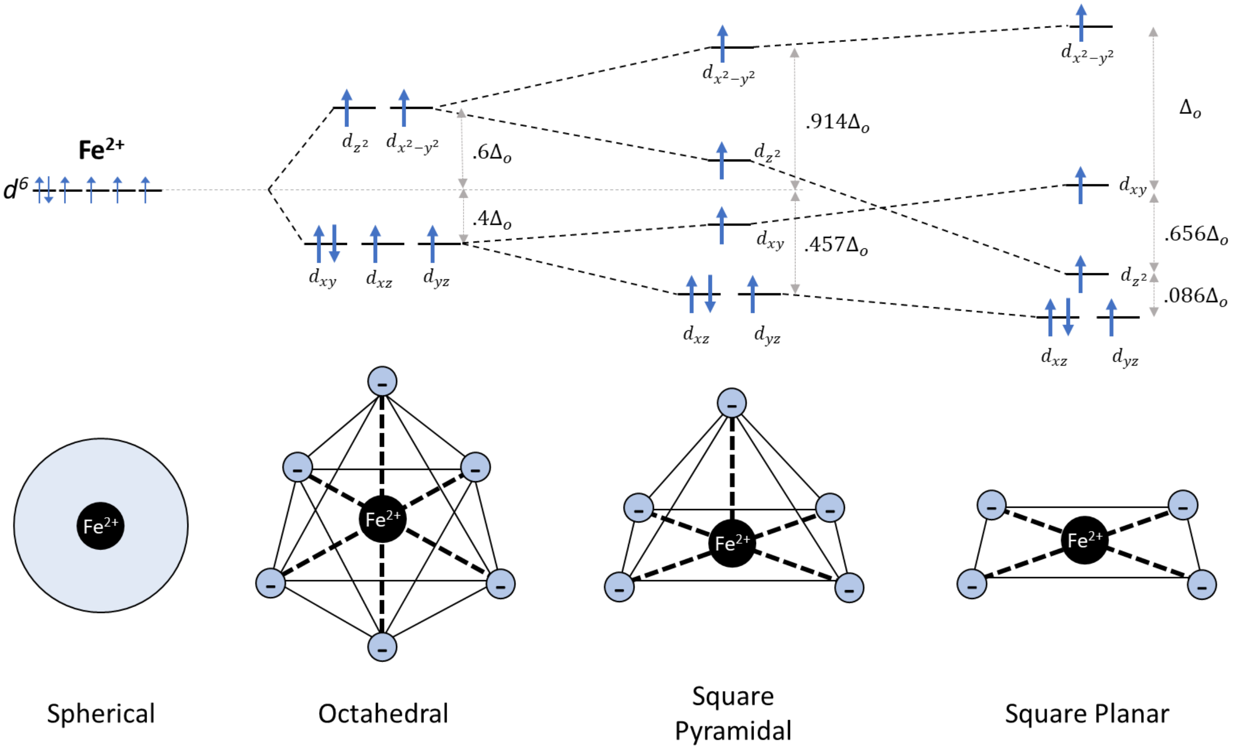

Figure 3-11. Orbital splitting of Fe^{2+} in different ligand coordinations.

Kinetics of Na-jarosite and Pb-jarosite

Pb-jarosite and Na-jarosite batteries were cycled at different C-rates to investigate the influence of lithium-ion kinetics (**Figure 3-12**). Na-jarosite displayed greater lithium-ion capacity at lower current rates but had more significant capacity drop off at higher rates than Pb-jarosite.

At slow current, it would be expected that Na-jarosite has higher capacity because of its higher theoretical specific capacity. Conversely, Pb-jarosite had superior capacity of 59 mAh/g at 1C compared to 28 mAh/g for Na-jarosite. The larger dependence on C-rate is indicative of more kinetically restricted behavior. The increased lithium capacity of Pb-jarosite at higher rates is likely attributed to increased lithium ion diffusion within the jarosite crystal due to increased vacancies and interlayer spacing.

Electrochemical impedance spectroscopy (EIS) of Na-jarosite and Pb-jarosite batteries further illustrate the improved kinetics of Pb-jarosite (**Figure 3-13**). EIS spectra show Pb-jarosite has a smaller charge transfer resistance indicated by the lower x-intercept of the large semicircle. Improved charge transfer could result from better electronic properties by substituting Pb for Na ions and introducing vacancies.

Furthermore, the low-frequency Warburg region of EIS spectra pertains to lithium ion diffusion. The lithium ion diffusion coefficient (D_{Li^+}) can be calculated using the following methodology proposed by Ho et al.:

$$D_{Li^+} = \frac{1}{2}\left[\left(\frac{V_M}{AF\sigma_W}\right)\frac{\delta E}{\delta x}\right]^2 \tag{3-1}$$

where V_{M} is the molar volume, A is the electrode/electrolyte surface area (simplified as the electrode area, 0.785 cm^2), F is the Faraday constant, and σ_W is the Warburg coefficient, which is determined from the slope of real impedance Z' vs the inverse square root of angular frequency $\omega^{-1/2}$ at low frequencies.[98] The parameter $\delta E/\delta x$ is estimated from the first plateau of the galvanostatic test in **Figure 3-6** as the change in potential vs lithium ion insertion. The resulting diffusion coefficients are 4.3×10^{-13} and 1.7×10^{-11} $\mathrm{cm}^2\ \mathrm{s}^{-1}$ for Na-jarosite and Pb-jarosite, respectively, thus showing Pb-jarosite to have two orders of magnitude faster diffusion. It should be noted that these are only nominal values due to the assumptions made about electrode/electrolyte interface, but the comparison should still be considered appropriate.

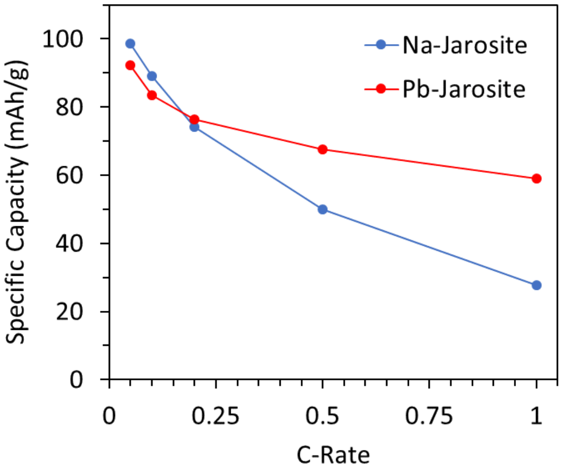

Figure 3-12. Discharge capacities of Na-jarosite and Pb-jarosite at different C-rates.

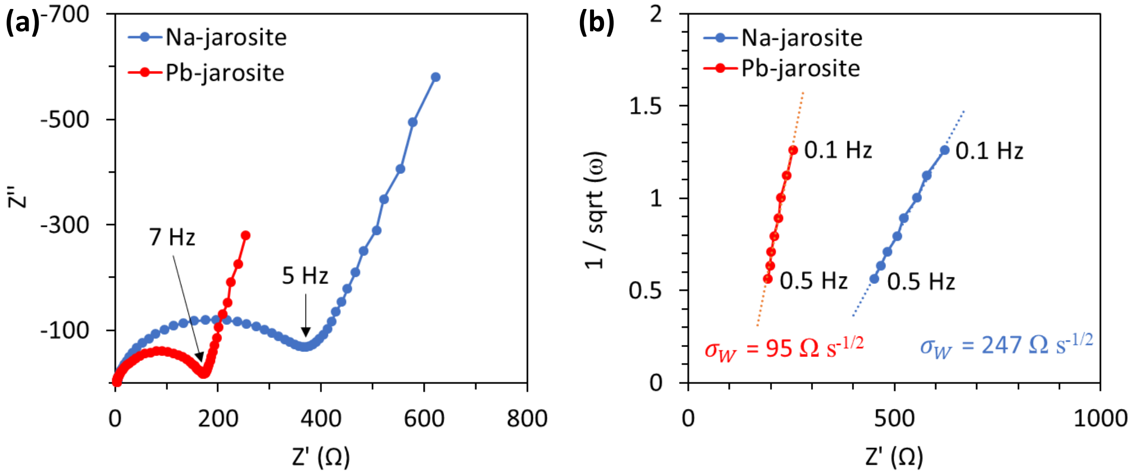

Figure 3-13. EIS spectra between 100 kHz and 0.1 Hz of lithium halfcell batteries before cycling (a) and their Warburg impedance at low frequency (b).

Potentiostatic intermittent titration technique (PITT) further corroborated the relationship of the lithium ion diffusion in Na-jarosite and Pb-jarosite. PITT measured the potentiostatic current response at 5mV steps starting from 4 V (**Figure 3-14**). The decay in current during a potentiostatic test can be modeled by the Cottrell equation to determine kinetic parameters such as diffusion coefficient. A fitting approximation developed by Vorotyntsev, et al. was used.[99] At early times when diffusion dominates the kinetics, the current is described by

$$I(t_{short}) = \frac{Q^{total}}{\tau_D/\Lambda + \sqrt{\pi\tau_D t}} \tag{3-2}$$

where Q^{total} is the total capacity per voltage increment, t is time, τ_D is the characteristic diffusion time which is equal to L^2/D where L is the characteristic particle size and D is the diffusion coefficient, and Λ is the ratio of the diffusion resistance to the external resistance. The parameters τ_D and Λ are determined graphically by finding the slope and intercept of the linear regression of $1/(I(t)\sqrt{t})$ versus $1/\sqrt{t}$ at early times.

$$m = \frac{\tau_D}{\Lambda Q^{total}} \tag{3-3}$$

$$b = \frac{\sqrt{\pi\tau_D}}{Q^{total}} \tag{3-4}$$

The parameters τ_D and Λ were found for each potential step and used to calculate diffusion coefficient (**Figure 3-15**).

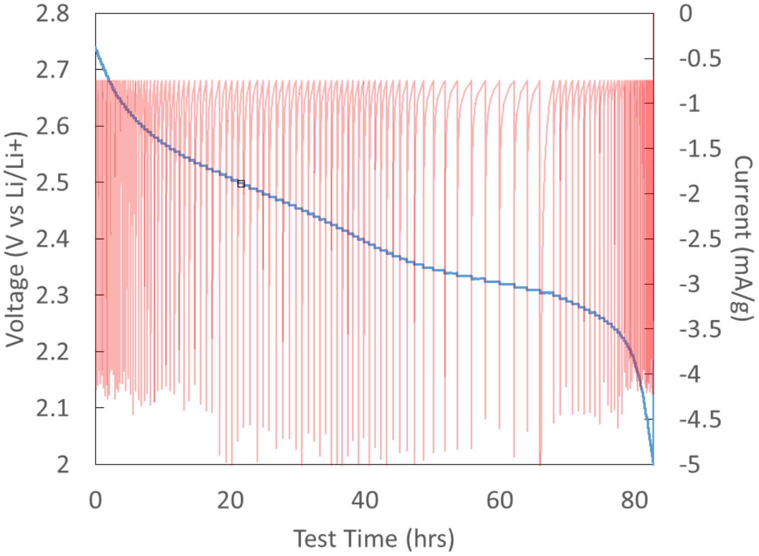

Figure 3-14. PITT current and voltage profile of Pb-jarosite.

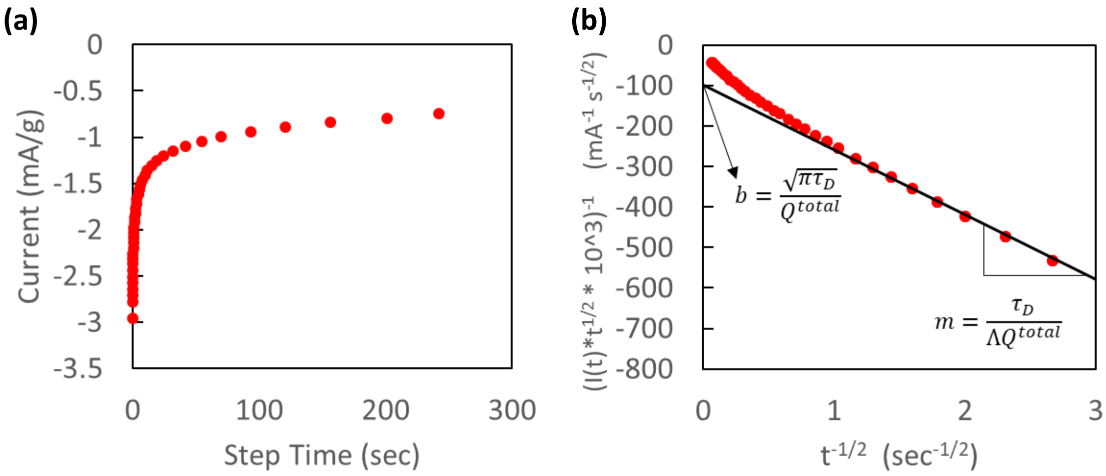

Figure 3-15. Example of single PITT step and graphical transformation to determine τ_D and Λ.

The calculated diffusion coefficient varies during lithium ion intercalation in Na-jarosite and Pb-jarosite (**Figure 3-16a**). In general, the weighted average diffusion coefficient when considering amount lithium intercalated at each potential step is 8.6×10^{-13} and 1.1×10^{-11} cm^2 s^{-1} for Na-jarosite and Pb-jarosite, respectively. The larger average diffusion coefficient over all lithium concentrations corroborates the improved capacity and rate performance of Pb-jarosite over Na-jarosite. However, Pb-jarosite exhibits lower lithium-ion diffusivity than Na-jarosite at lower lithium concentrations but increases to higher diffusivity upon further intercalation. This region of low diffusivity corresponds well with the large overpotential of Pb-jarosite during initial intercalation (**Figure 3-6d**).

An explanation to the large change in diffusion coefficient in Pb-jarosite could be the transition between lithium intercalation first into amorphous Pb-jarosite and its crystalline phase (**Figure 3-17**). It has already been shown that both jarosite materials undergo a semi-reversible crystalline-to-amorphous phase transformation upon lithium intercalation (**Figure 3-9**). The PITT test was preceded by two CCCP cycles which would have contributed to the formation of some amorphous

Pb-jarosite phase responsible for the initial low diffusivity. The amorphous phase would not receive the same benefits from vacancies due to its disordered structure. Additionally, the lower density of amorphous phase would result in larger hopping distances for lithium ions, further decreasing diffusivity. In contrast, Na-jarosite without vacancies does not receive the same boost in diffusivity for its crystalline phase.

PITT performed after 30 galvanostatic cycles at C/5 illustrates the growing amorphous environment for lithium diffusion (**Figure 3-16b**). Pb-jarosite retains a high diffusivity above 10^{-11} cm^2 s^{-1}, albeit throughout a smaller concentration range. Similarly, the range of low diffusivity increases but with higher diffusivity. In contrast, Na-jarosite exhibits a mostly unchanging diffusion coefficient during intercalation which is consistent with the diffusivity independence on lithium concentration in disordered materials because of less change in local environment during intercalation.[100] This supports the idea that Na-jarosite and Pb-jarosite are irreversibly transforming into a disordered phase through electrochemical cycling, with Pb-jarosite being more resilient to the irreversible transformation. The decreasing high diffusivity region corresponds with decreasing crystalline content of Pb-jarosite and increasing amorphous phase that does not receive the same boost in diffusivity from vacancies.

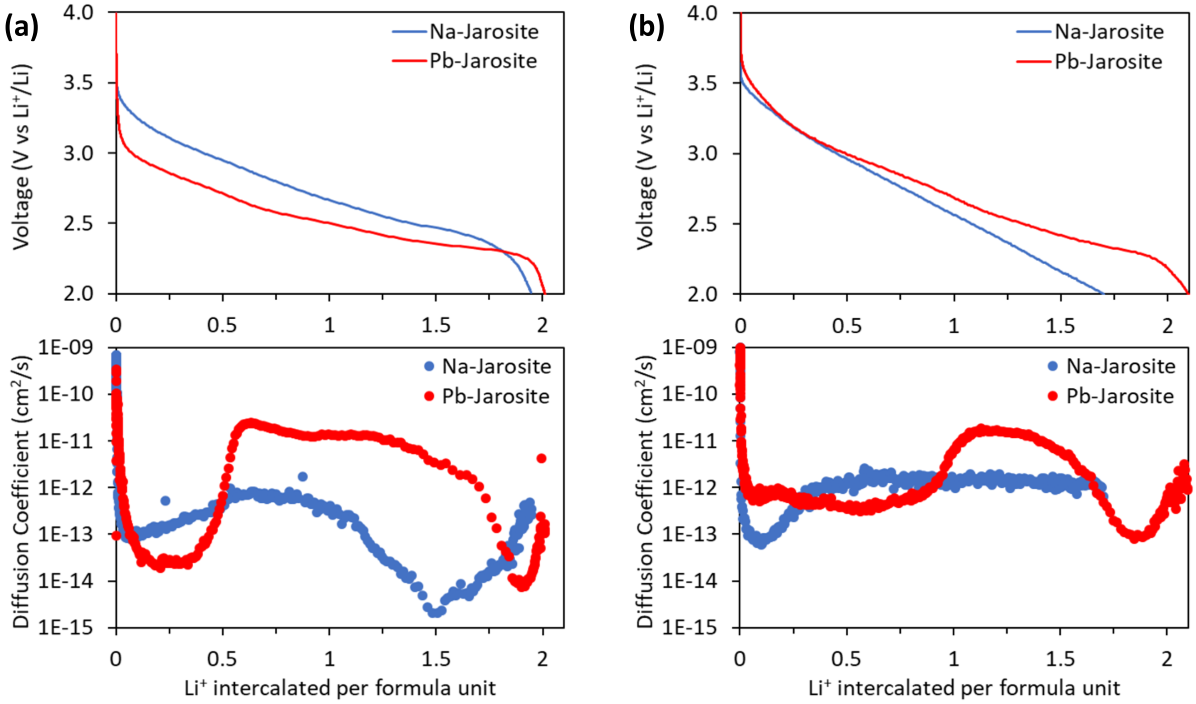

Figure 3-16. PITT discharge profile and calculated diffusion coefficient of Na-jarosite and Pb-jarosite before cycling (a) and after 30 galvanostatic cycles at C/5 (b). PITT was preceeded by two CCCP cycles.

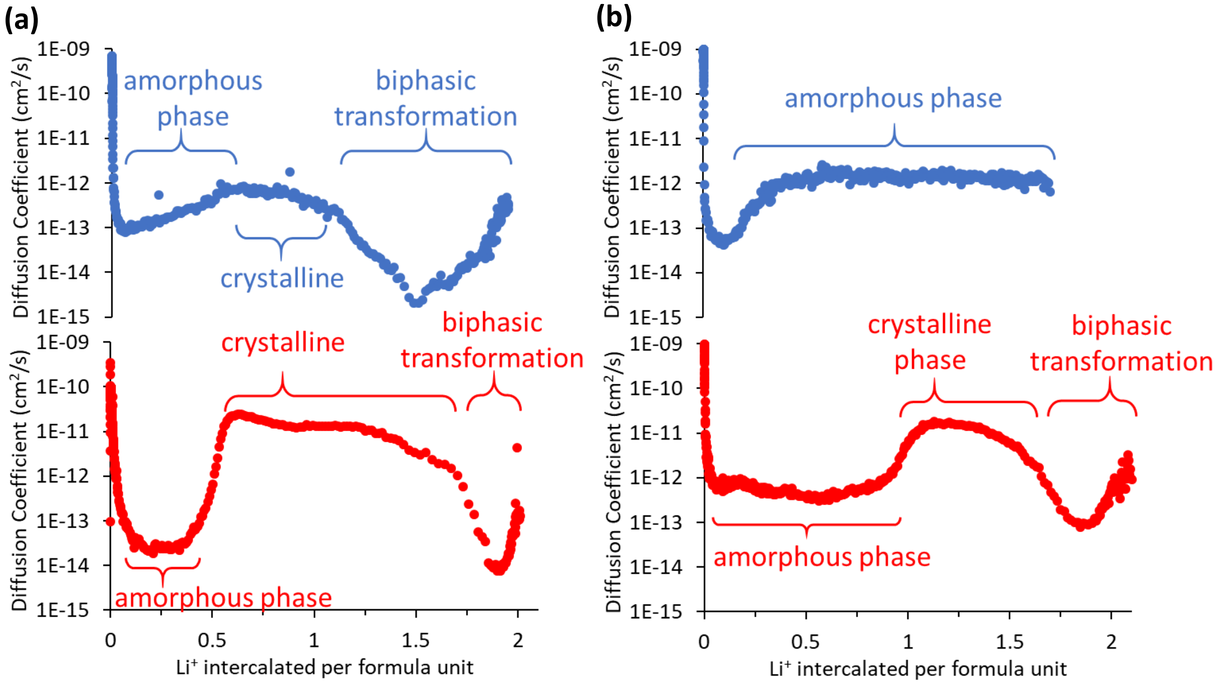

Figure 3-17. Proposed theory for transitioning diffusion coefficients in Na-jarosite and Pb-jarosite after 2 CCCP cycles (a) and after 30 galvanostatic cycles (b).

Diffusivity results from PITT of batteries after 30 galvanostatic cycles were validated by performing EIS at various depths of discharge. EIS was performed on batteries after intermitant steps of galvanostatic discharge at a rate of C/20 for 1 hour followed by 1 hour of open circuit rest (**Figure 3-18**). Diffusion coefficient after each step was determined from the Warburg impedance using **equation (3-1)**. The corresponding diffusivity vs lithium intercalation profile matches the trend in diffusivity determiend by PITT; albiet diffusivity values are about an order of magnitude higher when determiend by EIS (**Figure 3-19**). The higher diffusivity values determined by EIS is likely caused by the assumptions made about electrode surface area in its calcualtion. While it is typical to assume electrode surface area is the plane area of the current collector, in reality the active electrode surface area of may be significantly larger due to particle geometry and electrode thickness. A larger surface area value would decrease the diffusivity results from this calculation, coming closer to the values determiend by PITT. Nonetheless, the similarity between two different methods of calculating diffusivity helps to validate the general trend in lithium ion diffusivity as a function of lithium ion intercalation in Na-jarosite and Pb-jarosite.

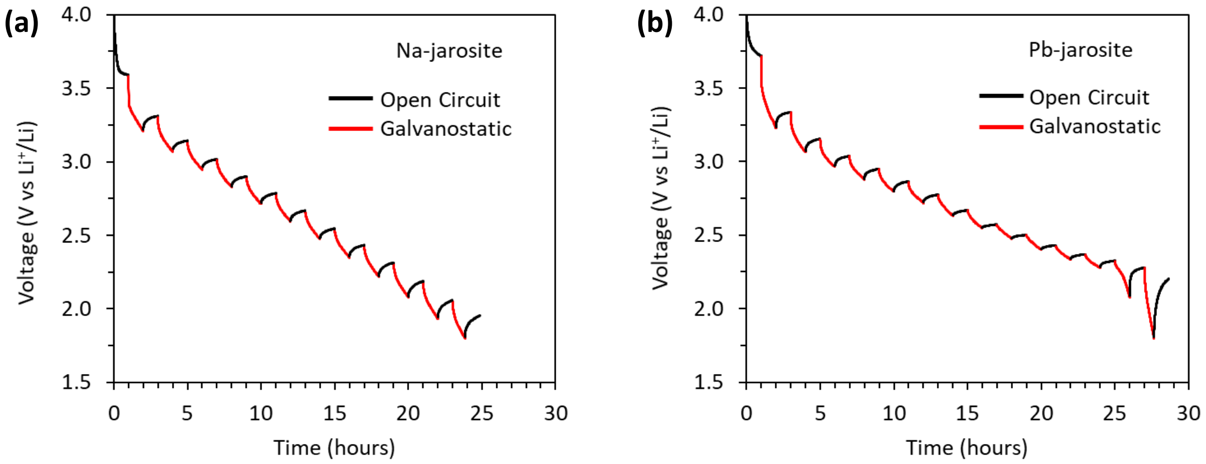

Figure 3-18. Galvanostatic intermittant titration profiles for Na-jarosite (a) and Pb-jarosite (b) after 30 cycles and PITT. Galvanostatic discharge was done at a current rate of C/20 for 1 hour followed by open circuit rest for 1 hour.

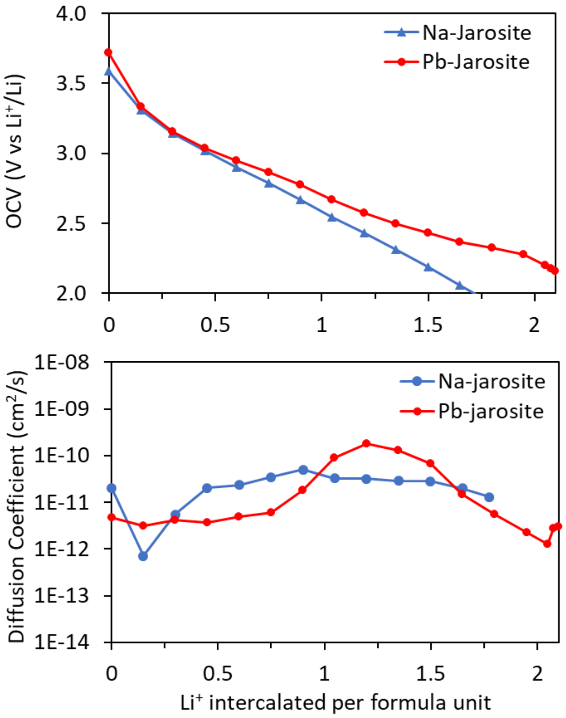

Figure 3-19. Open circuit voltage profile after resting during intermittant galvanostatic discharge (top) and calculated diffusivity (bottom) for Na-jarosite and Pb-jarosite determined from EIS at each open circuit rest step.

3.4 Conclusions

Lithium ion intercalation into synthetic Pb-jarosite was investigated and compared to its Na-jarosite analog. Substituting Pb^{2+} for Na^{+} in the synthesis of jarosite results in the formation of cation vacancies that help contribute to improved lithium ion diffusion of its crystalline phase. Despite having a lower theoretical specific capacity, Pb-jarosite demonstrated increased lithium-ion uptake at competitive rates attributed to faster diffusion kinetics and lower charge transfer resistance. However, average diffusivity in Pb-jarosite decreases due to the accumulation of amorphous phase from a semi-reversible crystalline-to-amorphous phase transformation during lithium intercalation over several cycles.

This work helps contribute to the understanding of solid ionic diffusion in jarosite materials with unique amorphous phase transformation over many cycles. The characterization of Pb-jarosite having higher lithium ion diffusivity and capacity helps to open the possibility of recycling jarosite waste materials in energy storage applications. Additionally, it suggests that utilizing mixed jarosite waste material with higher Pb content would be more desirable.

Reproduced in part with permission from Royal Society of Chemistry Copyright 2020.
Neale, Z. G.; Liu, C.; Cao, G. Effect of synthesis pH and EDTA on iron hexacyanoferrate for sodium-ion batteries. Sustainable Energy & Fuels 2020, 4 (6), 2884–2891. https://doi.org/10.1039/d0se00120a.

Chapter 4: Room temperature synthesis of crystalline iron hexacyanoferrate through EDTA chelation

Iron hexacyanoferrate (FeHCF) is synthesized at room temperature with the addition of EDTA to produce highly crystalline faceted particles compared to nanoparticles synthesized without. The highly crystalline particles have fewer $Fe(CN)_6$ anion vacancies and improved electrochemical activity.

4.1 Introduction

In general, there are two routes to chemically synthesizing FeHCF. First is through a two-precursor method, utilizing an iron salt and sodium ferrocyanide. The precipitation reaction at room temperature between free iron ions and ferrocyanide complex is rapid. The solubility product of FeHCF was determined to be 10^{-257}, suggesting that nucleation of this phase due to supersaturation is incredibly rapid.[101] The fast nucleation kinetics results in nanoparticles with poor crystallinity, low initial Na^+ concentration, high vacancies, and high water content.[74] In contrast, high quality FeHCF crystals can be grown through a one-pot synthesis route in which a single precursor, such as sodium ferrocyanide, is slowly decomposed with hydrochloric acid or a hydrothermal treatment to produce free iron ions that can react with undecomposed ferrocyanide ions.[71,74,102] This route produces highly crystalline FeHCF particles that have improved capacity and cyclability compared to nanoparticles prepared by simple mixing.[74] However, the one-pot synthesis route creates hazardous cyanide as a byproduct, generating six moles of cyanide per mole of FeHCF. Furthermore, this route does not easily allow for the doping or substitution of the *M* species with other transition metals due to the fast precipitation between ferrocyanide and

Reproduced in part with permission from Royal Society of Chemistry Copyright 2020.
Neale, Z. G.; Liu, C.; Cao, G. Effect of synthesis pH and EDTA on iron hexacyanoferrate for sodium-ion batteries. Sustainable Energy & Fuels 2020, 4 (6), 2884–2891. https://doi.org/10.1039/d0se00120a.

transition metal ions. Therefore, it is important to investigate new synthesis routes that avoid cyanide generation and can allow M species substitution at room temperature while retaining a highly crystalline structure.

It was hypothesized that ethylenediaminetetraacetic acid (EDTA) would inhibit fast nucleation of FeHCF during simple mixing of ferrous chloride and sodium ferrocyanide precursors, thus increase particle crystallinity and improve electrochemical performance. Retarding nucleation would allow more controlled growth of the crystal as previously shown by the citrate molecule for FeHCF, Ni/MnHCF, and CoHCF.[75,103,104] EDTA is a hexadentate chelating agent commonly used in industry to suppress the activity of metal ions in solution and is a strong chelator of Fe ions.[105] It forms complexes with metal ions through two amine groups and four carboxyl groups. Due to the pH dependence of deprotonation the synthesis pH was held constant through a buffer. Preliminary studies determined a pH of 3.8 proved suitable for experiment.

4.2 Experimental Procedures

Synthesis of FeHCF

A 0.3M acetate buffer solution was prepared with sodium acetate and acetic acid at pH 3.8. Two separate 200 mL solutions of 20 mM $\mathrm{Na_4Fe(CN)_6 * 10H_2O}$ and 30 mM $\mathrm{FeCl_2 * 4H_2O}$ were prepared from the buffer solution. Sufficient time was allowed for both solutions to fully dissolve, after which the $FeCl_2$ solution was quickly added to the former solution while stirring. The solution was mixed for 24 hours before particles were collected and washed with water and ethanol through centrifugation. The blue product was dried in air at 80^{o}C overnight. For EDTA-synthesized particles the same procedure was used with the addition of 30 mM ethylenediaminetetraacetic acid tetrasodium salt to the $FeCl_2$ solution. Herein samples made without EDTA will be labeled as PB-1 and samples made with EDTA will be labeled PB-2.

Reproduced in part with permission from Royal Society of Chemistry Copyright 2020.
Neale, Z. G.; Liu, C.; Cao, G. Effect of synthesis pH and EDTA on iron hexacyanoferrate for sodium-ion batteries.
Sustainable Energy & Fuels 2020, 4 (6), 2884–2891. https://doi.org/10.1039/d0se00120a.

Physical Characterization

The crystal structure of the as-synthesized products were determined via powder X-ray diffractometry (XRD) on a Bruker D8 Discover using a Cu-K X-ray source with nickel filter and a 1-dimensional x-ray transducer. A JSM 7000F scanning electron microscope was used in SEI mode to collect electron micrographs. SEM samples were prepared by drop casting FeHCF-water suspensions onto silicon substrates and drying at 80^{o}C under vacuum. The optical absorbance was measured using a UV-vis spectrometer. Thermal gravimetric analysis (TGA) was performed on samples under nitrogen gas at 5^{o}C/min. Exhaust gas from TGA was filtered through a 0.1M ferrous sulfate water trap to capture any cyanide gas generated. Total carbon, hydrogen, and nitrogen content (CHN) was determined using a Perkin Elmer CHN 2400 series analyzer.

Electrochemical Characterization

Electrodes were made on aluminum foil by doctor blading a slurry of 70% active material, 20% Super P conductive carbon, and 10% sodium carboxymethylcellulose (CMC) binder dissolved in water. The aluminum foil was cleaned with 0.1 M oxalic acid solution and ethanol before doctor blading. The electrodes were dried under vacuum at 80^{o}C for 12 hours before punching into 10mm diameter disks. After measuring mass, the electrodes were transferred into an argon filled glove box with oxygen and water concentration below 0.5 ppm. Sodium half-cells were made with CR2032 type coin cells with a sodium metal anode and Whatman glass fiber separator saturated with 1M $NaClO_4$ in PC with 5% FEC electrolyte solution. Batteries for cyclic voltammetry did not include FEC additive in their electrolyte. Galvanostatic cycling was done on a LAND battery tester between 2 and 4.3V. Cyclic voltammetry was performed with an Arbin electrochemical tester between 2 and 4.3V at 0.1mV/s.

Reproduced in part with permission from Royal Society of Chemistry Copyright 2020.
Neale, Z. G.; Liu, C.; Cao, G. Effect of synthesis pH and EDTA on iron hexacyanoferrate for sodium-ion batteries. Sustainable Energy & Fuels 2020, 4 (6), 2884–2891. https://doi.org/10.1039/d0se00120a.

4.3 Results and Discussion

Physical Characterization

XRD patterns of PB-1 and PB-2 (**Figure 4-1**) both closely match the cubic $Fm\bar{3}m$ crystal structure of Prussian blue. The diffraction peaks of PB-2 grown with EDTA are stronger in intensity and have smaller peak width compared to PB-1 grown without EDTA, indicating that PB-2 consists of larger crystals. The peak position of the (200) plane is slightly smaller for PB-2, indicating a larger lattice constant of 10.24Å compared to 10.17Å for PB-1. The average crystallite size using the Scherrer equation was estimated to be 51 and 116 nm for PB-1 and PB-2, respectively. SEM images (**Figure 4-2**) show that particles synthesized with EDTA display cubic morphology and agree with the estimation of crystal size by XRD.

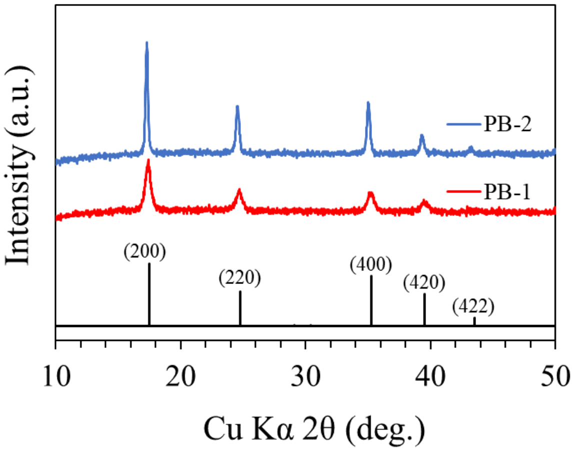

Figure 4-1. XRD pattern of PB-1 (without EDTA) and PB-2 (with EDTA) compared against ICDD No. 00-052-1907 for Prussian blue.

Reproduced in part with permission from Royal Society of Chemistry Copyright 2020.
Neale, Z. G.; Liu, C.; Cao, G. Effect of synthesis pH and EDTA on iron hexacyanoferrate for sodium-ion batteries. Sustainable Energy & Fuels 2020, 4 (6), 2884–2891. https://doi.org/10.1039/d0se00120a.

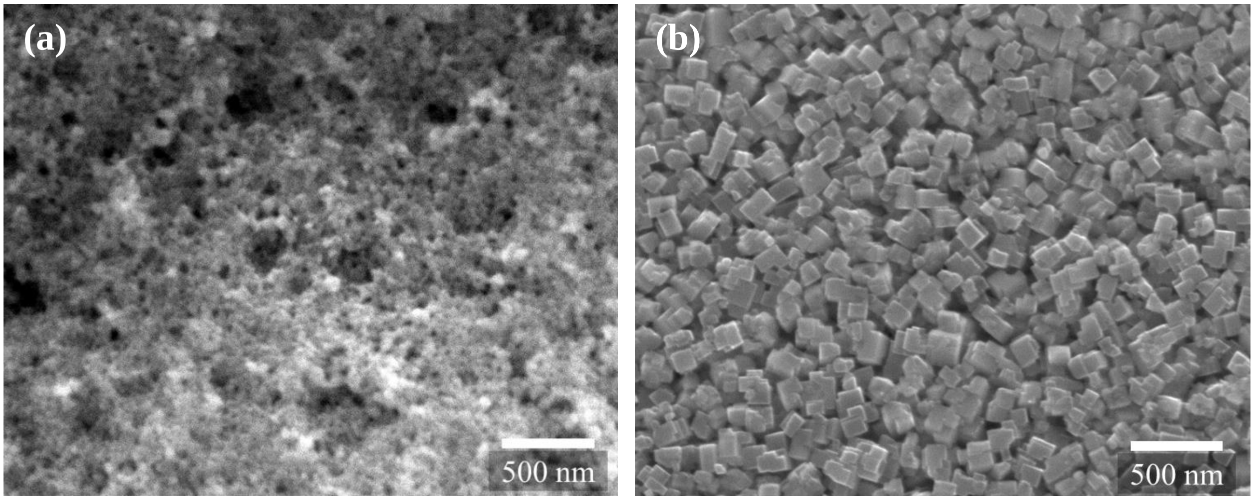

Figure 4-2. SEM images of PB-1 (a) and PB-2 (b).

The crystal structure of FeHCF is typically associated with zeolitic water and water coordinated to high-spin Fe in place of $[\mathrm{Fe(CN)_6}]$ anion vacancies. TGA and CHN elemental analysis can elucidate the amount of water in the FeHCF lattice. TGA results up to 400^{o}C (**Figure 4-3**) show an initial weight loss of about 23 and 16% for PB-1 and PB-2, respectively, followed by a second weight loss step of 13 and 6%. The first weight loss step is associated with the loss of water and the second step is the partial decomposition of $Fe(CN)_6$ groups.[106] CHN elemental analysis results (**Table 4-1**) for total hydrogen correlates well with TGA results. Assuming all hydrogen corresponds to water in the sample, CHN analysis returns 22 and 17 wt% H_2O respectively for PB-1 and PB-2. The similarity between TGA and CHN indicate that the first weight loss step is attributed to both zeolitic water and coordinated water. The higher carbon weight percentage in PB-2 corroborate this speculation. These results allude that the addition of EDTA to FeHCF synthesis decreases water content and vacancy concentration.

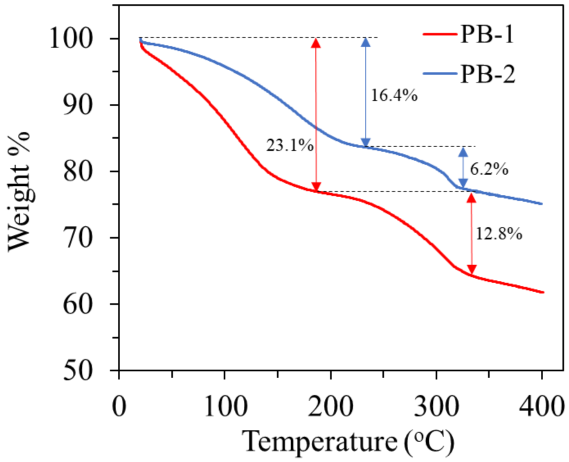

Figure 4-3. TGA of as-synthesized FeHCF powders under nitrogen at 5°C/min.

Table 4-1. Elemental analysis results for carbon, hydrogen, and nitrogen.

Sample	Weight %		
	C	H	N
PB-1	19.7	2.5	21.3
PB-2	21.1	1.9	24.2

Mössbauer spectroscopy was performed to better understand the structure of FeHCF grown with EDTA. Mössbauer spectroscopy is a characterization technique that uses gamma ray absorption to probe the chemical environment of iron species in materials. The source of gamma rays comes from a radioactive Co-57 source that decays into Fe-57 with an excited nuclear state through electron capture (**Figure 4-4**). The excited state of Fe-57 lowers its energy through emission gamma rays. Fe-57 in the sample absorb these gamma rays, but the energy of resonant absorbance is influenced by the local chemical environment of iron in the sample. To change the gamma ray energy the source is linearly actuated towards and away the sample target at constant acceleration (**Figure 4-5**). The positive and negative velocities of the gamma ray emitting source correspond to blue-shift and red-shift of gamma rays due to the Doppler effect, in which 1 mm/s velocity corresponds to an energy shift of 48.075×10^{-9} eV. For example, if the absorbing Fe species in the sample has the same chemical environment as the iron emitting gamma rays, then there would be an absorption peak at 0 mm/s. A different chemical environment of the absorber species can lead to an isomer shift, δ, away from 0 mm/s which is influenced by electron density at the nucleus and change in nuclear radius between the excited and ground state (negative for Fe-57). The nuclear energy level is affected by *s*-character bonding of the species and electron screening of the nucleus by *p* and *d* electrons. Therefore, a positive isomer shift would be expected for Fe^{3+} with fewer *s*-electrons compared to Fe^0, and a greater positive shift for Fe^{2+} which has greater electron screening by *d* electrons. Furthermore, the shape of nuclear charge distribution of the absorber species can be affected by coordinated ligands and valence state which can lead to quadrupole splitting of absorbance peaks (**Figure 4-6**). For example, a uniform electric field gradient of octahedrally coordinated high-spin Fe^{3+} or low-spin Fe^{2+} will not result in quadrupole splitting of peaks. However, a non-uniform electric field gradient such as in high-spin Fe^{2+} or low-spin Fe^{3+}, or when there is a non-uniform ligand field coordinated to Fe, then the singlet absorbance peak will turn into a doublet.

Reproduced in part with permission from Royal Society of Chemistry Copyright 2020.
Neale, Z. G.; Liu, C.; Cao, G. Effect of synthesis pH and EDTA on iron hexacyanoferrate for sodium-ion batteries. Sustainable Energy & Fuels 2020, 4 (6), 2884–2891. https://doi.org/10.1039/d0se00120a.

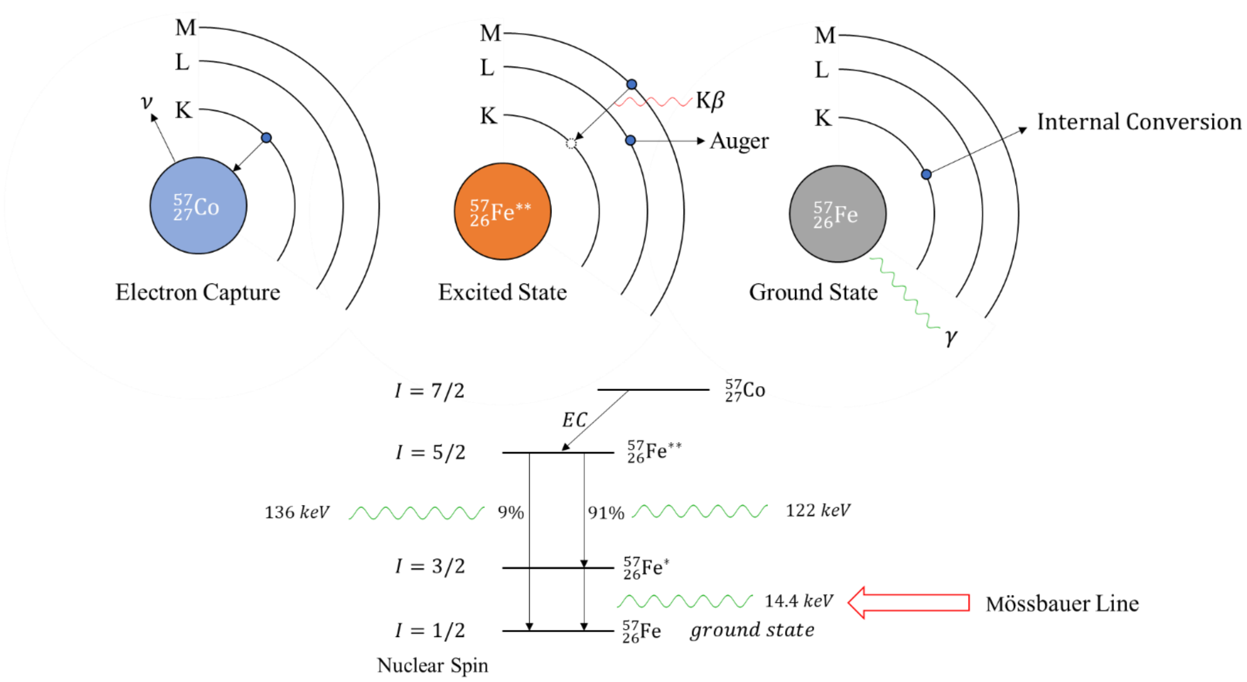

Figure 4-4. Nuclear decay of Co-57 and emission of Mössbauer gamma rays from Fe-57.

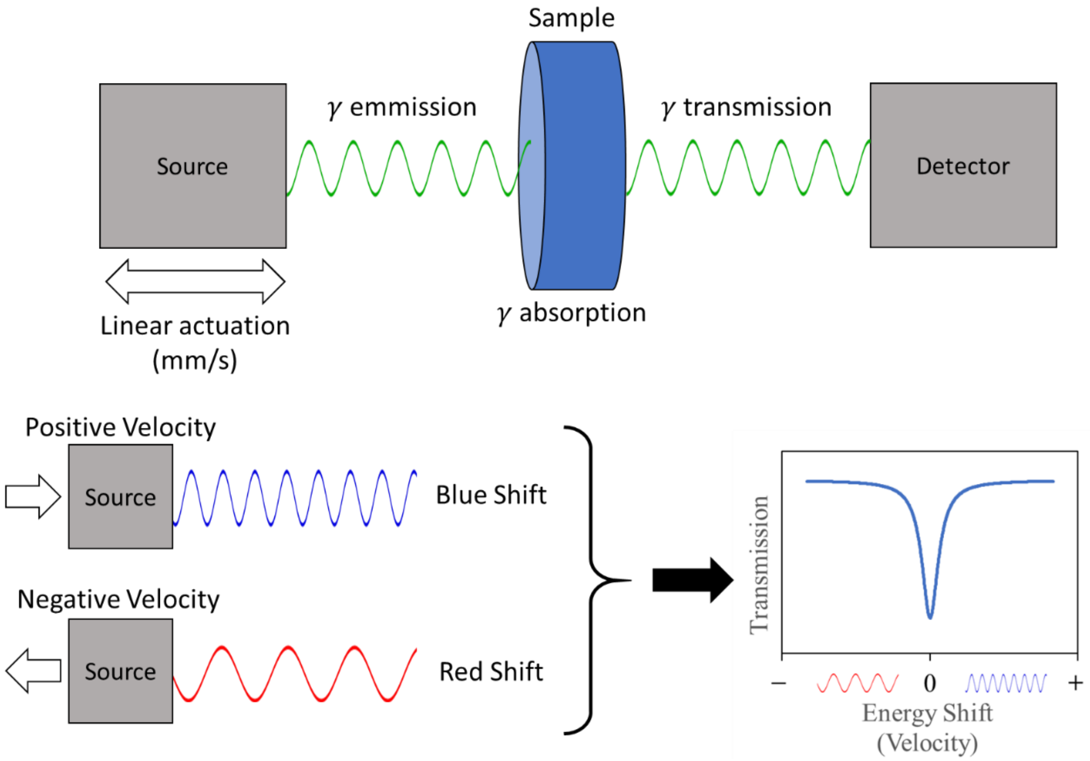

Figure 4-5. Diagram of working principle of Mössbauer spectroscopy.

Reproduced in part with permission from Royal Society of Chemistry Copyright 2020.
Neale, Z. G.; Liu, C.; Cao, G. Effect of synthesis pH and EDTA on iron hexacyanoferrate for sodium-ion batteries. Sustainable Energy & Fuels 2020, 4 (6), 2884–2891. https://doi.org/10.1039/d0se00120a.

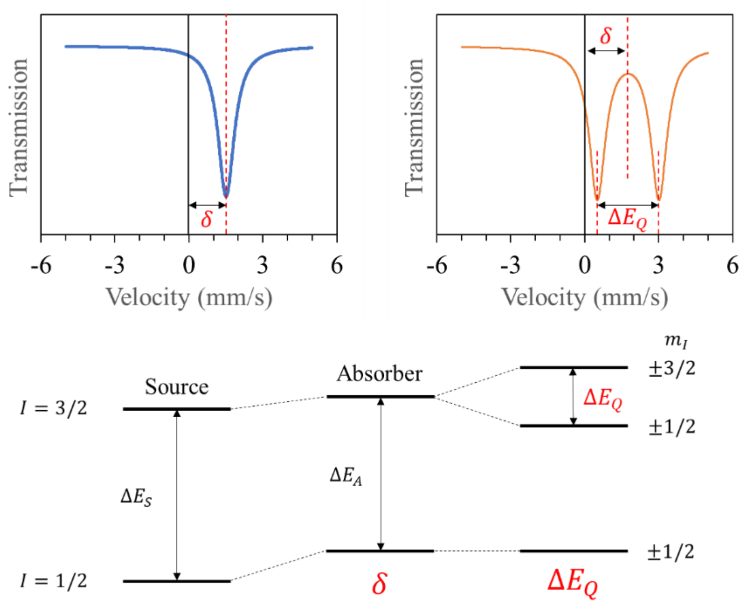

Figure 4-6. Isomer shift and quadrupole splitting due to different chemical environment of absorber species and non-uniform electric field influencing nuclear energy level of Fe species.

Mössbauer spectroscopy was performed at room temperature using a Co-57 source and calibrated to α-Fe. The nuclear resonance of Fe-57 atoms in FeHCF are sensitive to their local chemical environment and valence state. The Mössbauer spectra (**Figure 4-7**) can be fitted with Lorentzian curves representing each iron species and the area of the curve is proportional to the molar fraction of that species. Using the same fitting methodology as Grandjean et al., a single doublet was assigned to low-spin Fe(II), and three doublets were assigned to high-spin Fe(III) with their line widths, Γ, held equal to that of the α-Fe calibration of about 0.34 mm/s.[107] Although one doublet could be assigned to high-spin Fe(III), it was found that the fitted curve would produce line widths much larger than that of α-Fe. This is because the presence of low-spin [Fe(CN)$_6$] vacancies create several chemically unique identities of high-spin Fe(III) which would increase the line width of a composite doublet fitting curve. The fitting parameters of each curve are listed in **Table 4-2**.

The curve area ratios between high-spin and low-spin iron species are approximately 2:1 and 1.2:1 for PB-1 and PB-2, respectively. These ratios correspond to an estimated 50% and 18% $[\mathrm{Fe(CN)}_6]$ anion vacancies in the FeHCF lattice. The measured anion vacancies for PB-1 are higher than what is typically reported for Prussian Blue and other metal hexacyanoferrates, that is less than 33%.[72,108,109] Surface effects could influence the results with increasing effect for smaller particles; however, a cubic FeHCF particle of 50 nm in width only has 6% of its atoms on the surface. Another explanation could be that the recoil-free factors, the *f*-factors, for the different iron species is not the same which would affect the measured absorption.[107] Another concern is that FeHCF with such high anion vacancies would not be able to maintain charge neutrality according to the traditional chemical formulation of Prussian Blue, but could be possible if OH^- anions were present as proposed by Bueno, et al.[72] Regardless, the Mössbauer data clearly indicates an increase in low-spin Fe concentration of PB-2 which corroborates with the increased carbon weight percentage results from CHN analysis.

The decreased weighted quadrupole splitting, $\langle \Delta E_Q \rangle$, of the high-spin Fe(III) doublets indicate a more symmetric ligand environment of PB-2, likely due to a decrease in $[\mathrm{Fe(CN)}_6]$ vacancies. The decreasing $\langle \Delta E_Q \rangle$ is also supported by the increasing isomer shift, δ, of both low-spin and high-spin Fe. The isomer shift is sensitive to *s*-electron density, with more negative velocity for increasing *s*-electron density at the nucleus of Fe atoms.[110] High-spin Fe in FeHCF is coordinated to the highly electronegative nitrogen of $[\mathrm{Fe(CN)}_6]$. When $[\mathrm{Fe(CN)}_6]$ ligands are replaced by coordinated water which is less electronegative, the *s*-electron density at the nucleus of high-spin Fe increases resulting in a negative isomer shift. Similarly, the increased electron density of high-spin Fe pulls cyanide ligands closer to it, thus increasing the *s*-electron density of low-spin Fe atoms causing the relative negative shift in δ for PB-1. These results corroborate with the higher

Reproduced in part with permission from Royal Society of Chemistry Copyright 2020.
Neale, Z. G.; Liu, C.; Cao, G. Effect of synthesis pH and EDTA on iron hexacyanoferrate for sodium-ion batteries. Sustainable Energy & Fuels 2020, 4 (6), 2884–2891. https://doi.org/10.1039/d0se00120a.

water content of PB-1 determined by TGA and CHN analysis due to increased coordinated water in vacant sites resulting in decreased octahedral symmetry of high-spin Fe ions.

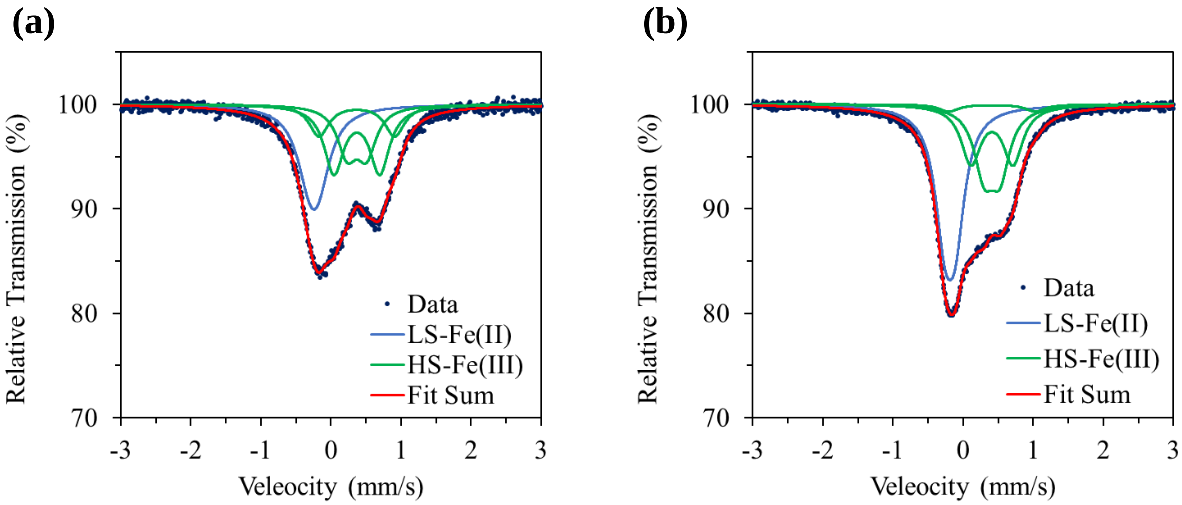

Figure 4-7. Mössbauer spectra at room temperature of (a) PB-1 and (b) PB-2 with fitted Lorentzian curves representing iron species.

Table 4-2. Fitting parameters for Mössbauer spectra. $\boldsymbol{\delta}$ is the isomer shift relative to $\boldsymbol{\alpha}$-Fe in mm/s, $\boldsymbol{\Delta E_Q}$ is the quadrupole splitting in mm/s, and **Γ** is the full line width at half max in mm/s. The quadrupole splitting displayed for high-spin Fe(III) is the weighted average of the three doublets.

	Low-Spin Fe(II)				High-Spin Fe(III)			
	δ	ΔE_Q	Γ	Area %	δ	$\langle \Delta E_Q \rangle$	Γ (fixed)	Area %
PB-1	-0.24(0)	0.13(2)	0.43(2)	33	0.37(0)	0.21(0)	0.34	67
PB-2	-0.19(0)	0.15(0)	0.34(0)	45	0.41(0)	0.15(0)	0.34	55

UV-visible light absorbance spectroscopy was performed on FeHCF samples diluted in water to an approximate concentration of 0.4 and 0.1 mg/mL for PB-1 and PB-2, respectively. The absorbance spectra match that of Prussian blue pigments with a main absorption peak at 700nm.[108] The light absorption in the visible range is associated with charge transfer between Fe(II) and Fe(III) ions. The higher absorption in PB-2 despite lower concentration could arise from a more even ratio of Fe(II)/Fe(III) ions to facilitate charge transfer.

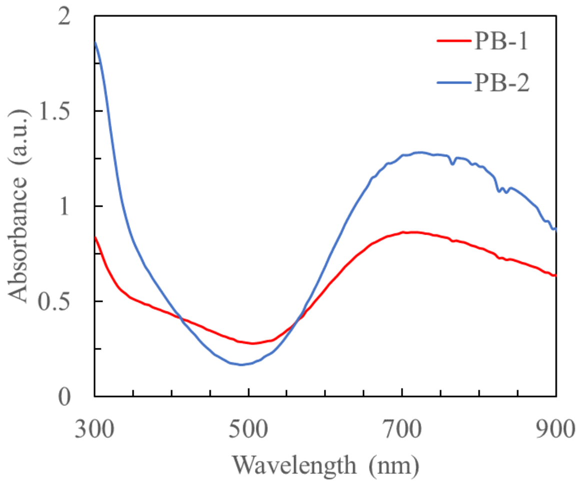

Figure 4-8. UV-vis absorbance spectra. Sample concentration was approximately 0.4 mg/mL for PB-1 and 0.1 mg/mL for PB-2.

Electrochemical Results

Cyclic voltammetry (CV) (**Figure 4-9**) reveals several redox peaks corresponding to sodium ion intercalation and deintercalation. PB-1 has broad peaks, possibly indicating that its iron redox sites vary with energy due to high vacancy concentration and surface defects. In contrast, PB-2 displays sharper, more distinct redox peaks, an indication that redox sites are more uniform in chemistry.

PB-2 possess an additional reduction peak at 3.8 V. This high-voltage reduction peak is also observed in other FeHCF non-aqueous systems when water content is high,[71] but is absent when the crystal is dehydrated which only shows the peak at 3.3 V (**Figure 4-10**).[111] Similarly, sodium ion intercalation in FeHCF of aqueous systems demonstrate a high redox potential corresponding to about 3.9 V vs Na^+/Na, but are absent of the peak at 3.3 V.[102] The potential during intercalation is not only affected by the crystal field energy of Fe^{3+}, but also the interaction energy between intercalant and host crystal, and the repulsive energy between intercalated ions.[112] It is apparent that the crystalline water content strongly influences the energy interaction between sodium ions and host crystal. On the other hand, PB-1 does not show the high voltage reduction peak although its water content is also supposedly high. One explanation is that the nanosized PB-1 particles are dehydrated during the thermal preparation of electrodes due to its lower dehydration temperature according to TGA. Additionally, electrochemical dehydration of the crystal will occur when cycling to 4.3 V,[71] which is evidenced by the large anodic current above 4 V during the first cycle and the disappearance of the reduction peak at 3.8 V during subsequent cycles in PB-2.

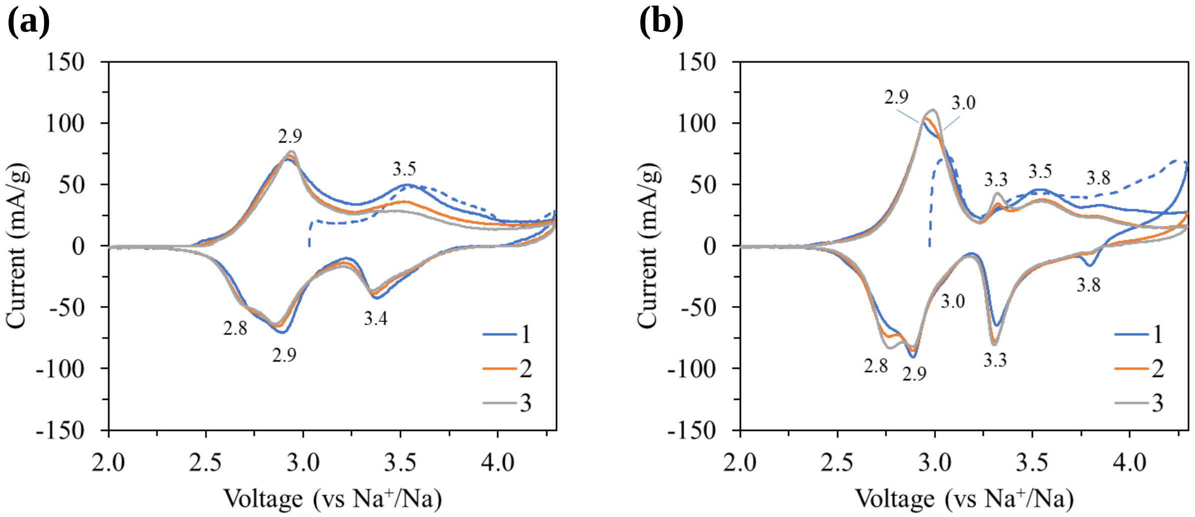

Figure 4-9. Cyclic voltammetry at 0.1 mV/s of (a) PB-1 and (b) PB-2. Dotted line indicates the initial charge cycle.

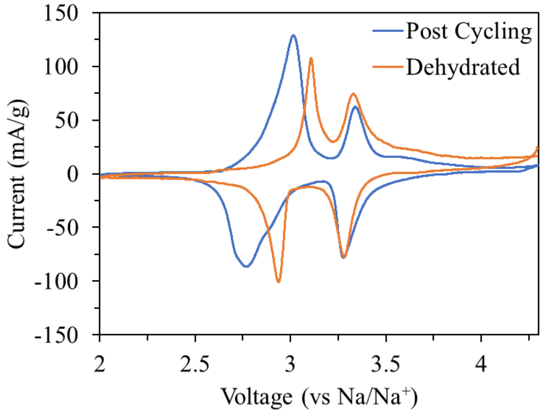

Figure 4-10. Cyclic voltammetry of PB-2 after galvanostatic cycling at 100 mA/g for 100 cycles versus the first cycle of a PB-2 electrode dehydrated at 200°C under N_2 for 1 hour.

Galvanostatic cycling was performed on sodium metal half cells at 100 mA/g (**Figure 4-11**). The initial charge cycle (dotted line) capacity is slightly higher for PB-2. The initial charge cycle corresponds to the initial Fe^{2+} available for oxidation, or possibly oxidation of coordinated water. The first cycle discharge capacities were 111 and 151 mAh/g for PB-1 and PB-2, respectively.

Upon further cycling PB-1 and PB-2 suffer from gradual capacity decay (**Figure 4-12**). The average coulombic efficiencies (discharge / charge) after the 3rd cycle up to 100 cycles are 98 and 99% for PB-1 and PB-2, respectively. An efficiency less than 100% corresponds to extra capacity gained during oxidation. The oxidation of zeolitic and crystalline water maybe attribute to this inefficiency. Additionally, FeHCF has been shown to oxidize electrolyte forming a cathode electrolyte interface (CEI) at high voltages.[113] If the CEI layer is unstable then further electrolyte may decompose on every cycle contributing to coulombic efficiencies below 100%. PB-2 also demonstrates less capacity decay after the 3rd cycle, with a capacity retention of 83% up to 100 cycles. In contrast, PB-1 had lower capacity retention at 79%. The increased coulombic efficiency and cyclic stability of PB-2 may be a result of its larger particle size allowing for a more stable

CEI layer or from fewer side reactions at the electrolyte interface due to its lower specific surface area.

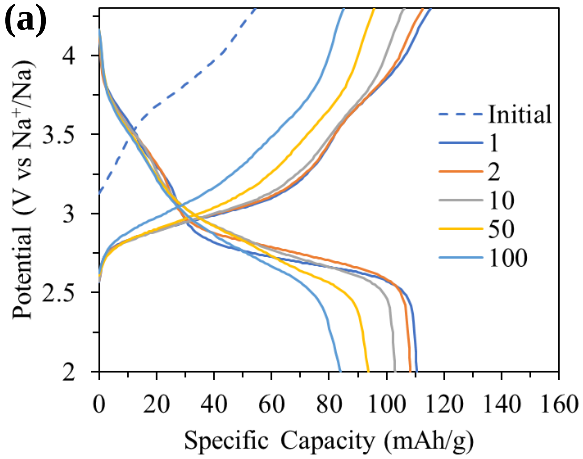

Figure 4-11. Galvanostatic profile at 100 mA/g of the initial charge and subsequent cycles for (a) PB(3.8), (b) PB(4.4), (c) EDTA(3.8), and (d) EDTA(4.4).

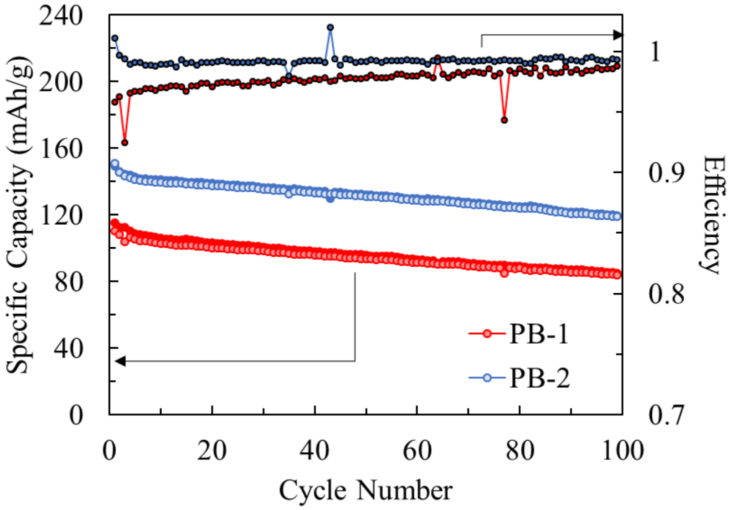

Figure 4-12. Galvanostatic cycling at 100 mA/g. Discharge shown as open circles and charge shown as filled circles.

The intercalation kinetics of FeHCF samples were investigated by cycling batteries at various current densities (**Figure 4-13**). The specific discharge capacities at a current density of 3.2 A/g were 63 and 122 mAh/g, corresponding to capacity retentions of 56 and 85% respectively for PB-

1 and PB-2 compared to their 4th cycle. The high capacity retention at high current of PB-2 indicates fast intercalation kinetics which can be ascribed to Prussian Blue's unique cage-like structure which can facilitate rapid ion transport. On the other hand, PB-1 suffers from capacity loss at higher current densities.

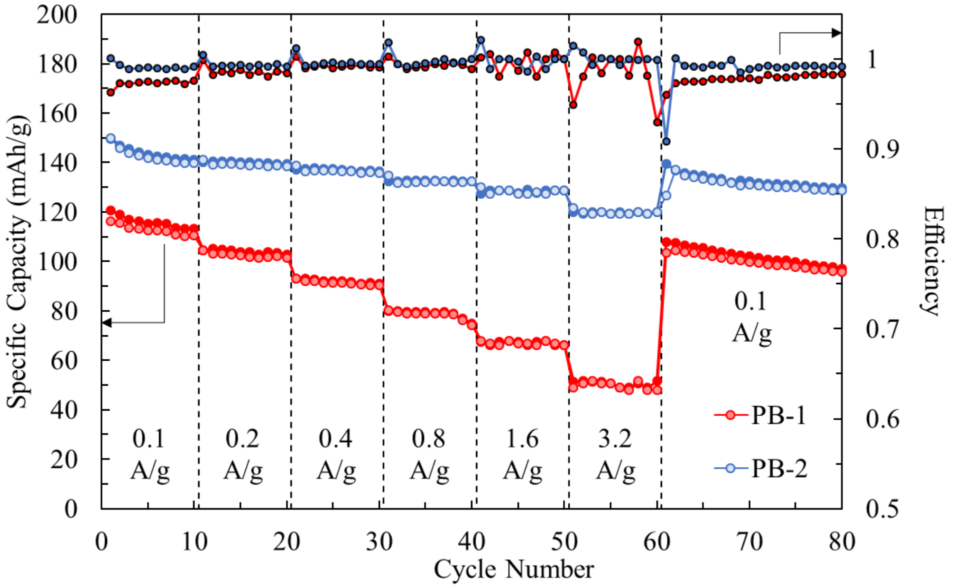

Figure 4-13. Discharge capacity at various current rates.

Kinetics were further explored with electrochemical impedance spectroscopy (EIS) on batteries in the charged state after galvanostatic cycling. Nyquist plots (**Figure 4-14a**) show a high frequency semi-circle representing charge transfer resistance and a low-frequency tail indicating Warburg diffusion. PB-1 shows a larger semi-circle compared PB-2 indicating that its charge transfer resistance is higher. The higher resistance is a contributing factor to the poor rate performance of PB-2. Additionally, the Warburg diffusion tails can be analyzed to estimate the nominal sodium diffusion coefficient of the FeHCF electrode by the following:

$$\sigma = \frac{RT}{n^2F^2A\sqrt{2}}\left(\frac{1}{C_{Na}D_{Na}^{1/2}}\right) \qquad (4\text{-}1)$$

The Warburg coefficient, σ, is the slope of real impedance versus the inverse square root of frequency in the low frequency region (**Figure 4-14b**). R is the gas constant, T is temperature, n is the number of electrons transferred during intercalation, F is the Faraday constant, A is surface area which is estimated in this case as the electrode surface area, C_{Na} is the molar concentration of sodium ions which is set to 0.001 mol/cm^3, and D_{Na} is the nominal diffusion coefficient of sodium ions. Solving for D_{Na} results in values of 2×10^{-12} and 7×10^{-12} cm^2/s respectively for PB-1 and PB-2. The more crystalline FeHCF particles of PB-2 with low vacancies demonstrate faster ion diffusion than nanoparticles with high vacancy concentration. Vacancies and high energy surface defects may act as traps for sodium ions. Another possibility is that the water content of PB-2 after thermal preparation is higher than PB-1 due to its higher dehydration temperature according to TGA. Water can help shield the coulombic interaction between the crystal host and intercalated ions, allowing for faster diffusion.

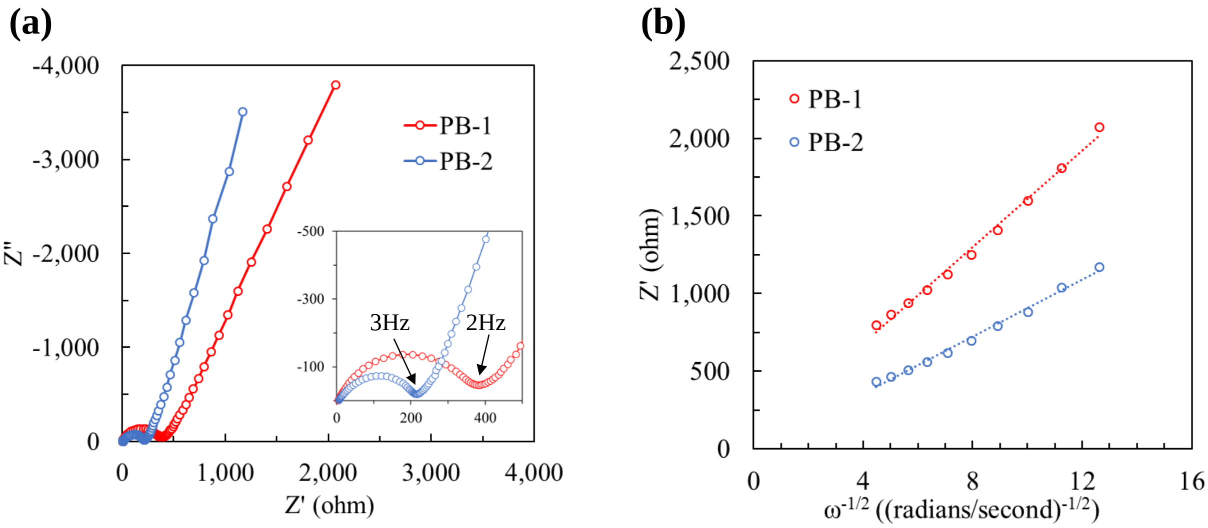

Figure 4-14. EIS spectra (a) and plot of real impedance vs inverse square root of angular frequency (b) for FeHCF batteries after cycling.

Reproduced in part with permission from Royal Society of Chemistry Copyright 2020.
Neale, Z. G.; Liu, C.; Cao, G. Effect of synthesis pH and EDTA on iron hexacyanoferrate for sodium-ion batteries.
Sustainable Energy & Fuels 2020, 4 (6), 2884–2891. https://doi.org/10.1039/d0se00120a.

4.4 Conclusions

FeHCF cubic crystals were synthesized with and without EDTA at constant pH and its effect on sodium-ion battery performance was observed. XRD and SEM characterization showed that particle size and crystallinity increased with the addition of EDTA. TGA and CHN analysis confirmed that PB-2 had a lower water content and higher carbon content, indicating fewer $[\mathrm{Fe(CN)_6}]$ anions. The lower ratio of LS-Fe to HS-Fe measured by Mössbauer spectroscopy corroborates with this claim. Battery performance greatly increased for PB-2 with higher capacity, better coulombic efficiency, and faster rate performance than PB-1 due to more redox active low-spin Fe capacity contribution, faster diffusion, and lower charge transfer resistance.

This work demonstrates that the EDTA molecule can be used as an effective additive for the synthesis of iron hexacyanoferrate at room temperature. By controlling nucleation rate, particle size and vacancy concentrations can be controlled. This has positively affected the capacity and rate performance of FeHCF in sodium-ion batteries. To the best of the author's knowledge, this research has demonstrated the highest capacity recorded for a FeHCF electrode grown at room temperature, and it is competitive with many made through high-temperature decomposition synthesis that generates toxic cyanide byproduct.

Reproduced in part with permission from Royal Society of Chemistry Copyright 2020.
Neale, Z. G.; Liu, C.; Cao, G. Effect of synthesis pH and EDTA on iron hexacyanoferrate for sodium-ion batteries. Sustainable Energy & Fuels 2020, 4 (6), 2884–2891. https://doi.org/10.1039/d0se00120a.

Table 4-3. Literature comparisons of FeHCF for non-aqueous sodium-ion batteries.

Synthesis Method	**Formula**	**Electrolyte**	**First Discharge (mAh/g)**	**Retention**	**Rate (mAh/g)**	**Source**
Precipitation Room temp. EDTA pH 3.8	$Na_{0.71}Fe[Fe(CN)_6]_{0.82}\cdot 2.68H_2O$	$NaClO_4$ PC 5%FEC	151 (100mA/g)	82% (100 cycles @100 mA/g)	122 (3.2 A/g)	This work
One-pot reflux 140^{o}C	$Na_2Fe[Fe(CN)_6]$ * 2 H_2O	$NaClO_4$ EC/PC	150 (85 mA/g)	77% (10 cycles @ 85 mA/g)	-	71
One-pot Air HCl 60^{o}C	$Na_{0.61}Fe[Fe(CN)_6]_{0.94}$ 15.7% H_2O	$NaPF_6$ EC/DEC	170 (25 mA/g)	107% (150 cycles @ 25 mA/g)	70 (0.6 A/g)	74
Precipitation Room temp. citrate	$Na_{1.92}Fe[Fe(CN)_6]$ * 13.2% H_2O	$NaClO_4$ EC/PC	129 (200 mA/g)	70% (100 cycles @ 200 mA/g)	71 (1.2 A/g)	75
One-pot Hydrothermal 140^{o}C	$Na_{1.92}Fe[Fe(CN)_6]$ * 0.08 H_2O	$NaPF_6$ EC/DEC 5% FEC	~150 (75 mA/g)	~89% (100 cycles @300 mA/g)	145 (1.5 A/g)	111
Precipitation 60^{o}C	$Fe[Fe(CN)_6]$	$NaPF_6$ EC/DEC	109 (60 mA/g)	96% (150 cycles @60 mA/g)	98 (1.2 A/g)	114
One-Pot Air HCl 65^{o}C	$Na_{0.52}Fe[Fe(CN)_6]_{0.85}$ * 3.15 H_2O @C	$NaPF_6$ EC/DEC	~130 (50 mA/g)	90% (2k cycles @ 2 A/g)	77.5 (45 A/g)	115

Reproduced in part with permission from Royal Society of Chemistry Copyright 2020.
Neale, Z. G.; Liu, C.; Cao, G. Effect of synthesis pH and EDTA on iron hexacyanoferrate for sodium-ion batteries. Sustainable Energy & Fuels 2020, 4 (6), 2884–2891. https://doi.org/10.1039/d0se00120a.

Chapter 5: Chemical control of vacancy concentration in iron hexacyanoferrate

Iron hexacyanoferrate (FeHCF) particles were synthesized at room temperature with ethylenediaminetetraacetic acid (EDTA) at varying pH. The presence of EDTA produced faceted particles and increasing synthesis pH resulted in slower reaction kinetics and larger particles with lower water content and fewer anion vacancies determined by TGA and Mössbauer spectroscopy. Electrochemical testing of sodium metal half cells revealed higher capacity in FeHCF particles grown at lower pH with EDTA, obtaining a maximum discharge capacity of 151 mAh/g with 79% capacity retention after 100 cycles at 100 mA/g and a rate capability of 122 mAh/g at 3.2 A/g. In contrast, particles grown at higher pH had stunted low-spin Fe redox activity but with improved long-term cyclic stability. These findings demonstrate that small changes in synthesis pH can greatly affect the growth and electrochemical properties of FeHCF when using a pH sensitive chelating agent such as EDTA.

5.1 Introduction

The chelation strength of EDTA depends on solution pH. The EDTA molecule can change from a bidendate to hexadendate chelator by deprotonation of its carboxylic acid groups. It is hypothesized that increasing the synthesis pH of FeHCF precipitation with EDTA additive will decrease nucleation and increase crystal growth, thus improving battery performance. FeHCF with less anion vacancies would be less prone to crystal instability during oxidation, thus increase cyclic stability of intercalation. The decrease in nucleation rate was measured by time-dependent light absorbance during precipitation. Preliminary trials have demonstrated complete inhibition of FeHCF precipitation without pH control of solution due to the basicity of the $Na_4Fe(CN)_6$ and Na-EDTA precursor salts (pH > 6). Additionally, if pH is too low the EDTA molecule becomes insoluble and does not participate in chelation. A pH range between 3.8 and 4.4 was deemed suitable for experimentation.

5.2 Experimental Procedures

Synthesis of FeHCF with EDTA at different pH

Four 0.3M acetate buffer solutions were made at pH 3.8, 4.0, 4.2, and 4.4 with sodium acetate and acetic acid. Samples were made at each pH from a 200 mL solution of 20 mM $\mathrm{Na_4Fe(CN)_6} * 10\mathrm{H_2O}$ and a 200 mL solution of 30 mM $\mathrm{FeCl_2} * 4\mathrm{H_2O}$ and 30 mM ethylenediaminetetraacetic acid tetrasodium salt. The $FeCl_2$ solution was quickly added to the former solution and stirred for 24 hours at room temperature before particles were collected and washed with water and ethanol through centrifugation. The blue product was dried in air at 80^{o}C overnight. Herein samples will be labeled as PB(3.8), PB(4.0), PB(4.2) and PB(4.4) corresponding to their respective solution pH during synthesis.

Physical Characterization

The crystal structures of the as-synthesized products were determined via powder X-ray diffraction (XRD) on a Bruker D8 Discover using a Cu-K X-ray source with nickel filter and 1-dimensional X-ray transducer. A JSM 7000F scanning electron microscope was used in SEI mode to collect electron micrographs. SEM samples were prepared by drop casting FeHCF-water suspensions onto silicon substrates and drying at 80^{o}C under vacuum. The optical absorbance at 700 nm was measured for PB(3.8) and PB(4.4) using a UV-vis spectrometer at 10 second intervals for the first 30 minutes after mixing precursor solutions together. Thermal gravimetric analysis

(TGA) was performed on samples under nitrogen gas at 5°C/min. Exhaust gas from TGA was filtered through a 0.1M ferrous sulfate water trap to capture any cyanide gas generated. Total carbon, hydrogen, and nitrogen content was determined using a Perkin Elmer CHN 2400 series analyzer. Mössbauer spectroscopy was performed on FeHCF powders using a ^{57}Co radioactive source. X-ray emission spectroscopy (XES) was performed on a lab-built high-resolution spectrometer from the Seidler X-ray Spectroscopy Lab at the University of Washington.

Electrochemical Characterization

Electrodes were made on aluminum foil by doctor blading a slurry of 70% active material, 20% Super P conductive carbon, and 10% sodium carboxymethylcellulose (CMC) binder dissolved in water. 2032 type coin cells were made in an Argon glovebox with a sodium metal anode and Whatman glass fiber separator saturated with 1M $NaClO_4$ in propylene carbonate (PC) with 5 vol% fluoroethylene carbonate (FEC) electrolyte solution. Batteries for cyclic voltammetry did not include FEC additive in their electrolyte. Galvanostatic cycling was done on a LAND battery tester between 2 and 4.3V. Cyclic voltammetry was performed with an Arbin electrochemical tester between 2 and 4.3V at 0.1mV/s.

5.3 Results and Discussion

Crystallinity and particle size

The XRD patterns of the four FeHCF samples synthesized under different pH match the cubic $Fm\bar{3}m$ crystal structure of Prussian blue (**Figure 5-1a**). Sharp diffraction peaks with small FWHM suggests large crystallite size with good crystallinity. The diffraction peak intensity increases slightly with synthesis pH. Improved diffraction intensity corresponds to crystallinity, indicating better crystalline particles grown at higher pH. Additionally, peak position of the (200) diffraction peak decreases with increasing pH, corresponding to an approximate lattice increase from 10.24

Reproduced in part with permission from Royal Society of Chemistry Copyright 2020.
Neale, Z. G.; Liu, C.; Cao, G. Effect of synthesis pH and EDTA on iron hexacyanoferrate for sodium-ion batteries. Sustainable Energy & Fuels 2020, 4 (6), 2884–2891. https://doi.org/10.1039/d0se00120a.

to 10.27 Å between pH 3.8 and pH 4.4 (**Figure 5-1b**). An increasing lattice could correspond to higher concentration of Na^+ inside the crystal.

The trends in XRD intensity are confirmed by SEM micrographs (**Figure 5-2**) showing that particles display faceted morphology, and particle size increases from ~100 nm at pH 3.8 to micrometer size at pH 4.4. Particle geometry is not necessarily cubic and consists of irregular particles with square and rectangular facets. The thermodynamic equilibrium shape of FeHCF is cubic because of its face-center-cubic lattice. The synthesized FeHCF particles with EDTA do display faceted features, which might suggest that the crystal was grown under thermodynamic conditions; however, the non-uniformity and irregularity of particle geometry could be due to non-classical crystallization, such as mesocrystal assembly. Mesocrystals are hierarchical structures formed by the oriented self-assembly and fusing of smaller nanoparticles.[116–118] There are several reports on the formation of FeHCF mesocrystals of various morphologies through hydrothermal synthesis with different organic additives such as glucose, polyethylene glycol, or polyvinylpyrrolidone.[119–121] The addition of EDTA could assist in oriented aggregation of FeHCF nanocrystals as it has been shown in the formation of biomineral mesocrystal materials.[122,123] The difference in mesocrystal size between PB(3.8) and PB(4.4) may be due to a difference in the initial nanocrystal size as illustrated in **Figure 5-3**.

Crystal size is dependent on the competition between growth rate and nucleation rate, where the energy barrier for nucleation is related to particle solubility and free ion concentration.[124] The solubility product of Prussian blue has been reported as between 10^{-264} and 10^{-177}, resulting in extremely fast nucleation.[101] The presence of EDTA reduces the activity of free Fe in solution by forming a complex with Fe ions, slowing the kinetics of nucleation which typically dominate over particle growth. Formation of crystal nuclei with $[Fe(CN)_6]^{4-}$ anions is more inhibited by EDTA at higher pH, resulting in increased crystal size. Acetate anions from the acetate buffer solution can also form a complex with Fe ions in solution; however, it is a monodentate ligand and has a lower stability constant of $10^{3.2}$ (K_1) compared to $10^{14.3}$ for EDTA.[125] In comparison, FeHCF grown by the same procedure without EDTA results in nanoparticles that do not show any significant difference in particle size between different pH (**Figure 4-2**).

Growth rate and sodium concentration

UV-visible light spectroscopy of FeHCF particles dispersed in water show an absorbance peak associated with Prussian blue (**Figure 5-4a**) at 700 nm. Visible light absorption is due to charge transfer between low-spin Fe^{2+} and high-spin Fe^{3+} ions in Prussian blue.[108] Increasing synthesis pH results in decreasing absorbance at 700 nm but increasing absorbance near 400 nm. The lower absorbance at 700 nm could be caused by an increased concentration of reduced high-spin Fe^{2+} in the larger FeHCF particles. The reduced state of FeHCF, known as Prussian white, is not stable in air and will gradually oxidize to Prussian blue. PB(4.4) may be less prone to oxidation due to its larger particle size, or perhaps because free Fe^{3+} ions in solution are preferentially chelated by EDTA compared to Fe^{2+}.[105] The higher concentration of Fe^{2+} could be balanced by an increased concentration of Na^+ in the FeHCF crystal to maintain charge neutrality. Energy dispersive X-ray spectroscopy (EDS) reveals Na:Fe ratios of 0.39, 0.42, 0.43, and 0.51 for PB(3.8), PB(4.0), PB(4.2), and PB(4.4), respectively. The increasing concentration of Na^+ with synthesis pH for FeHCF samples could directly correspond with the ratio of Fe^{2+} to Fe^{3+} and corroborates the decreasing peak intensity of UV-vis.

The claim that EDTA retards the nucleation of FeHCF particles more at higher pH was tested by measuring optical absorbance at 700 nm during the first 30 minutes of synthesis for PB(3.8) and PB(4.4) (**Figure 5-4b**). The solution synthesized at pH 3.8 reaches saturated optical absorbance within the first few minutes of reaction. In contrast, the sample synthesized at pH 4.4 increases optical absorbance more gradually with time, indicating slower precipitation of particles.

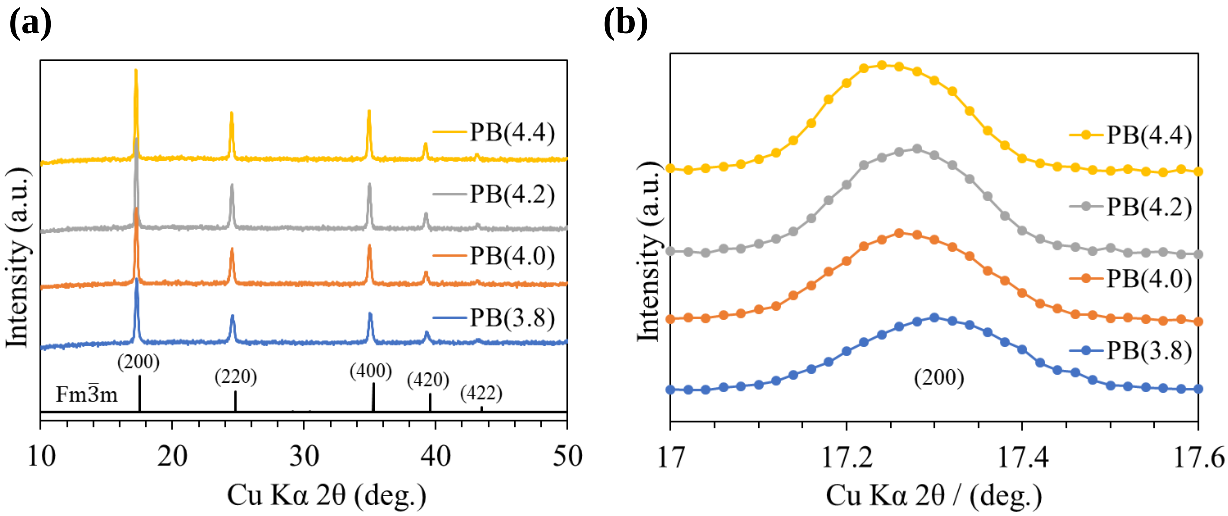

Figure 5-1. XRD patterns of FeHCF samples between (a) 10-50 degrees compared against ICDD No. 00-052-1907 for Prussian blue and (b) zoomed pattern on the (200) peak.

Neale, Z. G.; Liu, C.; Cao, G. Effect of synthesis pH and EDTA on iron hexacyanoferrate for sodium-ion batteries.
Sustainable Energy & Fuels 2020, 4 (6), 2884–2891. https://doi.org/10.1039/d0se00120a.

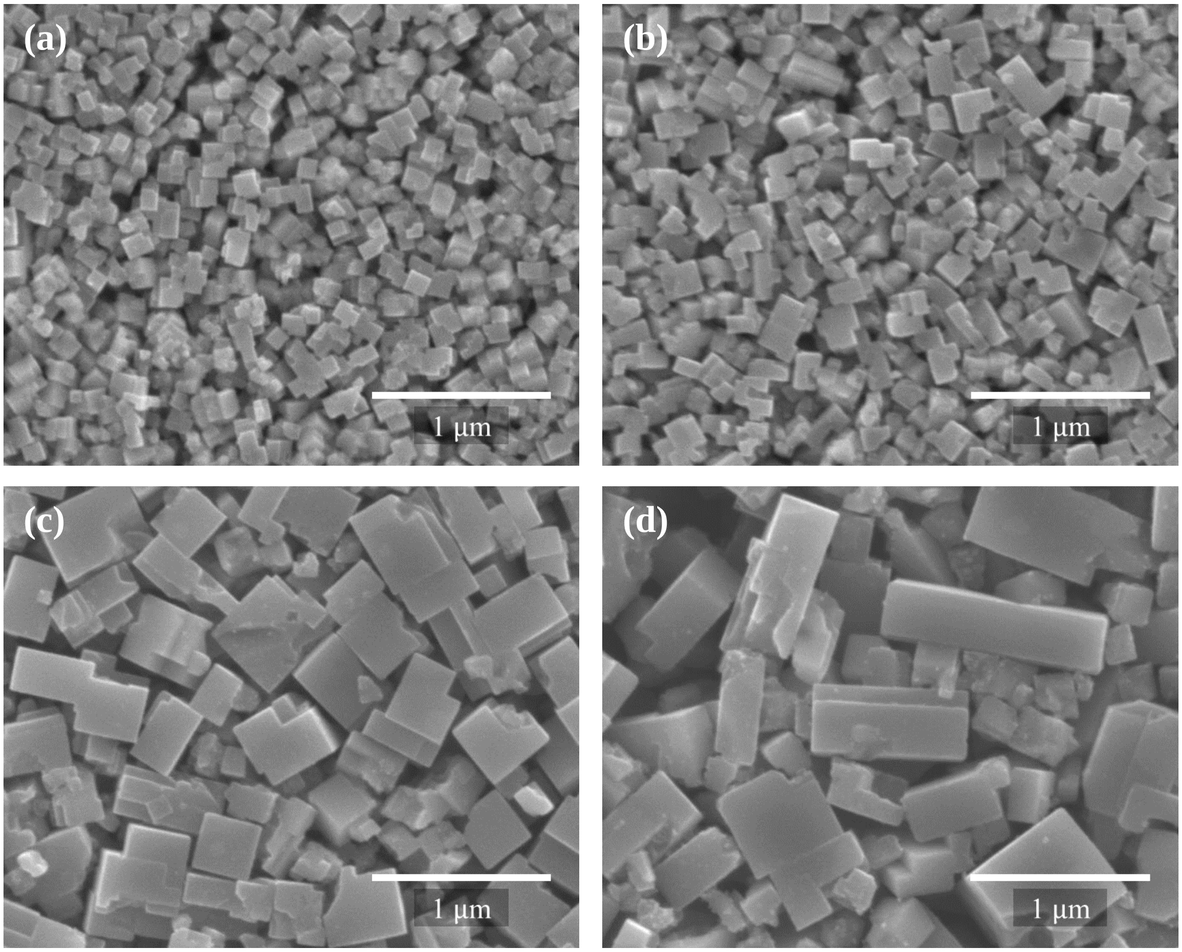

Figure 5-2. SEM micrographs of (a) PB(3.8), (b) PB(4.0), (c) PB(4.2), and (d) PB(4.4).

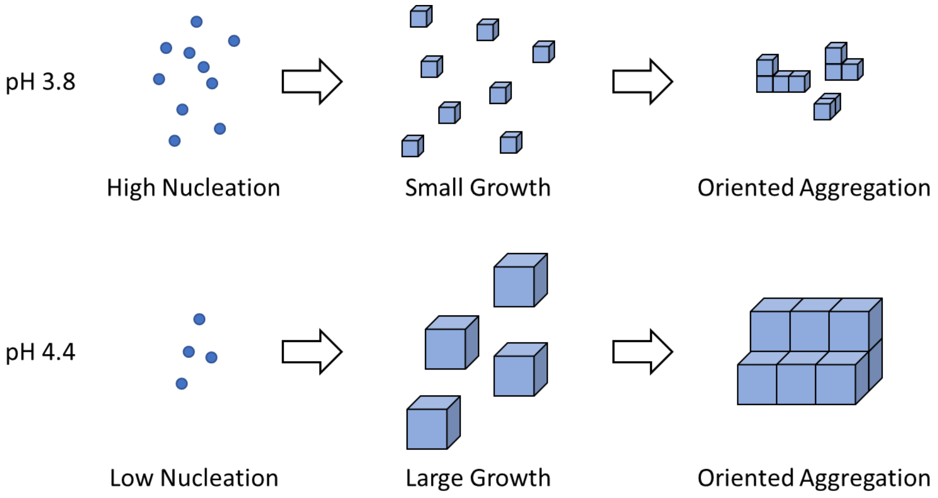

Figure 5-3. Proposed mechanism of oriented aggregation between different synthesis pH.

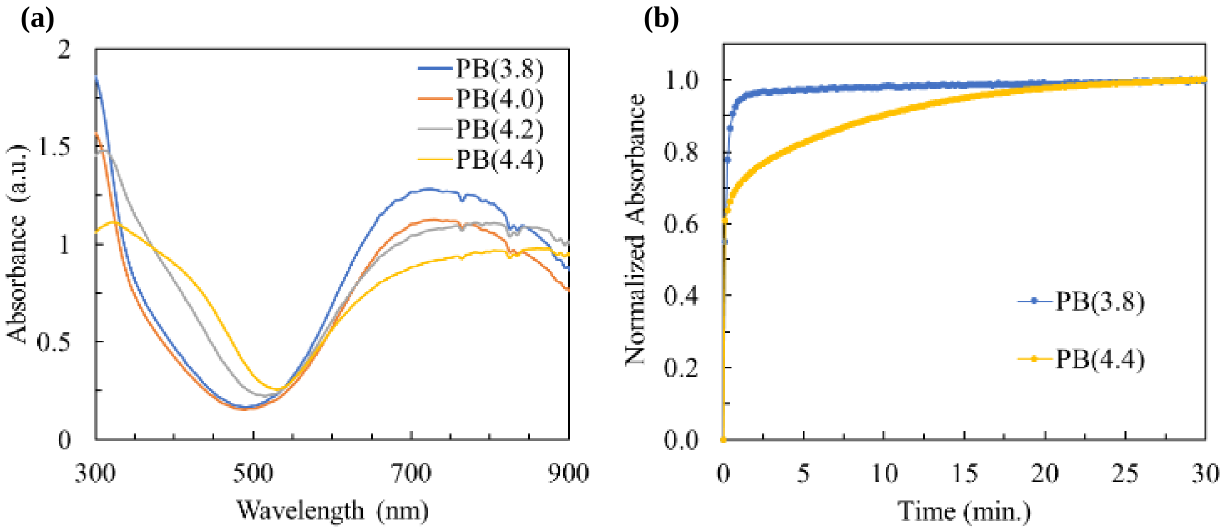

Figure 5-4. UV-visible light absorbance spectra for FeHCF samples (a). Normalized optical absorbance at 700nm during the first 30 minutes of synthesis (b).

Water concentration

The crystal structure of FeHCF is typically associated with zeolitic water and water coordinated to high-spin Fe in place of $Fe(CN)_6$ anion vacancies. TGA results (**Figure 5-5**) show two weight loss regions that corresponding to dehydration and partial decomposition of cyanide groups.[106] The initial weight loss step associated with total dehydration reveals water content of 16.4, 14.4, 13.8, and 13.4 wt% for PB(3.8), PB(4.0), PB(4.2), and PB(4.4), respectively. The increasing water content at lower synthesis pH could be attributed to additional water present in $Fe(CN)_6$ anion vacancy sites and from increased surface absorbed water due to smaller particle size. Additionally, Fe ions in solution are coordinated by water during a typical synthesis which could lead to a high water content of FeHCF during rapid precipitation. When EDTA is added it blocks coordinated water by chelating with Fe ions. At higher pH the chelation strength of EDTA is stronger and more water may be blocked from coordinating with Fe. Furthermore, the dehydration and decomposition temperature increase with particle size which could be due to a

Reproduced in part with permission from Royal Society of Chemistry Copyright 2020.
Neale, Z. G.; Liu, C.; Cao, G. Effect of synthesis pH and EDTA on iron hexacyanoferrate for sodium-ion batteries. Sustainable Energy & Fuels 2020, 4 (6), 2884–2891. https://doi.org/10.1039/d0se00120a.

thermal delay dependent on particle size, a similar phenomenon to a shift in onset temperature when heating rate is increased.

CHN elemental analysis results (**Table 5-1**) for total hydrogen corroborate the correlation with synthesis pH. Assuming that all hydrogen corresponds to water in the sample, CHN analysis returns 16.7, 12.8, 12.1, and 11.1 wt% H_2O respectively for PB(3.8), PB(4.0), PB(4.2), and PB(4.4).

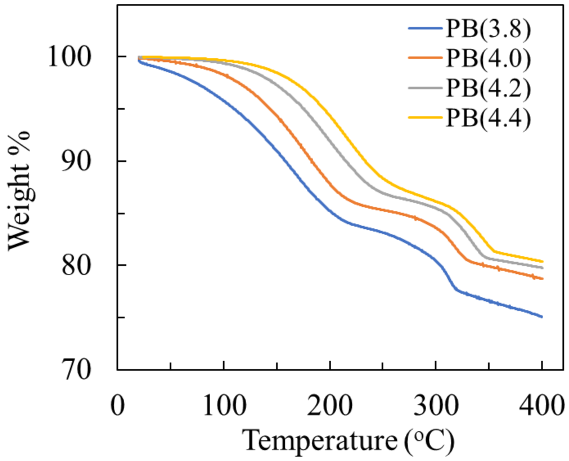

Figure 5-5. TGA of as-synthesized FeHCF powders under nitrogen at 5°C/min.

Table 5-1. Elemental analysis results for carbon, hydrogen, and nitrogen, and calculated H_2O.

Sample	Weight %			
	C	H	N	H_2O
PB(3.8)	21.1	1.9	24.2	16.7
PB(4.0)	21.2	1.4	24.2	12.8
PB(4.2)	21.4	1.4	24.7	12.1
PB(4.4)	21.6	1.2	24.8	11.1

Vacancy concentration

Mössbauer spectroscopy was performed on PB(3.8) and PB(4.4) to investigate the effect synthesis pH had on $Fe(CN)_6$ vacancies. The nuclear resonance of ^{57}Fe atoms in FeHCF are sensitive to their local chemical environment and valence state. The Mössbauer spectra of PB(3.8) and PB(4.4) (**Figure 5-6**) can be fitted with Lorentzian curves representing each iron species and the area of the curve is proportional to the molar fraction of that species. Using the same fitting methodology as Grandjean et al., a single doublet was assigned to low-spin Fe^{2+}, and three doublets were assigned to high-spin Fe^{3+} and Fe^{2+} with their line widths, Γ, held equal to that of the α-Fe calibration of 0.34 mm/s.[107] This is because the presence of low-spin $Fe(CN)_6$ vacancies create several chemically unique identities of high-spin Fe. For PB(4.4) it was necessary to add an additional set of doublets corresponding to high-spin Fe^{2+} to fit a shoulder peak, which corroborates the increased Na:Fe ratio from EDS and decreased absorption peak at 700 nm observed in **Figure 5-4** indicating increased high-spin Fe^{2+} concentration. The fitting parameters of each curve are listed in **Table 5-2**.

The curve area ratios between low-spin and high-spin iron species reveal approximately 18 and 4% $Fe(CN)_6$ anion vacancies for PB(3.8) and PB(4.4), respectively, corresponding to estimated chemical formulae of $Na_{0.71}Fe[Fe(CN)_6]_{0.82}\cdot 2.68H_2O$ and $Na_{1.00}Fe[Fe(CN)_6]_{0.96}\cdot 2.38H_2O$ when incorporating EDS and TGA results. This result is supported by the decrease in weighted quadrupole splitting, $\langle \Delta E_Q \rangle$, of high-spin Fe^{3+} from 0.14 to 0.11 mm/s. Quadrupole splitting of the iron nucleus is caused by an electric field gradient contributed to by nonsymmetric valence electrons or ligands.[126] The smaller quadrupole splitting of PB(4.4) suggests its high-spin Fe^{3+} centers are surrounded by a more symmetric octahedra of $Fe(CN)_6$ anions due to fewer vacancies.

Similarly, the isomer shift, δ, of high-spin Fe^{3+} increases from 0.41 to 0.42 mm/s for PB(3.8) and PB(4.4), respectively. The isomer shift is sensitive to *s*-electron density, with more negative shift for increasing *s*-electron density at the nucleus of Fe atoms.[110] High-spin Fe^{3+} in FeHCF are octahedrally coordinated to the electronegative nitrogen of $Fe(CN)_6$, pulling electrons away from its center. When $Fe(CN)_6$ ligands are vacant the *s*-electron density at the nucleus of high-spin Fe increases resulting in a less positive isomer shift as seen in PB(3.8). The decreasing vacancy concentration of FeHCF grown with EDTA at higher pH indicated by Mössbauer spectroscopy may be attributed to the slower nucleation and growth rate of particles.

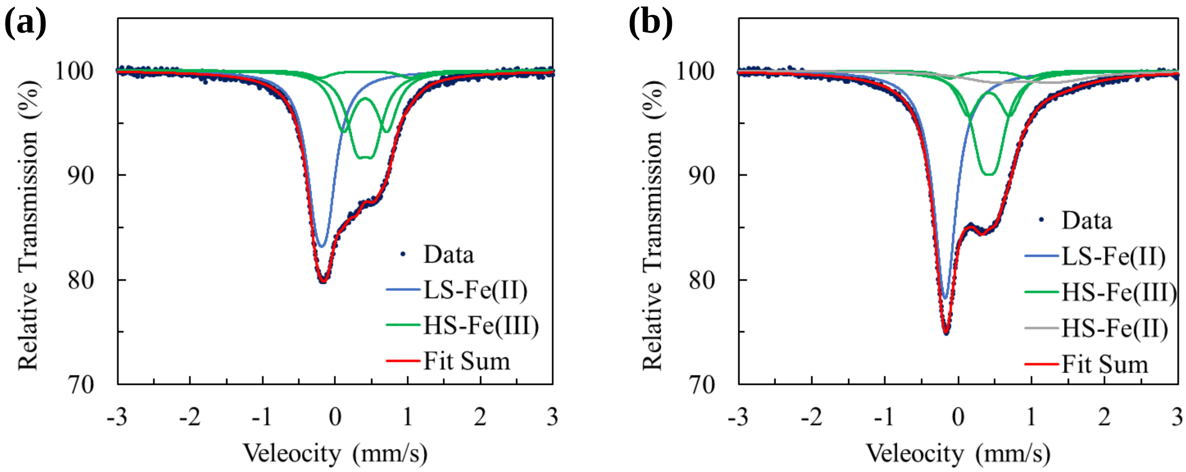

Figure 5-6. Mössbauer spectra at room temperature of (a) PB(3.8) and (b) PB(4.4) with fitted Lorentzian curves representing iron species.

Table 5-2. Fitting parameters for Mössbauer spectra. $\boldsymbol{\delta}$ is the isomer shift relative to $\boldsymbol{\alpha}$-Fe in mm/s, $\boldsymbol{\Delta E_Q}$ is the quadrupole splitting in mm/s, and $\boldsymbol{\Gamma}$ is the full line width at half max in mm/s. The quadrupole splitting displayed for high-spin Fe(III) is the weighted average of the three doublets.

	Low-Spin Fe(II)				**High-Spin Fe(III)**				**High-Spin Fe(II)**				**Ratio**
	δ	ΔE_Q	Γ	Area %	δ	$\langle \Delta E_Q \rangle$	Γ (fixed)	Area %	δ	$\langle \Delta E_Q \rangle$	Γ (fixed)	Area %	LS : HS
PB(3.8)	-0.19	0.14	0.34	45	0.41	0.14	0.34	55	-	-	-	0	0.82 : 1
PB(4.4)	-0.18	0.00	0.37	49	0.42	0.11	0.34	43	1.06	0.18	0.34	9	0.96 : 1

Further examination of the iron species concentration between PB(3.8) and PB(4.4) was performed with XES (**Figure 5-7**). FeO and Fe_2O_3 were used as standards for high-spin Fe(II) and Fe(III) in octahedral coordination, and $Na_4Fe(CN)_6$ and $K_3Fe(CN)_6$ were used as standards for low-spin Fe(II) and Fe(III) in octahedral coordination. The XES spectra of PB(3.8) and PB(4.4) were fit by a linear combination of the standard spectra in order to estimate the relative concentration of each iron species. The relative amount of low-spin iron was calculated to be 43

Reproduced in part with permission from Royal Society of Chemistry Copyright 2020.
Neale, Z. G.; Liu, C.; Cao, G. Effect of synthesis pH and EDTA on iron hexacyanoferrate for sodium-ion batteries. Sustainable Energy & Fuels 2020, 4 (6), 2884–2891. https://doi.org/10.1039/d0se00120a.

and 49% in PB(3.8) and PB(4.4), respectively (**Figure 5-8)**. However, the error associated with the line fitting was very large, especially for high-spin iron species. The reason for such a large error is due to the chemical dissimilarities between the standard oxides of high-spin iron and the nitrogen-coordinated high-spin iron in FeHCF. Additionally, the high-spin iron of FeHCF may not necessarily be octahedrally coordinated due to $[\mathrm{Fe(CN)_6}]$ vacancies. Nevertheless, the general trend in XES results supports the lower vacancy formation determined by Mössbauer spectroscopy.

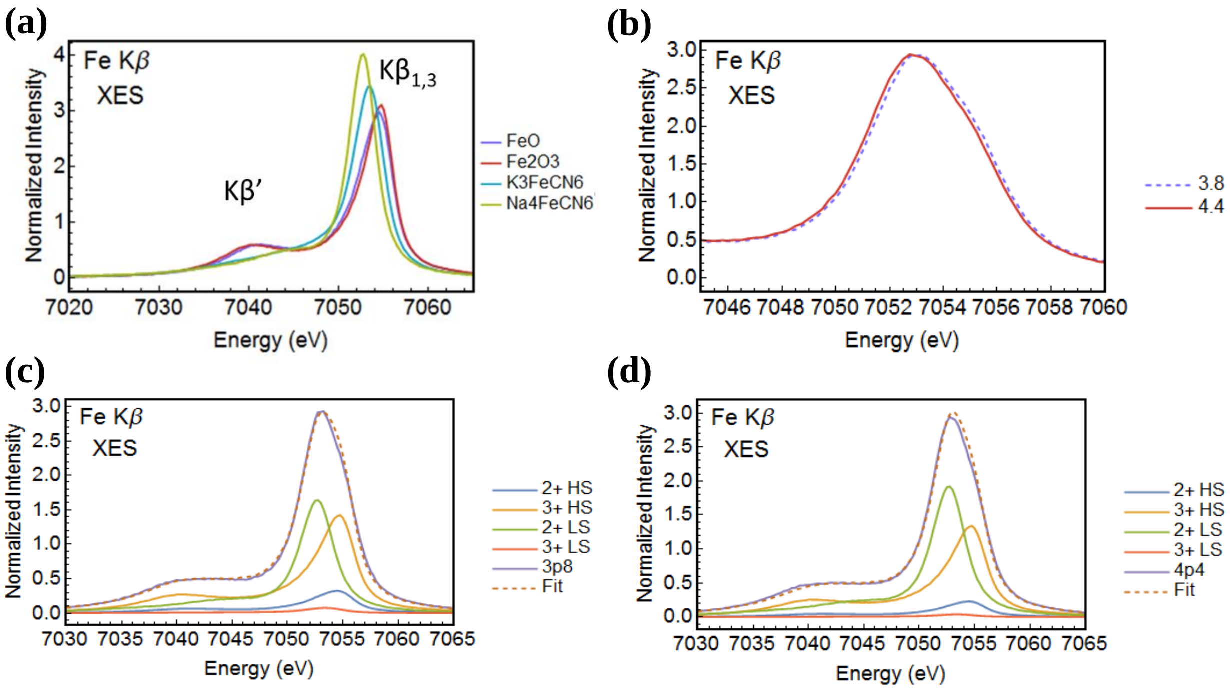

Figure 5-7. XES spectra of (a) Fe standards, (b) zoomed spectra of PB(3.8) and PB(4.4), (c) fitted spectra of PB(3.8), and (d) fitted spectra of PB(4.4).

Reproduced in part with permission from Royal Society of Chemistry Copyright 2020.
Neale, Z. G.; Liu, C.; Cao, G. Effect of synthesis pH and EDTA on iron hexacyanoferrate for sodium-ion batteries. Sustainable Energy & Fuels 2020, 4 (6), 2884–2891. https://doi.org/10.1039/d0se00120a.

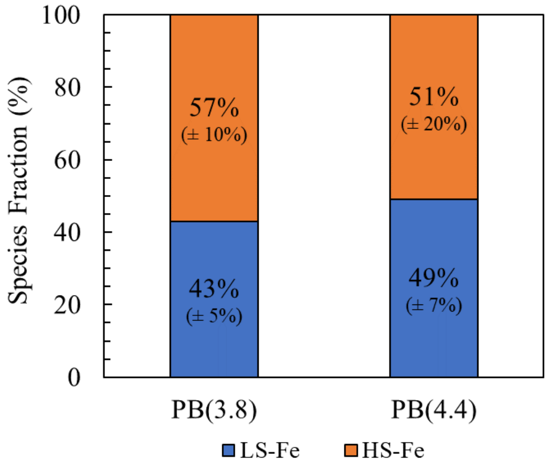

Figure 5-8. Species fraction between low-spin Fe and high-spin Fe in PB(3.8) and PB(4.4) determined by XES.

Effect on redox potential

Cyclic voltammetry (CV) of sodium metal half-cells reveals several redox peaks corresponding to sodium ion intercalation and deintercalation (**Figure 5-9**). The redox potential of sodium-ion intercalation into FeHCF can be affected by ligand field energy of the transition metal ion and energy of the intercalation site which could be influenced by the concentration of sodium and water in the crystal.[112] Previous studies have modeled the different energies associated with ion intercalation into different sites, as well as the influence of water molecules. Possible sodium sites include 8c (body-centered), 24d (face-centered), 32f (displaced 8c towards high-spin Fe), 32f' (displaced 8c towards low-spin Fe), and 48g (displaced between 8c and 24d).[112] Additionally, the presence of water has been reported to affect the redox potential of sodium ion intercalation in the large interstitial sites of FeHCF.[127,128]

Cyclic voltammetry during the initial charge cycle shows a large current response at high-voltage which may be the oxidation of water in the crystal. The oxidation peak is larger in PB(3.8) than PB(4.4) which could be because of the larger water content of PB(3.8). The first reduction peak located above 3.5 V may be the intercalation of Na-ions into hydrated sites and low-spin Fe reduction.[71] This peak's redox potential is higher for PB(3.8) than PB(4.4) which could be due to the amount of water, which has been modeled to influence the redox potential of FeHCF and decrease in potential with lowering water content.[127] After subsequent cycling the first reduction peak above 3.5 V decreases in current density while the second reduction peak at around 3.3V increases, attributed to dehydrated Na-ion intercalation and low-spin Fe reduction. The reduction and oxidation peaks below this voltage are attributed to Na-ion intercalation and high-spin Fe reduction. The several peaks of high-spin Fe may also be due to the influence of water and intercalation site preference.

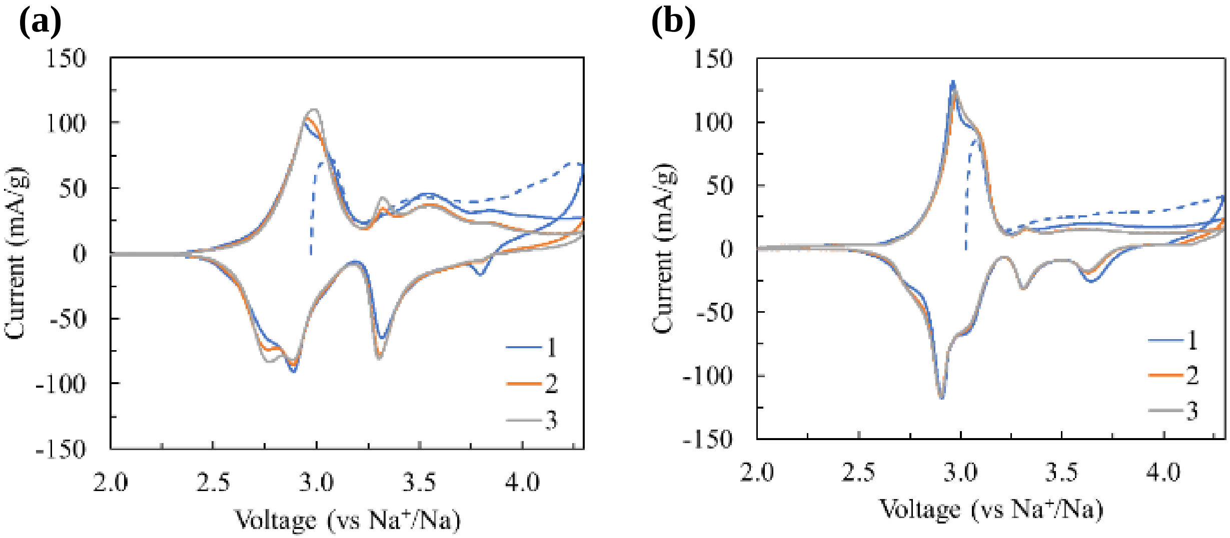

Figure 5-9. Cyclic voltammetry at 0.1 mV/s for PB(3.8) (a) and PB(4.4) (b). Dashed line is initial charge.

Reproduced in part with permission from Royal Society of Chemistry Copyright 2020.
Neale, Z. G.; Liu, C.; Cao, G. Effect of synthesis pH and EDTA on iron hexacyanoferrate for sodium-ion batteries. Sustainable Energy & Fuels 2020, 4 (6), 2884–2891. https://doi.org/10.1039/d0se00120a.

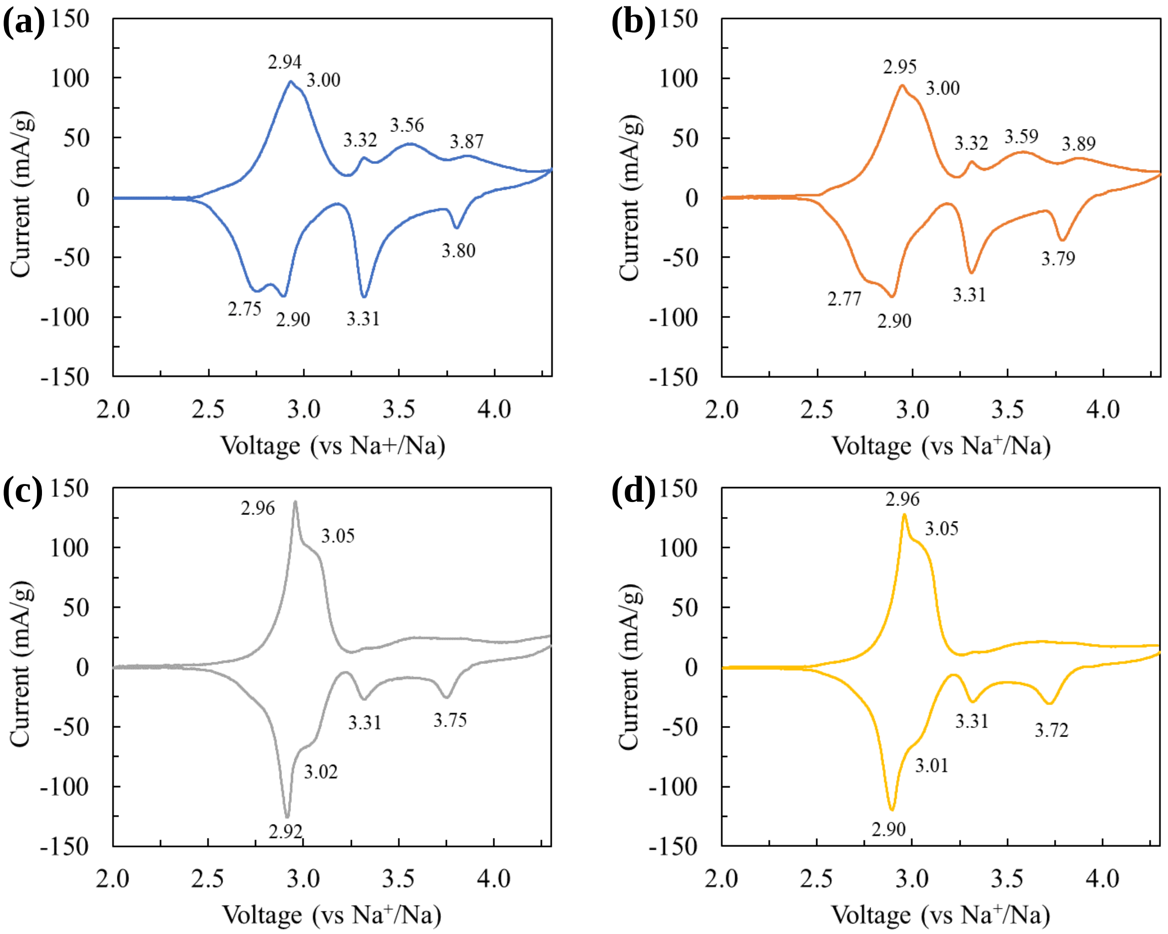

Figure 5-10. Cyclic voltammetry at 0.1 mV/s of FeHCF synthesized with EDTA at (a) pH 3.8, (b) pH 4.0, (c) pH 4.2, and (d) pH 4.4 (b).

Effect on capacity and cyclic stability

Galvanostatic cycling was performed on sodium metal half cells at 100 mA/g (**Figure 5-11**). During the initial charge cycle PB(4.4) shows a significantly larger plateau at 3.1 V than PB(3.8) indicating a greater concentration of initial high-spin Fe^{2+}. This corroborates the presence of a high-spin Fe^{2+} peak in the Mössbauer spectra and lower absorbance at 700 nm in UV-Vis of PB(4.4). On the other hand, the initial charge capacity contribution beyond this voltage plateau is larger for PB(3.8), indicating more redox active low-spin $[Fe(CN)_6]^{4-}$ despite having slightly more vacancies according to Mössbauer spectroscopy. The first cycle discharge capacities were 151, 142, 125, and 124 mAh/g for PB(3.8), PB(4.0), PB(4.2) and PB(4.4), respectively. The increased capacity of FeHCF synthesized at lower pH with EDTA is primarily due to a larger contribution of low-spin Fe redox activity (Figure S4). When the synthesis of FeHCF is carried out without EDTA, there is no significant difference in capacity or voltage between pH 3.8 and pH 4.4 (Figure S5), confirming that the difference is primarily influenced by the addition of EDTA and not the acetate buffer at different pH.

Capacity loss occurs after the first cycle and is more significant in samples synthesized at higher pH. Capacity loss could arise from irreversible ion insertion or extraction, structural collapse due to crystal distortion or dehydration, and irreversible side-reactions. Work by Rudola, et al. on high-quality micron-sized FeHCF crystals demonstrate electrochemical dehydration of the crystal when cycled to 4.3 V which may result in structural distortion and capacity loss.[71] PB(4.4) shows a larger initial capacity loss despite having slightly less water than PB(3.8). The larger particle size of PB(4.4) with fewer vacancies may be less accommodating to structural transformation resulting in larger initial capacity loss.

Upon further cycling all FeHCF samples suffer from capacity decay at different severity **(Figure 5-9**) with samples synthesized at higher pH demonstrating better cyclic performance. Capacity retention up to 100 cycles after the 3rd cycle was 82, 85, 94, and 91% and average coulombic efficiencies (discharge divided by charge) were 99.2, 99.5, 99.5, and 99.6% for PB(3.8), PB(4.0), PB(4.2), and PB(4.4), respectively. Long term cyclic instability in FeHCF can be caused by lattice collapse from $Fe(CN)_6$ vacancies and side-reactions from the oxidation of coordinated water,[129] thus the samples grown at higher pH with a more perfect crystal structure and less water has improved cyclability.

PB(3.8) particles were washed in pH 4.4 buffer solution and PB(4.4) particles washed in pH 3.8 buffer solution for 24 hours to test whether surface chemistry change due to pH had any effect on cyclability. The cyclic performance of the FeHCF particles did not change after washing in different pH solutions, and capacity retention remained nearly the same at 86 and 94% for PB(3.8) and PB(4.4), respectively (**Figure 5-13**).

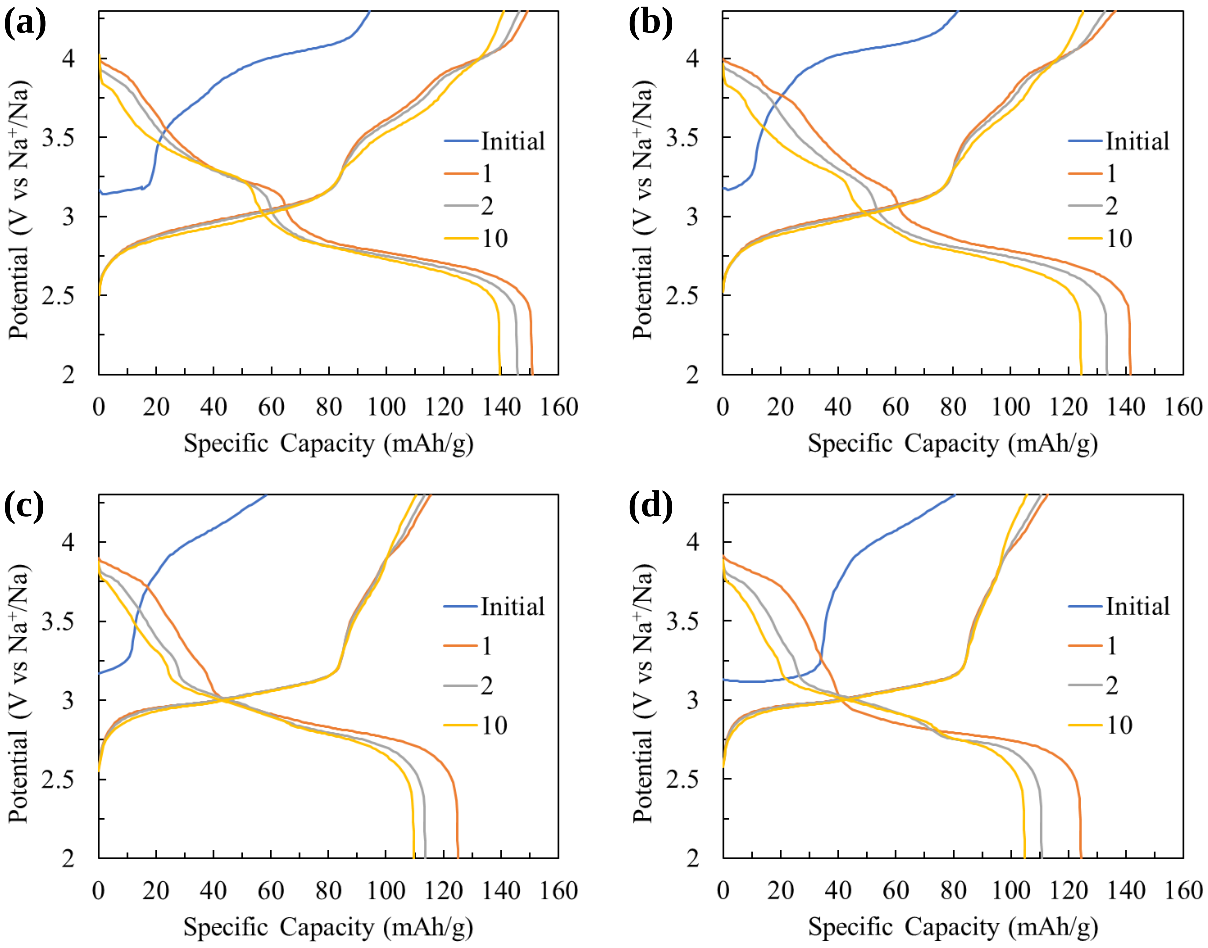

Figure 5-11. Galvanostatic profile at 100 mA/g of the initial charge and subsequent cycles for (a) PB(3.8), (b) PB(4.0), (c) PB(4.2), and (d) PB(4.4).

Reproduced in part with permission from Royal Society of Chemistry Copyright 2020.
Neale, Z. G.; Liu, C.; Cao, G. Effect of synthesis pH and EDTA on iron hexacyanoferrate for sodium-ion batteries. Sustainable Energy & Fuels 2020, 4 (6), 2884–2891. https://doi.org/10.1039/d0se00120a.

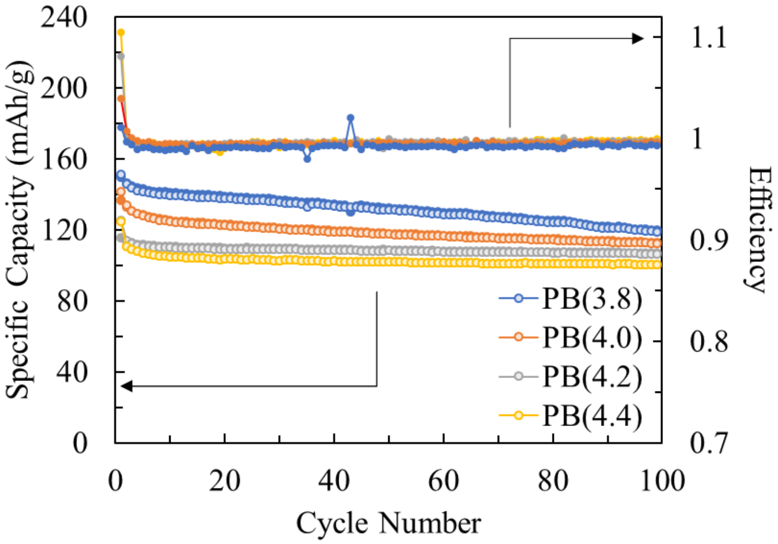

Figure 5-12. Galvanostatic cycling at 100 mA/g. Discharge shown as open circles and charge shown as filled circles.

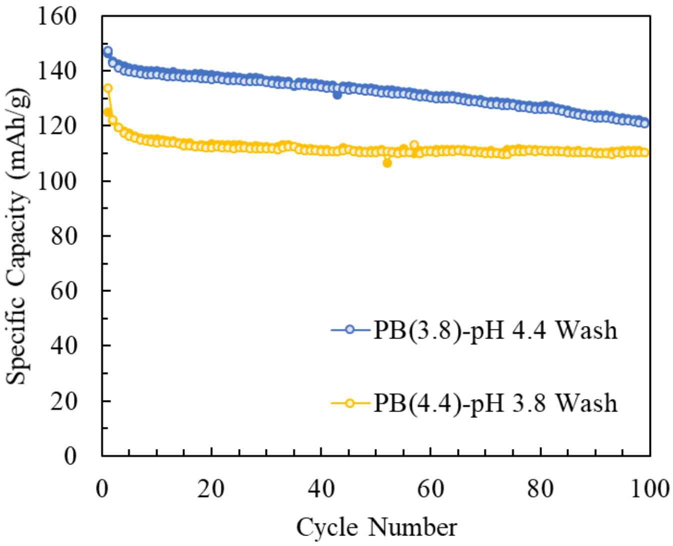

Figure 5-13. Galvanostatic cycling at 100 mA/g for PB(3.8) washed for 24 hours in pH 4.4 solution and PB(4.4) washed for 24 hours in pH 3.8 solution.

Intercalation Kinetics

The intercalation kinetics of FeHCF samples were investigated by cycling batteries at various current densities (**Figure 5-14**). The specific discharge capacities at a current density of 3.2 A/g

Reproduced in part with permission from Royal Society of Chemistry Copyright 2020.
Neale, Z. G.; Liu, C.; Cao, G. Effect of synthesis pH and EDTA on iron hexacyanoferrate for sodium-ion batteries. Sustainable Energy & Fuels 2020, 4 (6), 2884–2891. https://doi.org/10.1039/d0se00120a.

were 120, 104, 95, and 89 mAh/g, corresponding to capacity retentions of 84, 80, 83, and 80% respectively for PB(3.8), PB(4.0), PB(4.2), and PB(4.4) compared to their 4th cycle at 100 mA/g. The high capacity retention at high current indicates fast intercalation kinetics which can be ascribed to Prussian Blue's unique cage-like structure which can facilitate rapid ion transport. However, further analysis of discharge curves of PB(3.8) and PB(4.4) when current rate increases shows that capacity of the upper voltage plateau attributed to low-spin Fe is disproportionately lost compared to the lower voltage plateau attributed to high-spin Fe (**Figure 5-15**). The asymmetric decrease in capacity between voltage plateaus suggests that the intercalation or redox mechanism of the upper plateau is more impacted by kinetics. Furthermore, the capacity retention of the upper voltage plateau more quickly decreases for the larger microscale particles of PB(4.4) retaining about 32% capacity compared to 61% for PB(3.8) at 3.2 A/g (**Figure 5-17**). In contrast, the lower voltage plateau capacity retains about 97% capacity for PB(4.4) and there is no decrease for PB(3.8). The larger diffusion distance of micrometer-sized particles could be responsible for the decreased electrochemical activity of larger particles grown at higher pH with EDTA, despite having fewer vacancies.

Reproduced in part with permission from Royal Society of Chemistry Copyright 2020.
Neale, Z. G.; Liu, C.; Cao, G. Effect of synthesis pH and EDTA on iron hexacyanoferrate for sodium-ion batteries. Sustainable Energy & Fuels 2020, 4 (6), 2884–2891. https://doi.org/10.1039/d0se00120a.

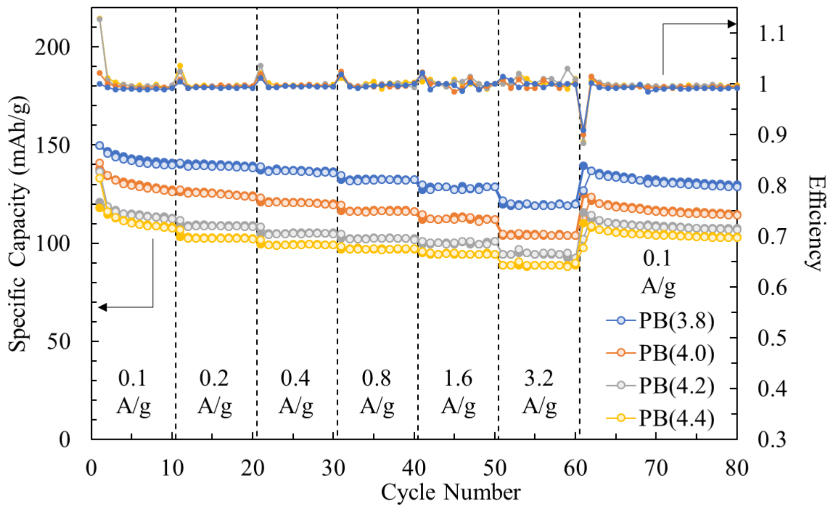

Figure 5-14. Galvanostatic cycling at various current rates. Discharge shown as open circles and charge shown as filled circles.

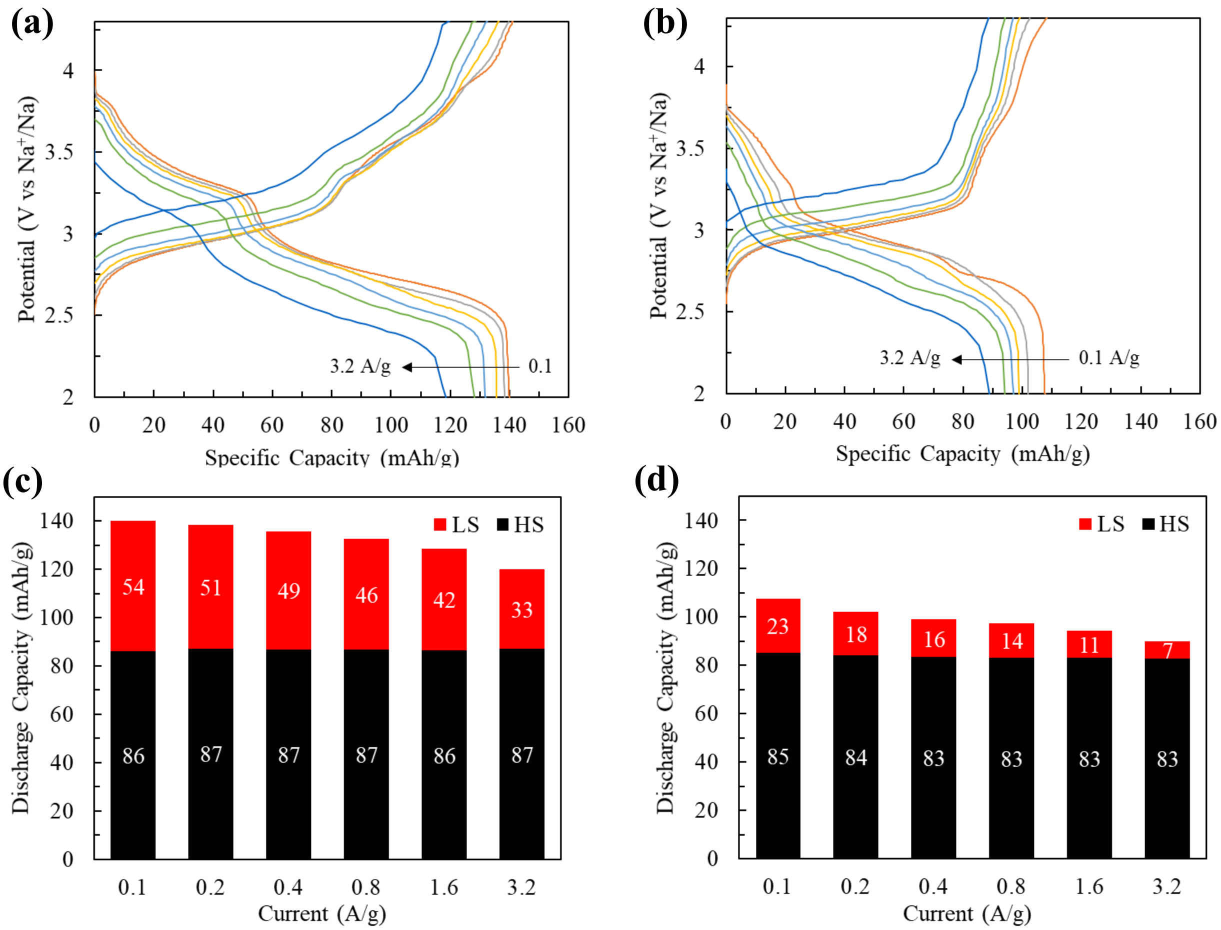

Figure 5-15. Rate performance of PB(3.8) (a) and PB(4.4) (b), and their respective estimated capacity contributions between low-spin and high-spin Fe (c, d).

Reproduced in part with permission from Royal Society of Chemistry Copyright 2020.
Neale, Z. G.; Liu, C.; Cao, G. Effect of synthesis pH and EDTA on iron hexacyanoferrate for sodium-ion batteries. Sustainable Energy & Fuels 2020, 4 (6), 2884–2891. https://doi.org/10.1039/d0se00120a.

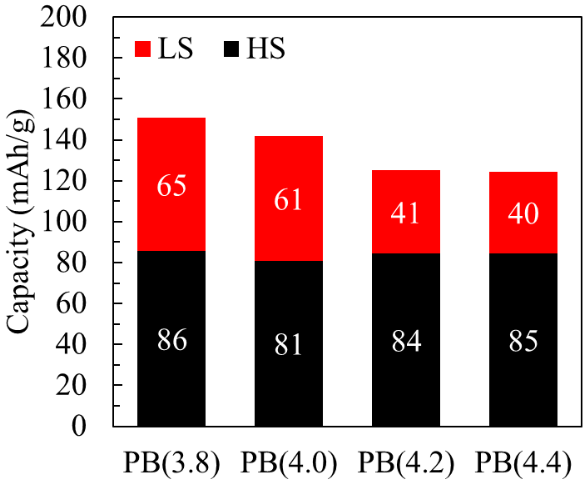

Figure 5-16. High-spin and low-spin Fe reduction capacity contributions for first discharge cycle at 100 mA/g. Low-spin capacity contribution approximated as discharge capacity associated with the high-voltage plateau.

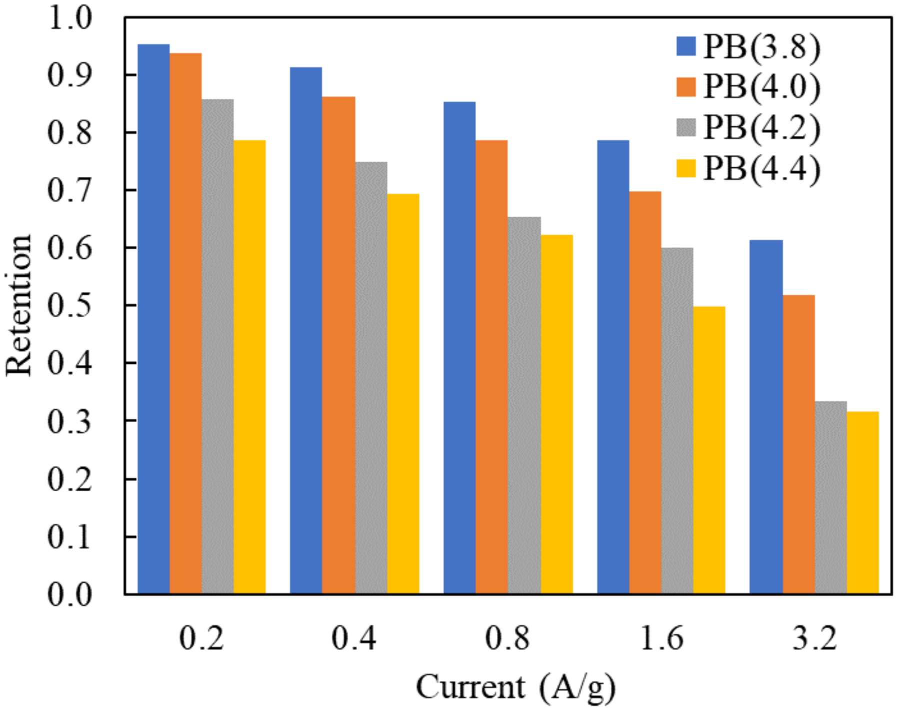

Figure 5-17. Approximate capacity retention of low-spin Fe reduction at increasing discharge rate compared to 0.1 A/g.

Reproduced in part with permission from Royal Society of Chemistry Copyright 2020.
Neale, Z. G.; Liu, C.; Cao, G. Effect of synthesis pH and EDTA on iron hexacyanoferrate for sodium-ion batteries. Sustainable Energy & Fuels 2020, 4 (6), 2884–2891. https://doi.org/10.1039/d0se00120a.

Kinetics were further explored with electrochemical impedance spectroscopy (EIS) on PB(3.8) and PB(4.4) batteries in the charged state after galvanostatic cycling. Nyquist plots (**Figure 5-18**) show a high frequency semi-circle representing charge transfer resistance and a low-frequency tail indicating Warburg diffusion. PB(4.4) has slightly larger charge transfer resistance than PB(3.8). The Warburg diffusion tails can be analyzed to estimate the nominal sodium diffusion coefficient of the FeHCF electrode by the following:

$$\sigma = \frac{RT}{n^2F^2A\sqrt{2}}\left(\frac{1}{C_{Na}D_{Na}^{1/2}}\right) \tag{5-1}$$

The Warburg coefficient, σ, is the slope of real impedance versus the inverse square root of frequency in the low frequency region (**Figure 5-18b**). R is the gas constant, T is temperature, n is the number of electrons transferred during intercalation, F is the Faraday constant, A is surface area which is estimated in this case as the electrode surface area, C_{Na} is the molar concentration of sodium ions which is set to 0.001 mol/cm^3, and D_{Na} is the nominal diffusion coefficient of sodium ions. Solving for D_{Na} results in values of 7×10^{-12} and 2×10^{-11} cm^2/s respectively for PB(3.8) and PB(4.4). Although this result may not be accurate because of the assumption for sodium ion concentration which may be different between the two samples.

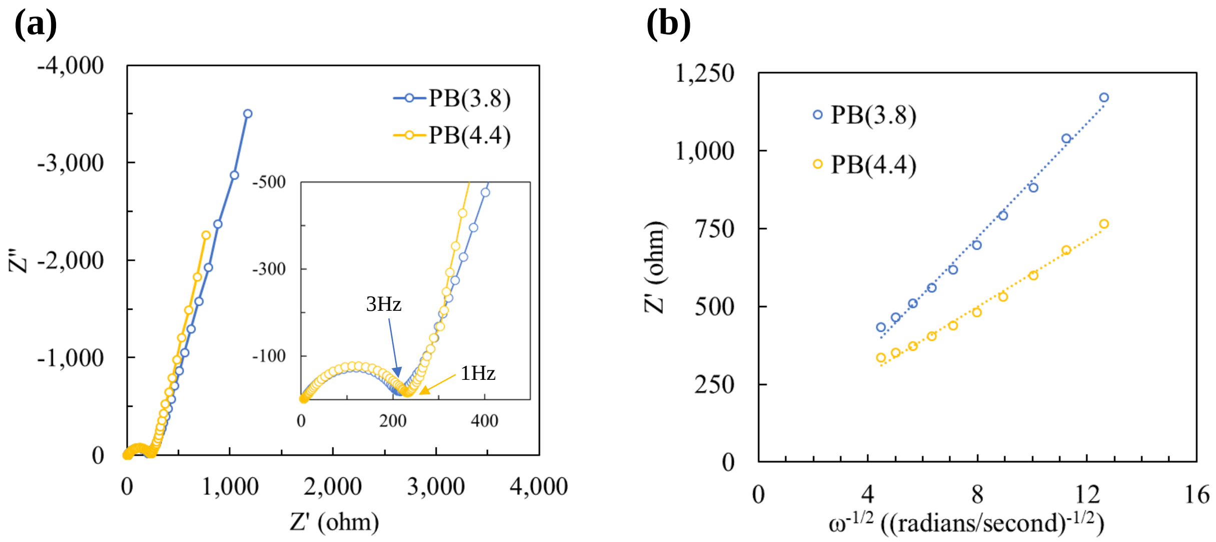

Figure 5-18. EIS spectra of PB(3.8) and PB(4.4) in the charged state after galvanostatic cycling (a). Plot of real impedance vs inverse square root of angular frequency (b).

Diffusion kinetics were also analyzed between PB(3.8) and PB(4.4) using cyclic voltammetry at different scan speeds (**Figure 5-19**). The nominal diffusion coefficient was estimated at four different current peaks using the Randles-Sevcik equation at 25°C:

$$i_p = 268{,}600\, n^{3/2} A D^{1/2} C v^{1/2} \tag{5-2}$$

The slope of the peak current i_p versus square root of scan speed $v^{1/2}$ were determined for each of the four redox peaks, n is the number of electrons transferred during reaction, A is the electrode surface area, D is the nominal diffusion coefficient, and C is the molar concentration of sodium in the host for a given peak which was estimated by finding the capacity at the peak position of the slowest scan speed. The individual parameters and diffusion coefficients are listed in **Table 5-3** and the average diffusion coefficient of the four redox peaks is 4×10^{-10} and 2×10^{-10} cm^2/s for PB(3.8) and PB(4.4). These results differ from the diffusion coefficients estimated by EIS because the sodium concentration was set to 0.001 mol/cm^3 for those calculations since it was

Reproduced in part with permission from Royal Society of Chemistry Copyright 2020.
Neale, Z. G.; Liu, C.; Cao, G. Effect of synthesis pH and EDTA on iron hexacyanoferrate for sodium-ion batteries. Sustainable Energy & Fuels 2020, 4 (6), 2884–2891. https://doi.org/10.1039/d0se00120a.

unable to be determined in the charged state after cycling. The close proximity in nominal diffusion coefficient and similar capacity retentions at high current rate suggest that the large particle size of PB(4.4) is not a major contributor to its lower capacity compared to PB(3.8). Furthermore, the *b* values are relatively close to 1. The *b* value parameter shows if a reaction is surface limited or diffusion limited. A high *b* value close to 1 means that charge storage is predominantly surface controlled, indicating capacity is not bulk diffusion limited. The *b* values greater than 1 in **Table 5-3** are not possible and probably arise because the peaks they are derived from are composites of several hidden peaks.

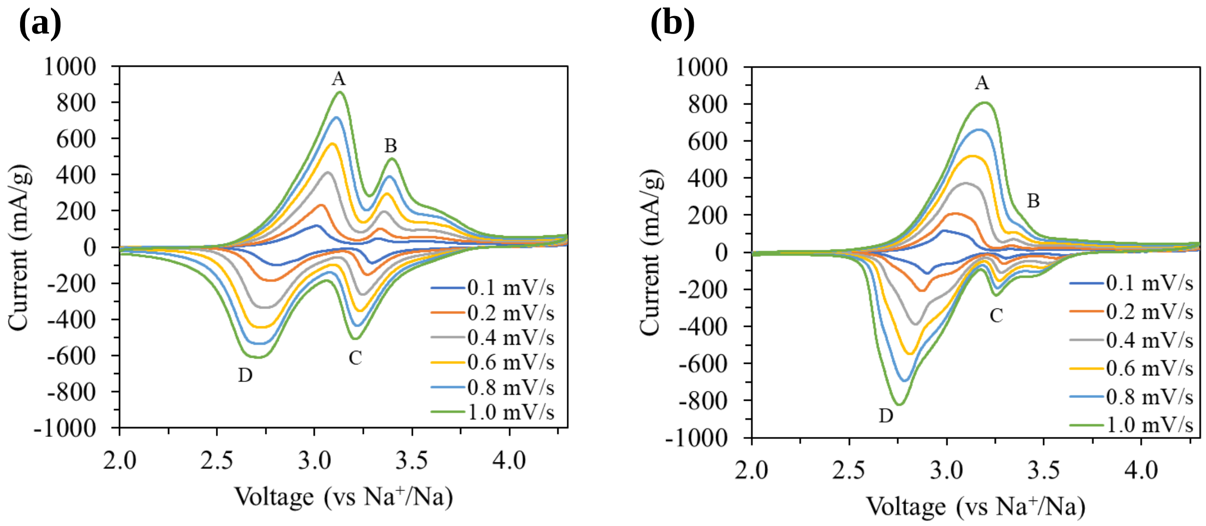

Figure 5-19. Cyclic voltammetry of PB(3.8) (a) and PB(4.4) (b) at various scan speeds

Reproduced in part with permission from Royal Society of Chemistry Copyright 2020.
Neale, Z. G.; Liu, C.; Cao, G. Effect of synthesis pH and EDTA on iron hexacyanoferrate for sodium-ion batteries. Sustainable Energy & Fuels 2020, 4 (6), 2884–2891. https://doi.org/10.1039/d0se00120a.

Table 5-3. Parameters derived from cyclic voltammetry results of PB(3.8) and PB(4.4).

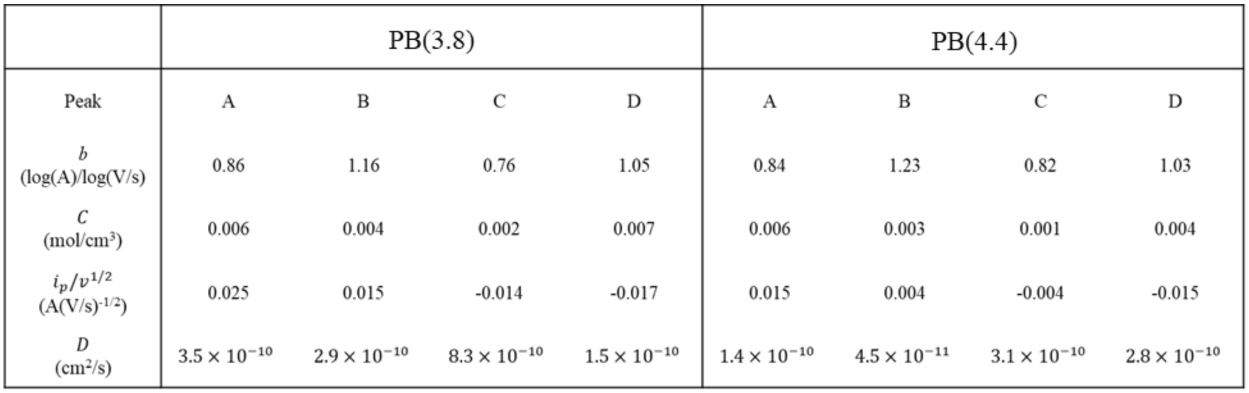

	PB(3.8)				PB(4.4)			
Peak	A	B	C	D	A	B	C	D
b (log(A)/log(V/s))	0.86	1.16	0.76	1.05	0.84	1.23	0.82	1.03
C (mol/cm^3)	0.006	0.004	0.002	0.007	0.006	0.003	0.001	0.004
$i_p/v^{1/2}$ (A(V/s)$^{-1/2}$)	0.025	0.015	-0.014	-0.017	0.015	0.004	-0.004	-0.015
D (cm^2/s)	3.5×10^{-10}	2.9×10^{-10}	8.3×10^{-10}	1.5×10^{-10}	1.4×10^{-10}	4.5×10^{-11}	3.1×10^{-10}	2.8×10^{-10}

5.4 Conclusions

The effect synthesis pH and EDTA had on FeHCF growth and its influence on sodium ion battery performance was investigated. Increasing synthesis pH results in slower nucleation kinetics leading to increased particle size, fewer anion vacancies, and decreased water content. However, galvanostatic cycling illustrated that FeHCF synthesized with EDTA at lower pH had increased capacity with more prevalent low-spin Fe redox activity and increased rate performance, but also suffered from faster cyclic decay.

It was originally hypothesized that particles with fewer vacancies would have improved capacity. While this still may be possible, rate-dependent results illustrate that any gains in capacity because of fewer vacancies were overshadowed by kinetic limitations of the low-spin Fe redox reaction. On the other hand, kinetic limitations due to large particle size was not a serious factor as illustrated by the competent rate capability of high-spin capacity contribution and higher lithium-ion diffusivity of PB(4.4). Therefore, the electrochemical activity of low-spin Fe could be more affected by electronic properties influenced by vacancies.

In summary, growth of FeHCF faceted particles with EDTA can be controlled by the adjustment of synthesis pH that results in significant changes in their electrochemical activity over a small pH range. These findings suggest that pH should be carefully considered especially when utilizing a chelating agent in other procedures of FeHCF synthesis.

Chapter 6: Doping of iron hexacyanoferrate

6.1 Introduction

Ion doping can affect mechanical properties of materials such as yield strength and electronic properties such as conductivity and band structure. Nickel doping of iron hexacyanoferrate (FeHCF), or Prussian blue, has shown increased redox activity of low-spin iron, speculated to be caused by decreased Fe-C bond force.[77] Other multivalent transition metal ions can easily be incorporated into the FeHCF crystal structure. Doping and substitution of ions in FeHCF is typically done with the high-spin iron ion while keeping the hexacyanoferrate component. For example, in the ideal chemical structure $A_xM[Fe(CN)_6]$, *A* is the monovalent ion such as sodium and *M* is the transition metal cation that is substituted. Fully substituted *M* species can create Prussian blue analogs (PBAs) of the same or similar crystal structure. For example, replacing high-spin Fe with Co or Mn to create CoHCF and MnHCF result in in increased redox potential, while replacing with Ni to form NiHCF increases cyclic stability at the expense of capacity.[68,130,131]

6.2 Zinc-substitution in FeHCF

Zinc ions can be partially substituted for high-spin iron during synthesis FeHCF. The 6-coodrinate Zn^{2+} ion has a smaller ionic radius of 0.74 Å compared to Fe^{2+} at 0.78 Å.[97] Zinc-doped FeHCF has been investigated as a material to enhance photothermal ablation of bacteria used in near-infrared photothermal therapy, where zinc-doping results in band-gap narrowing of FeHCF.[132] With fully occupied d-orbitals, Zn^{2+} does not exhibit any reversible oxidation reaction within a reasonable voltage range, thus loss of capacity would be expected for significant substitution of high-spin Fe^{2+} for Zn^{2+}. Additionally, higher concentrations of Zn^{2+} results in a crystal phase transformation to rhombohedral $Zn_3[Fe(CN)_6]_2$ (ZnHCF) with zinc ions in tetrahedral coordination with the nitrogen of $Fe(CN)_6$ octahedra, although hydrated ZnHCF is able to retain an unstable cubic structure.[133] It should be noted that the rhombohedral ZnHCF phase is significantly different than the rhombohedral sodium-rich phase of FeHCF which still retains octahedral coordination of high-spin Fe ions.[111] ZnHCF has been investigated as a cathode material for aqueous zinc-ion batteries with high working voltage (~1.7 V vs Zn^{2+}/Zn) but limited specific capacity (~80 mAh/g).[134]

In this work, zinc-doped FeHCF and ZnHCF at higher zinc concentrations were synthesized and characterized as cathodes for non-aqueous sodium-ion batteries. FeHCF was synthesized by mixing 100 mL of 0.02 M $Na_4Fe(CN)_6$ solution with 100 mL of 0.03 M $FeCl_2$ and 0.03 M ethylenediaminetetraacetic acid (EDTA) solution at room temperature for 24 hours. Both precursor solutions were made from a 0.3 M acetate buffer at pH 4. Zinc-doped FeHCF and ZnHCF samples were made by substituting $FeCl_2$ for $ZnCl_2$ at concentrations of 1, 3, 5, 10, 20, 50, and 100% (labeled as Zn-1, Zn-3, Zn-5, Zn-10, Zn-20, Zn-50, and Zn-100). The resulting precipitates were washed with water and dried at 80 °C for 12 hours.

XRD shows Zn-FeHCF retains its cubic $Fm\bar{3}m$ crystal structure up to 20% substitution which has a mix of cubic and rhombohedral $R\bar{3}c$ phase (**Figure 6-1a**). At 50% and 100% Zn substitution the material is entirely rhombohedral phase. Increasing Zn^{2+} concentration of the cubic phase results in decreasing lattice parameter from 10.26 Å for Zn-0 to 10.22 Å for Zn-10 attributed to the smaller ionic radius of Zn^{2+} compared to Fe^{2+} (**Figure 6-1b**). The coexistence of both cubic and rhombohedral phases at 20% Zn represents a two-phase region of an iron-rich cubic phase and a zinc-rich rhombohedral phase with zinc and iron solubility limits for each phase (**Figure 6-3**). It should be noted that these percentages represent the concentration of Zn^{2+} substituted for Fe^{2+}

during synthesis, which may not be consistent with the actual Zn^{2+} concentration incorporated into the material. The chelation strength between EDTA and Zn^{2+} is stronger than Fe^{2+},[135] thus it might be expected that less Zn^{2+} is incorporated into the structure than the percentage prescribed during synthesis. On the other hand, Fe^{2+} easily oxidizes to Fe^{3+} which has a significantly stronger chelation strength with EDTA.

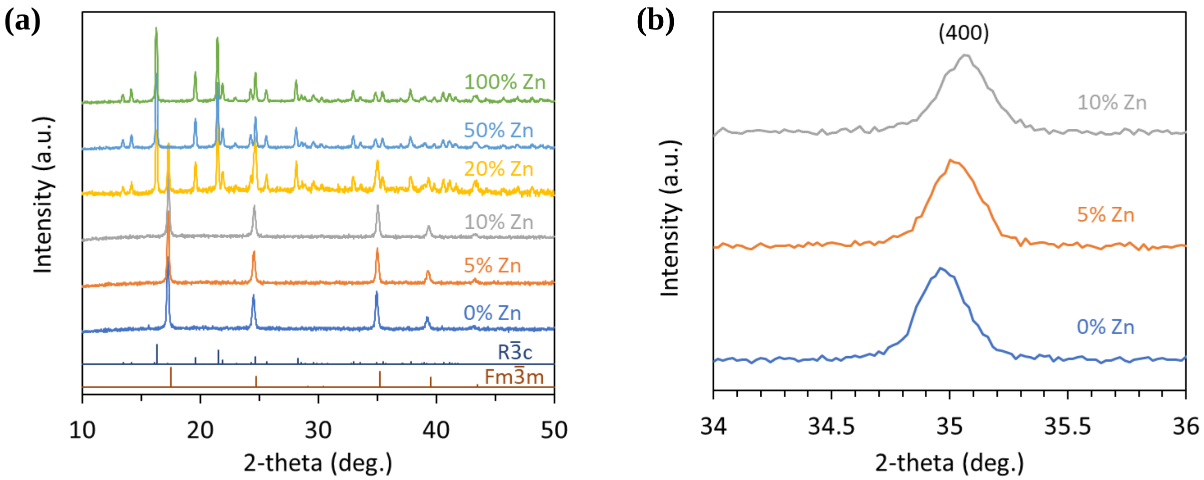

Figure 6-1. XRD patterns of zinc-substituted iron hexacyanoferrate and the reference patterns of cubic Fm$\bar{3}$m Prussian blue and rhombohedral R$\bar{3}$c zinc hexacyanoferrate (a) and zoomed view of the (400) peak of 0, 5, and 10% doped iron hexacyanoferrate (b).

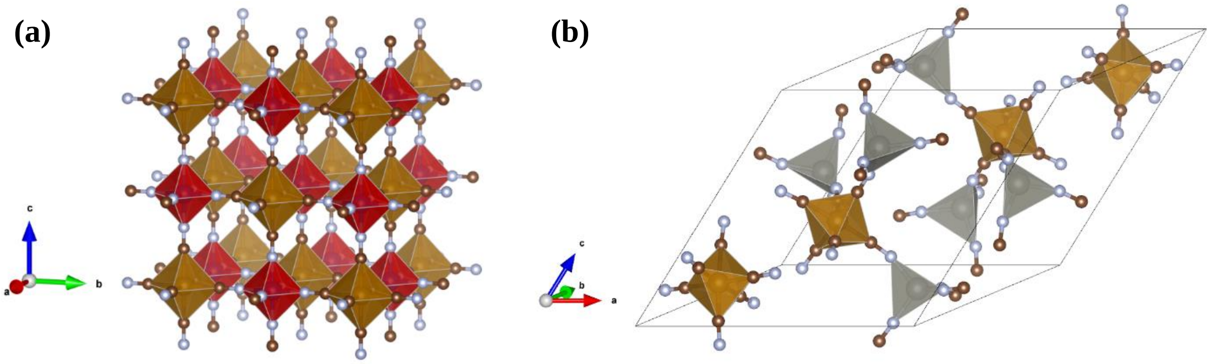

Figure 6-2. Unit cell model of (a) cubic Fe[Fe(CN)$_6$] and (b) rhombohedral Zn$_3$[Fe(CN)$_6$]$_2$. FeC$_6$ octahedra shown in orange, FeN$_6$ octahedra shown in red, and ZnN$_4$ tetrahedra shown in gray. Model generated on VESTA software developed by Koichi Momma and Fujio Izumi.

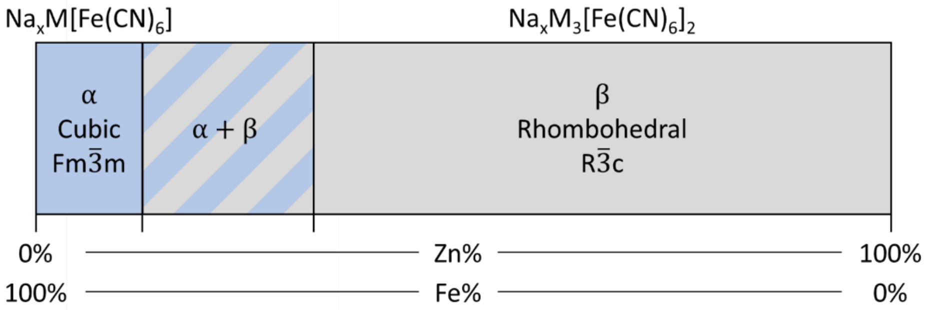

Figure 6-3. 1-dimensional phase diagram of Zn-substituted FeHCF. ***α*** represents cubic FeHCF structure and ***β*** represents rhombohedral ZnHCF structure.

Electrodes were made from a slurry of 70% active material, 20% carbon powder, and 10% sodium carboxymethyl cellulose binder dissolved in water and doctor bladed onto aluminum foil and dried under vacuum at 80 ^{o}C for 12 hours. Sodium metal battery coin cells were made in an argon glovebox using a glass fiber separator and 1 M $NaClO_4$ in propylene carbonate electrolyte with 5 vol% fluoroethylene carbonate additives.

Galvanostatic cycling at 100 mA/g of samples with rhombohedral phase display limited sodium ion capacity (**Figure 6-4**). The theoretical specific capacity of dehydrated rhombohedral ZnHCF with ideal chemical formula $Na_2Zn_3[Fe(CN)_6]_2$ is 80 mAh/g due to the inactive Zn^{2+} ions. The initial charge half-cycle resulted in decent capacity above 60 mAh/g corresponding to desodiation and Fe^{2+} oxidation. The following discharge cycle had capacities of 63, 48, and 36 mAh/g for Zn-20, Zn-50, and Zn-100 respectively. The higher capacity of Zn-20 is likely due to the presence of cubic Fe-rich phase. Similarly, the higher capacity of Zn-50 could be due to the presence of tetrahedral Fe ions in place of Zn that could help contribute to the capacity.

In contrast to rhombohedral ZnHCF, the Zn-doped FeHCF samples that retain cubic phase have significantly higher capacities, with first discharge capacities at 200 mA/g of 142, 137, 137, 131, and 125 mAh/g for Zn-0, Zn-1, Zn-3, Zn-5, and Zn-10 respectively (**Figure 6-5**). This cannot only be attributed to the greater concentration of redox active high-spin iron in these lower Zn-concentration samples. In relation to the theoretical capacity of $Na_2Fe[Fe(CN)_6]$ (171 mAh/g), the cubic FeHCF samples obtained between 73-83% of theoretical capacity on their first discharge, while rhombohedral ZnHCF only obtained 45-60% of the theoretical capacity of $NaZn_3[Fe(CN)_6]_2$ (80 mAh/g) for Zn-50 and Zn-100. The improved sodium ion capacity of cubic FeHCF could be related to improved kinetics. This could be due to faster diffusion in cubic FeHCF which has straight channels for sodium ion diffusion in 3 dimensions. Additionally, kinetics could be impacted by electronic structure of ZnHCF. Zn^{2+} ions have a fully occupied d-orbital shell which would not as easily facilitate electron hopping between metal ions like in FeHCF with $Fe^{2/3+}$ ions that have partially filled d-orbitals.

Higher Zn-doping in cubic FeHCF samples results in lower capacity as previously illustrated. This trend may be expected due to the inactivity and heavier mass of Zn^{2+} ions; however, the loss in capacity is not proportional between high-voltage and low-voltage redox plateaus which correspond to low-spin and high-spin Fe redox reactions. Inspecting the 20th cycle reveals that in general as zinc concentration increases the capacity contribution above 3.1 V also increases, but the capacity contribution below 3.1 V decreases (**Figure 6-6**). The lower capacity contribution below 3.1 V could be because more inactive Zn^{2+} is replacing high-spin Fe^{2+}. The increased capacity above 3.1 V is similar to what has previously been reported for Ni-doping of FeHCF and the previous study of pH controlled synthesis that influenced vacancy concentration.[77,136] What is common between these three studies is a decreasing lattice parameter associated with increasing low-spin Fe activity. Both chemical substitution and vacancy introduction will influence electronic properties of FeHCF, which likely has an impact on the redox activity of low-spin Fe.

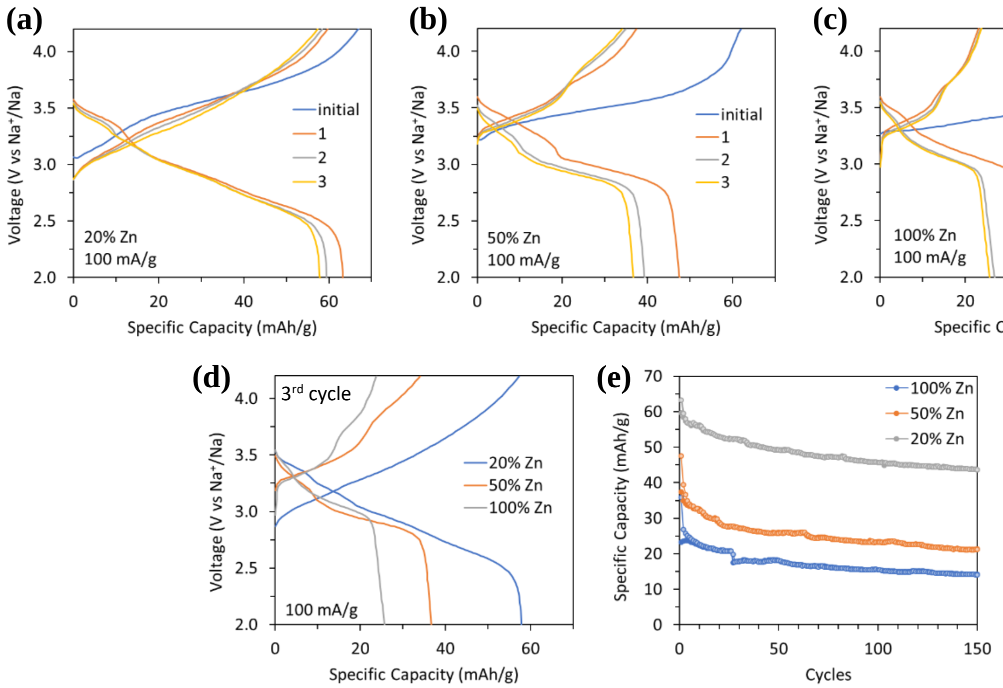

Figure 6-4. Galvanostatic profiles at 100 mA/g of zinc-substituted iron hexacyanoferrate for 20% (a), 50% (b), and 100% (c) $ZnCl_2$ substitution for $FeCl_2$ during synthesis. The 3rd cycle of each sample is compared (d). Galvanostatic cycling at 100 mA/g for rhombohedral zinc-substituted iron hexacyanoferrate (e). Discharge capacities shown as open shaded markers and charge capacities shown as solid filled markers.

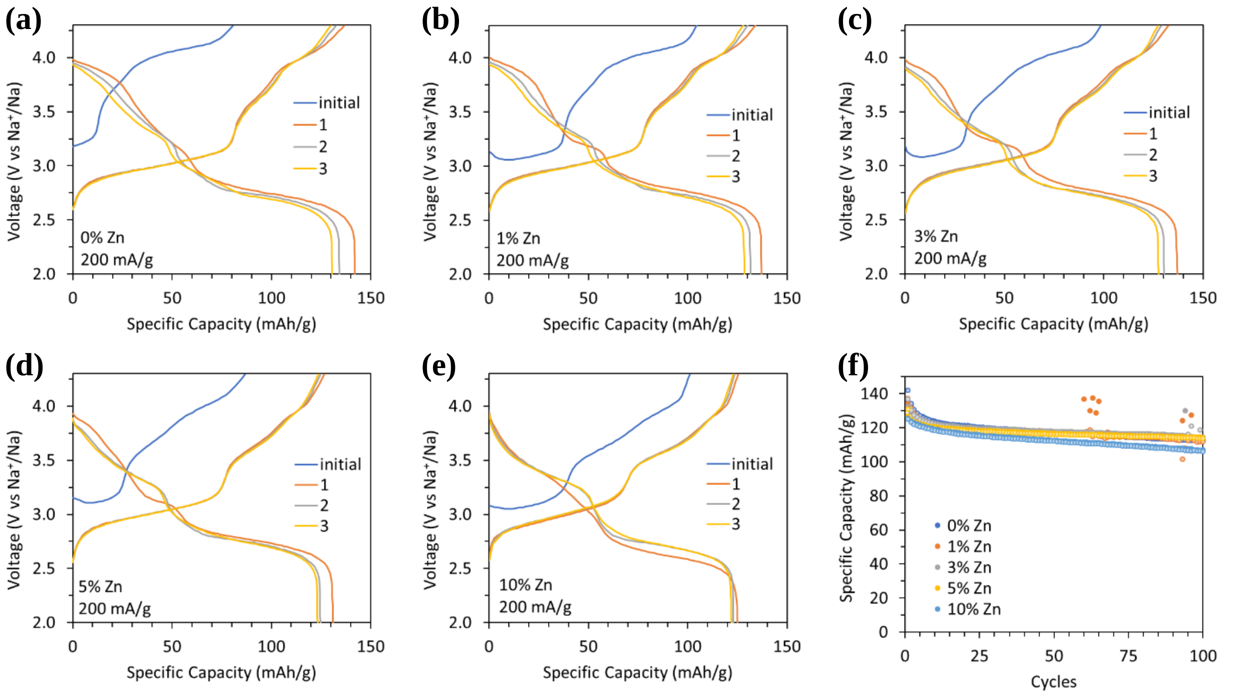

Figure 6-5. Galvanostatic profiles at 200 mA/g of zinc-substituted iron hexacyanoferrate for 0% (a), 1% (b), 3% (c), 5% (d), and 10% (e) $ZnCl_2$ substitution for $FeCl_2$ during synthesis. Cyclic capacity of samples at 200mA/g (f).

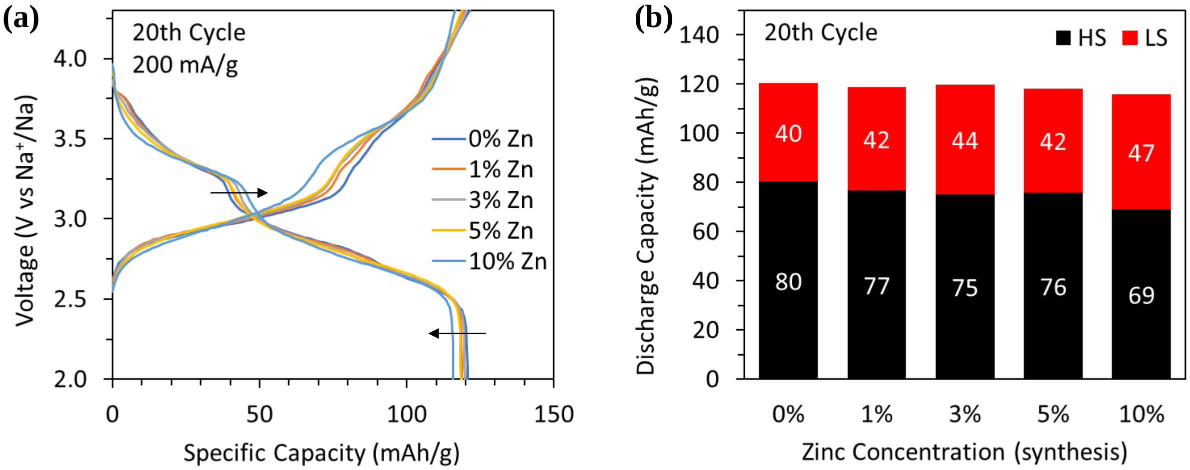

Figure 6-6. Galvanostatic profiles of the 20th cycle at 200 mA/g of zinc-substituted iron hexacyanoferrate (a) and the approximate capacity contributions of low-spin (red) and high-spin (black) iron redox reaction determined by capacity above and below 3.1 V (b).

6.3 Mn-doping of Prussian white

Prussian white (PW) is the fully reduced phase of Prussian blue (PB) with ideal chemical formula $Na_2Fe[Fe(CN)_6]$. The high concentration of sodium induces a lattice distortion from cubic $Fm\bar{3}m$ structure to rhombohedral $R\bar{3}$ structure or hydrated monoclinic $P2_1/n$ structure.[71,74,137,138] All three structures of FeHCF still retain octahedral coordination of high-spin and low-spin iron species. Direct synthesis of Prussian white is preferable as a battery cathode over partially reduced Prussian blue because its fully reduced state would be advantageous when paired with a fully oxidized anode. Prussian white when exposed to air changes color to cyan or light blue, probably an indication of slight iron oxidation. Similarly, synthesis of Prussian white must be done under a reductive environment to prevent oxidation of iron species. Typically, reducing agents such as ascorbic acid and addition of nitrogen sparging are used during synthesis to minimize oxidation.

In this work, Prussian white was synthesized with manganese doping through a hydrothermal co-precipitation route. Mn^{2+} has a larger ionic radius of 0.83 Å than Fe^{2+} at 0.78 Å. Additionally, $Mn^{3/2+}$ has a higher standard reduction potential than $Fe^{3/2+}$. Mn^{2+} has 5 *d* electrons which completely half-fill the d-orbitals in octahedral configuration; however, octahedral Mn^{3+} compounds typically undergo Jahn-Teller distortion to alleviate the d-orbital degeneracy.

Prussian white was synthesized by slowly dripping 50 mL of a 0.06 M solution of $FeCl_2$ at approximately 1 drop per second into a stirring 50 mL solution of 0.06 M $Na_4Fe(CN)_6$ and 0.02 M ascorbic acid at 80 ºC and under N_2 sparging for 20 hours. Precipitate was washed with water and dried at 80 °C in air (**Figure 6-7**). The product turned light blue during washing with water. Mn-doped samples were made in the same method by substituting $FeCl_2$ with $MnCl_2$. Samples were made with 0%, 5%, and 10% Mn-doping (labeled as Mn-0, Mn-5, and Mn-10).

Mn-0 and Mn-5 displayed the monoclinic $P2_1/n$ phase typical of hydrated Prussian white with high sodium content, while Mn-10 displayed a single (220) peak (**Figure 6-8**). The presence of cubic phase is an indication of lower sodium content; however, Mn^{2+} having a higher oxidation potential than Fe^{2+} should be less prone to oxidation during synthesis and allow for greater incorporation of Na^+ ions. The addition of larger Mn^{2+} ions may influence $[Fe(CN)_6]$ vacancies or allow more space for higher Na^+ concentration before distorting to monoclinic phase.

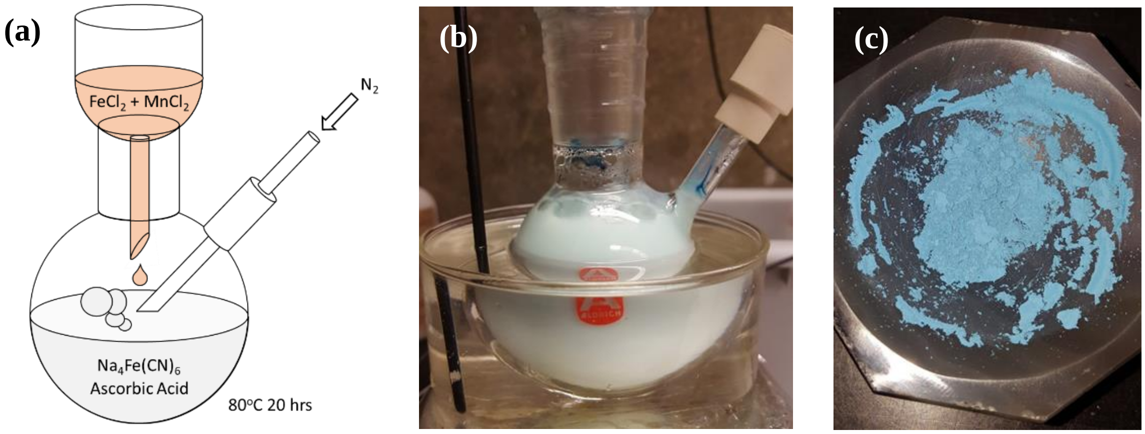

Figure 6-7. Diagram of experimental setup (a), precipitation of Prussian white under N_2 sparging (b), and dried Prussian white product that has turned cyan (c).

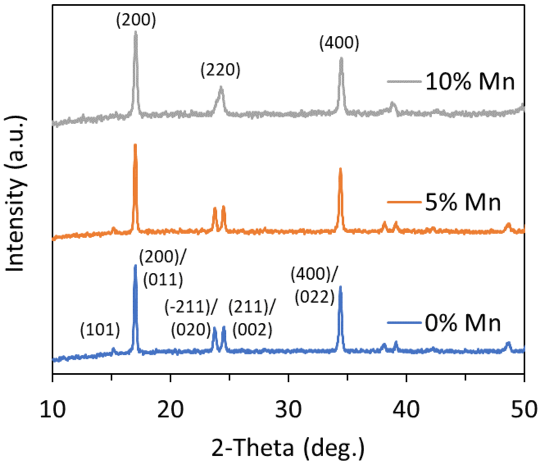

Figure 6-8. XRD patterns of Mn-doped Prussian white with the *hkl* indices of cubic $Fm\bar{3}m$ and monoclinic $P2_1/n$ phases.

Electrodes were made by preparing a slurry of 70% Prussian white material, 20% carbon powder, and 10% sodium carboxymethyl cellulose binder dissolved in water. The slurry was doctor bladed onto aluminum foil and dried under vacuum at 80 °C for 12 hours. Sodium metal half-cell batteries were assembled in an argon glovebox using 1 M $NaClO_4$ in propylene carbonate electrolyte.

Cyclic voltammetry at 0.1 mV/s between 2.25-4.25 V reveal many redox peaks corresponding to reduction and oxidation of high-spin and low-spin Fe species (**Figure 6-9**). The presence of water in the FeHCF crystal also has been shown to influence the site energy of sodium intercalation, which may add additional redox peaks.[127] Between the first and second cycle there is a large decrease in current density of the peaks between 3.8-4.0 V, but is replaced by an increase in current density of peaks between 3.2-3.6 V. This is likely due to a loss of hydrated sodium ions during the initial charge cycle. Hydrated sodium ions may give rise to the high redox potential between 3.8-4.0 V.[71,112,127,139] Upon the first deintercalation, many of the hydrated ions may dissociate and become replaced by dehydrated sodium on the next intercalation cycle which results in a lower redox potential of FeHCF.

There are no apparent new redox peaks between Mn-0 and Mn-10 that would indicate the presence of a $Mn^{3/2+}$ redox reaction. The reported voltage plateau of high-spin Mn in MnHCF is between 3.48-3.60 V; however, this also overlaps with reported voltage plateaus of low-spin Fe in FeHCF between 3.23-3.80.[68] The redox peaks of Mn-doped samples increased in current density and became sharper, except for the redox pair between 3.8-4.0 V which became lower in intensity for Mn-10. Increased current density could be indicative of higher redox activity. Additionally, the redox potential between 2.6-3.0 V corresponding to high-spin Fe shifts to higher voltage in Mn-10. Similarly, the reduction potential of low-spin Fe at 3.25 and 3.89 V for Mn-0 become lower with increased Mn content to 3.22 and 3.81 V for Mn-10. This shows that the addition of Mn to FeHCF influences the local chemical environment of the Fe species and increases with Mn concentration.

The initial charge capacities during galvanostatic cycling at 10 mA/g were 130, 146, and 143 mAh/g for Mn-0, Mn-5, and Mn-10 respectively (**Figure 6-10**). The high initial charge capacities are evidence of high sodium incorporation during synthesis. The higher initial capacity of Mn-5 and Mn-10 could be because Mn^{2+} is less prone to oxidation than Fe^{2+} and would be able to incorporate more Na^+ into the structure during synthesis. In corroboration with CV results, the voltage plateau corresponding to high-spin Fe^{3+} reduction is higher with increased Mn content, but the capacity contribution of this plateau is also reduced (**Figure 6-11**). The reduction in capacity below 3 V corresponds to the replacement of high-spin Fe with high-spin Mn which has a higher redox potential. The increased capacity of the reduction plateau around 3.3 V in Mn-10 could reflect the contribution from high-spin $Mn^{3/2+}$.

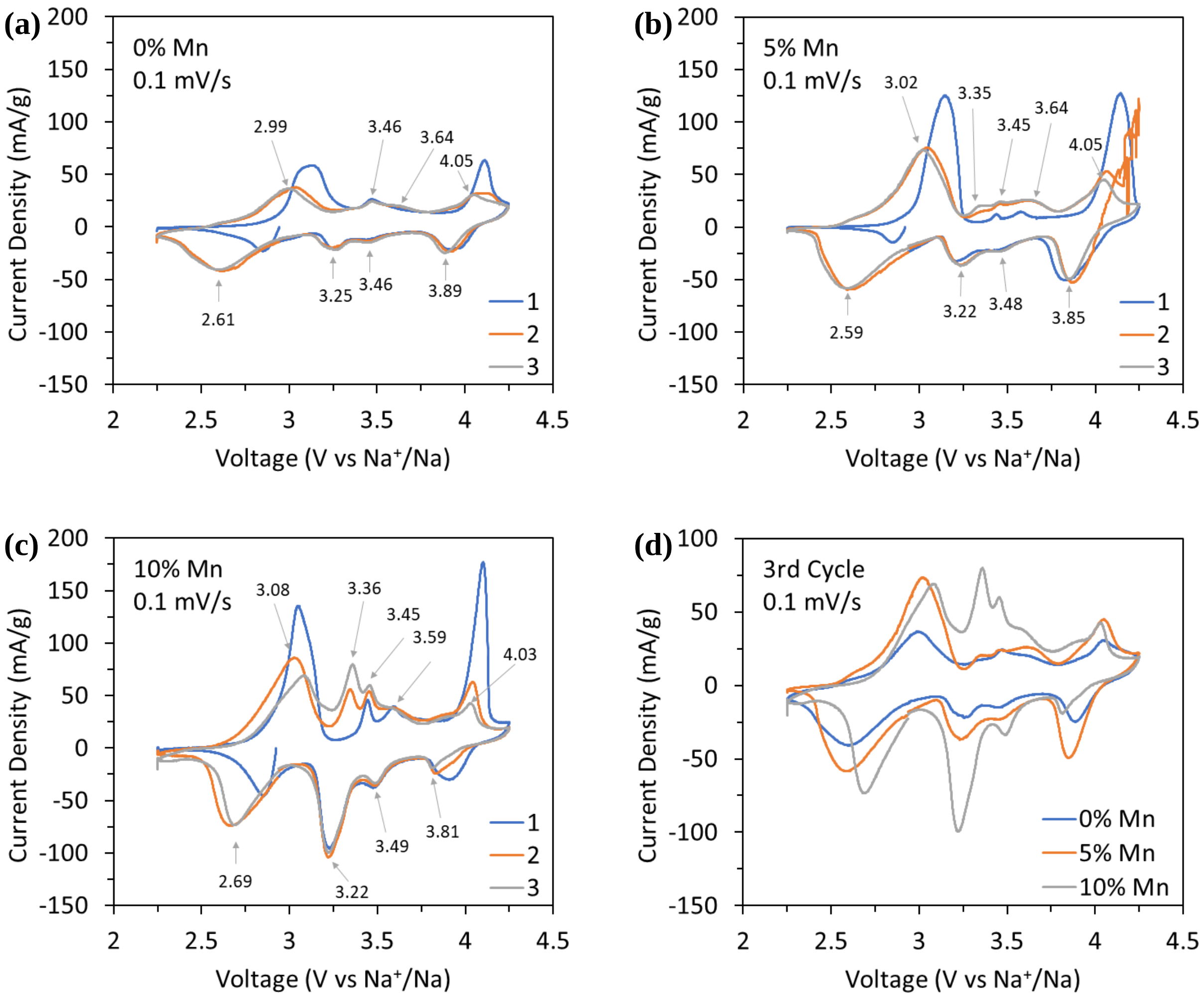

Figure 6-9. Cyclic voltammetry at 0.1 mV/s for 0% (a), 5% (b), and 10% (c) Mn-doped Prussian white. Comparison of 3rd cycle (d).

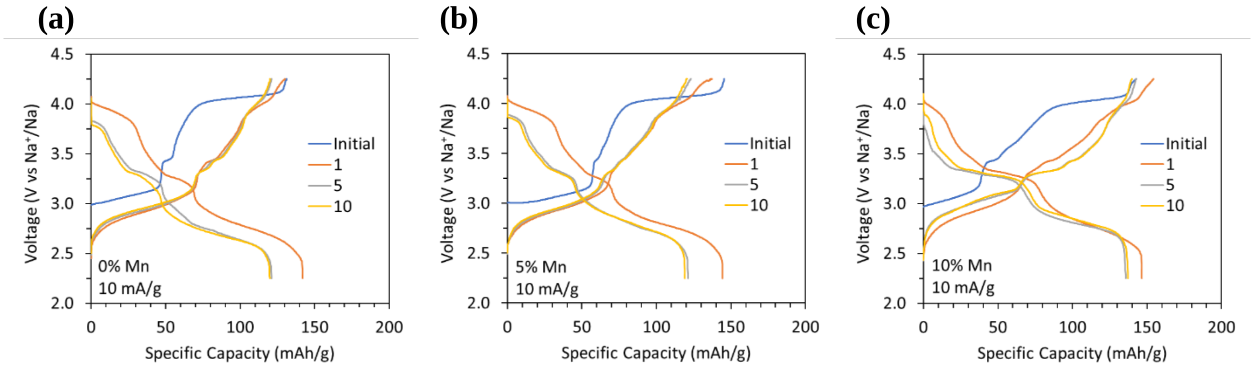

Figure 6-10. Galvanostatic cycling at 10 mA/g between 2.25 – 4.25 V of Prussian white samples with 0% (a), 5% (b), and 10% (c) Mn-doping.

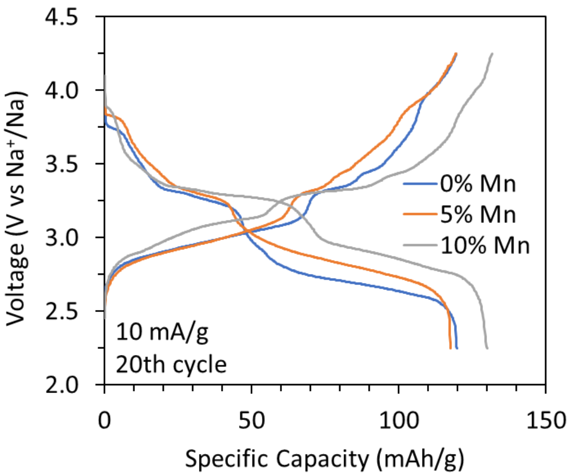

Figure 6-11. Comparison of 20th cycle at 10 mA/g of Mn-doped Prussian white sodium-ion batteries.

The cyclic stability and rate performance of Mn-10 was inferior to Mn-0 and Mn-5 (**Figure 6-11**). The poor cyclability of Mn-10 is similar to reported MnHCF and could be caused by the Jahn-Teller distortion of Mn^{3+} which would degrade the structural stability of FeHCF.[131,140] The Jahn-Teller theorem is that a non-linear coordinated species will have an energetic driving force to undergo a geometric distortion of coordinated ligands in order to alleviate a degenerate electronic state.[141] In the case of high-spin Mn^{3+} with 4 d-electrons in octahedral coordination, there exists a single electron between the d_{z^2} and $d_{x^2-y^2}$ orbitals. In order to remove this degeneracy and lower energy the octahedral coordination can distort by compression or elongation (**Figure 6-13**). Other transition metal ions like low-spin Fe^{3+} and high-spin Fe^{2+} are also prone to Jahn-Teller distortion, however a weaker Jahn-Teller effect is expected for these ions because the unequally occupied degenerate orbitals occurs in t_{2g} orbitals rather than e_g orbitals.

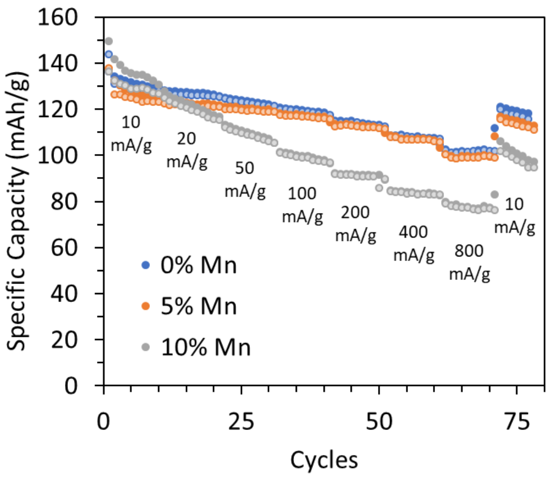

Figure 6-12. Cyclic capacity of Mn-doped Prussian white at different current densities.

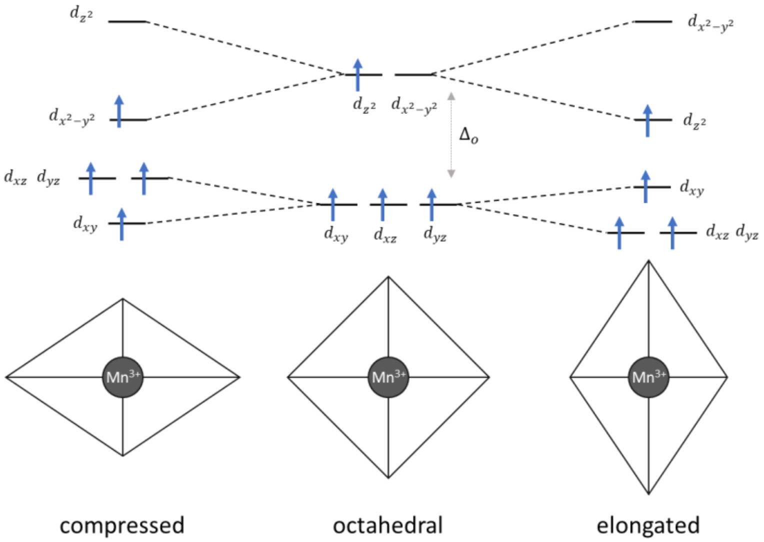

Figure 6-13. Jahn-Teller distortion of Mn^{3+} octahedron.

6.4 Summary

Iron hexacyanoferrate substitution of high-spin Fe for other transition metals such as Zn and Mn can easily be done during synthesis through co-precipitation. Higher concentrations of Zn-substitution in FeHCF result in a change in crystal phase to rhombohedral structure with tetrahedral metal ion coordination. The rhombohedral phase of ZnHCF had severely stunted capacity compared to the cubic phase of FeHCF, in part due to the high concentration of inactive Zn replacing high-spin Fe. Zn-doping at lower concentrations had the effect of increasing low-spin Fe redox activity, despite lower overall capacity. Doping FeHCF with Mn resulted in higher initial charge capacity, possibly due to the higher oxidation potential of Mn^{2+} compared to Fe^{2+} during synthesis. However, Mn-doped FeHCF suffered greatly from cyclic decay likely caused by the greater Jahn-Teller distortion of Mn^{3+}.

Doping and ion substitution presents an effective way of tuning the properties of FeHCF. Depending on the individual properties of substitutional ions such as oxidation state, ionic size, and electronic structure, electrochemical properties such as redox activity, voltage, and cyclic activity can be affected.

Chapter 7: Conclusions

This work has demonstrated how chemistry and vacancies impact the electrochemical properties of two iron-based electrode materials, jarosite and iron hexacyanoferrate (FeHCF). Both materials contain redox active $Fe^{3+/2+}$ but behave differently electrochemically. The reduction potential of Fe^{3+} in jarosite is about 2.7 V vs Li^+/Li and in FeHCF there are multiple reduction peaks between 2.7 – 3.8 V vs Na^+/Na (3.0 – 4.1 V vs Li^+/Li). The difference in reduction potential is explained by the differences in local chemical environment surrounding the Fe center. Unlike other iron sulfates such as $LiFeSO_4F$ with high working potential that coordinate two F^- and four oxygens of SO_4^{2-} groups, the FeO_6 octahedra in jarosite coordinate to the oxygen of four OH^- groups that are less electronegative. FeHCF on the other hand has $Fe(CN)_6$ octahedra linked by Fe cations, making two unique iron species in high and low spin states coordinated to N or C of CN^- groups.

The divalent cation substitution between Na^+ and Pb^{2+} in the jarosite structure creates vacant sites that help facilitate lithium-ion diffusion and increase bulk lithium capacity. In order to maintain charge neutrality in the crystal, two Na^+ ions are replaced by every Pb^{2+} ion, introducing vacancies in cation sites. Complete substitution is only possible by ions of similar size, thus smaller divalent cations such as Zn^{2+} and Ca^{2+} were not possible candidates in jarosite. Despite lower theoretical specific capacity of Pb-jarosite, it obtained higher capacity at higher current rates with lithium diffusion orders of magnitude higher. Additionally, the introduction of vacancies and Pb^{2+} improved the cyclic structural stability of the jarosite crystal helping prevent irreversible amorphous phase transformation. This was ascribed to extra space for lattice distortion due to vacancies and improved coulombic attraction between layers from Pb^{2+}.

In contrast, FeHCF synthesis was controlled to influence particle morphology and reduce $Fe(CN)_6$ anion vacancy concentration. In theory, fewer vacancies are desired in order to increase capacity and initial sodium content. It was shown that vacancy concentration could be controlled by synthesis pH due to its influence on chelation strength and nucleation rate. The electrochemical results of FeHCF grown with EDTA at higher pH were unexpected. The larger particles had significantly lower capacity despite having lower water content and vacancy concentration determined by Mössbauer spectroscopy, with corroboration from TGA, CHN, and XES. It was determined that lower capacity originates from poor electrochemical activity from low-spin $Fe(CN)_6$ in larger FeHCF particles. Furthermore, electrochemical properties of FeHCF could be influenced by doping with Zn and Mn through co-precipitation.

In summary, electrochemical properties of electrode materials are dependent on many factors. Some factors such as local chemistry, vacancies, and structure can be manipulated through synthesis in order to improve battery performance. Cation vacancies in jarosite materials can help lithium-diffusivity, while anionic vacancies in FeHCF may increase activity but decrease cyclic stability. This research contributes to the understanding of these potential battery materials and its findings could be applied to similar materials.

Further Work

The findings related to Pb-jarosite and lithium ion diffusion could be explored in the same manner for sodium-ion batteries. Na-jarosite has been previously studied as a cathode for sodium-ion batteries and has been shown to also undergo a amorphous transformation.[142] Sodium ions will be more impacted by kinetic limitations than lithium due to their larger size, thus the introduction of vacancies in Pb-jarosite should be more beneficial in sodium-ion batteries. One interesting question will be the structural stability during sodium-ion intercalation between Pb-jarosite and Na-jarosite. Na-jarosite already has fully occupied 12-coordinate sites before intercalation, thus a structural transformation upon further Na-ion insertion would be expected. On the other hand, Pb-jarosite has vacant 12-coordinate sites that could host the intercalation of Na-ions (**Figure 7-1**).

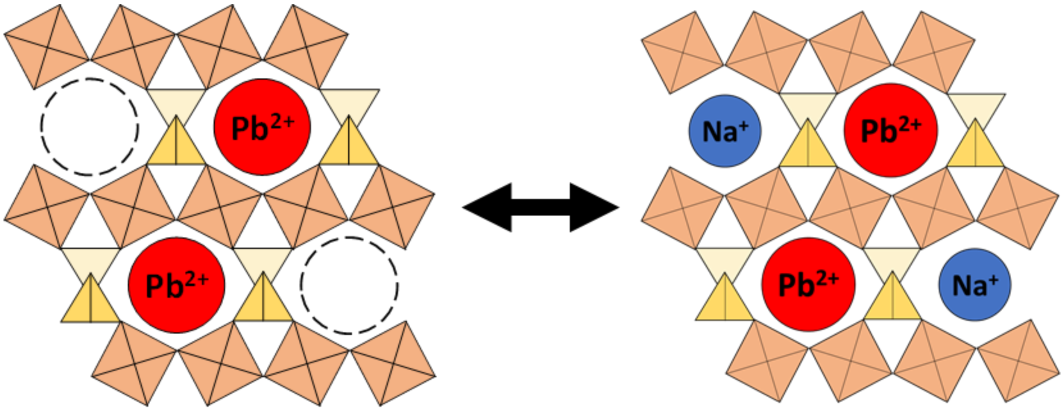

Figure 7-1. Possible sodium intercalation in vacant sites of Pb-jarosite.

In continuation of the study of Jarosite would be to investigate the effect other substitution ions have on its electrochemical properties. Other multivalent cations could be substituted to induce vacancies. The selection of divalent cations could be extended to Ba^{2+} and Sr^{2+} which have 12-coordiante ionic radii near that of Pb^{2+} of 1.61and 1.44 Å respectively (**Figure 7-2**).[97] However, barium is a more acutely toxic compound than lead, and these materials do not exist naturally. The selection of trivalent ions is limited due to the smaller size of these species. Small trivalent ions such as Al^{3+} substitute with Fe^{3+} rather than in the 12-coordinate site. The incorporation of Sc^{3+}, Y^{3+}, and UO_2^{2+} into the jarosite structure has previously been investigated but concluded that end-member analogs could not be synthesized.[143] Sc^{3+} and Y^{3+} are possibly too small of ions and UO_2^{2+} too large to form a stable jarosite compound. The only reasonable trivalent cation would be Bi^{3+}

with a 8-coordinate ionic radius of 1.17 Å and presumably larger 12-coordinate radius.[97] Furthermore, Bi^{3+} forms a stable compound when SO_4^{2-} is replaced by PO_4^{3-}, forming $BiFe_3(PO_4)_2(OH)_6$, of the alunite group with the same $R\bar{3}m$ crystal structure as jarosite.[144] However, one remaining issue of synthesis of hypothetical $Bi_{0.33}Fe_3(SO_4)_2(OH)_6$ would be its structural stability. The introduction of a large number of vacancies would increase the energy of the crystal, and possibly induce transformation into a more stable phase.

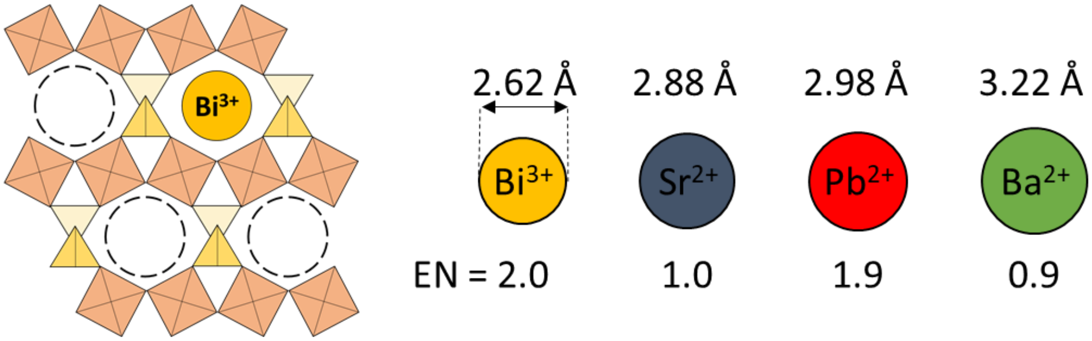

Figure 7-2. Possible substitutional multivalent cations and their respective ionic diameters and electronegativities.

Another potential research avenue for jarosite materials would be their conversion to more favorable, higher energy density iron-sulfate and iron-phosphate materials. For example, $LiFePO_4$ was produced via the carbothermal reduction of ammonium jarosite extracted from vanadium slag as an inexpensive iron source.[145] Other reduction methods could be investigated using jarosite as a source material. A disadvantage of many iron sulfate and phosphate materials is that they require a non-aqueous synthesis process. These materials also suffer from poor diffusion kinetics and conductivity which could be mitigated by the formation of nanostructures. Possibly jarosite precursor material could be synthesized as a nanostructure then converted into other iron sulfate or phosphate compounds but retain the original nanostructure.

Varying chemical composition of hexacyanoferrate compounds through cation doping and substitution has continued potential for investigation. Recently, multi-cation in Prussian blue analogs has gathered attention.[68] The combination of multiple cation species may have a synergistic effect on electrochemical performance. For example, partial Ni and Fe substitution in MnHCF displayed reduced Jahn-Teller distortion and increased cyclic stability.[146] Other combinations of different cation substitutes and their effect on electrochemistry of FeHCF have yet to be studied.

Bibliography

(1) Panos, E.; Densing, M.; Volkart, K. Access to Electricity in the World Energy Council's Global Energy Scenarios: An Outlook for Developing Regions until 2030. *Energy Strateg. Rev.* **2016**. https://doi.org/10.1016/j.esr.2015.11.003.

(2) Ritchie, Hannah; Roser, M. Energy - Our World in Data. *OurWorldInData.org*. 2020.

(3) BP. Statistical Review of World Energy, 2020 | 69th Edition. *Bp* **2020**.

(4) Landrigan, P. J.; Fuller, R.; Acosta, N. J. R.; Adeyi, O.; Arnold, R.; Basu, N. (Nil); Baldé, A. B.; Bertollini, R.; Bose-O'Reilly, S.; Boufford, J. I.; Breysse, P. N.; Chiles, T.; Mahidol, C.; Coll-Seck, A. M.; Cropper, M. L.; Fobil, J.; Fuster, V.; Greenstone, M.; Haines, A.; Hanrahan, D.; Hunter, D.; Khare, M.; Krupnick, A.; Lanphear, B.; Lohani, B.; Martin, K.; Mathiasen, K. V.; McTeer, M. A.; Murray, C. J. L.; Ndahimananjara, J. D.; Perera, F.; Potočnik, J.; Preker, A. S.; Ramesh, J.; Rockström, J.; Salinas, C.; Samson, L. D.; Sandilya, K.; Sly, P. D.; Smith, K. R.; Steiner, A.; Stewart, R. B.; Suk, W. A.; van Schayck, O. C. P.; Yadama, G. N.; Yumkella, K.; Zhong, M. The Lancet Commission on Pollution and Health. *The Lancet*. 2018. https://doi.org/10.1016/S0140-6736(17)32345-0.

(5) Lelieveld, J.; Klingmüller, K.; Pozzer, A.; Burnett, R. T.; Haines, A.; Ramanathan, V. Effects of Fossil Fuel and Total Anthropogenic Emission Removal on Public Health and Climate. *Proc. Natl. Acad. Sci. U. S. A.* **2019**. https://doi.org/10.1073/pnas.1819989116.

(6) Dlugokenky, E.; Tans, P. Trends in Atmospheric Carbon Dioxide www.esrl.noaa.gov/gmd/ccgg/trends/ (accessed Nov 16, 2020).

(7) Lacis, A. A.; Schmidt, G. A.; Rind, D.; Ruedy, R. A. Atmospheric CO2: Principal Control Knob Governing Earth's Temperature. *Science (80-.).* **2010**. https://doi.org/10.1126/science.1190653.

(8) Field, C.B., Barros, V.R., Dokken, D.J., Mach, K.J., Mastrandrea, M.D., Bilir, T.E., Chatterjee, M., Ebi, K.L., Estrada, Y. O., Genova, R.C., Girma, B., Kissel, E.S., Levy, A.N., MacCracken, S., Mastrandrea, P.R., White, L. L. Climate Change 2014: Impacts, Adaptation, and Vulnerability. Part A: Global and Sectoral Aspects. *Ipcc* **2014**.

(9) *Global EV Outlook 2020*; 2020. https://doi.org/10.1787/d394399e-en.

(10) Ahmed, S.; Nelson, P. A.; Gallagher, K. G.; Susarla, N.; Dees, D. W. Cost and Energy Demand of Producing Nickel Manganese Cobalt Cathode Material for Lithium Ion Batteries. *J. Power Sources* **2017**. https://doi.org/10.1016/j.jpowsour.2016.12.069.

(11) Goodenough, J. B.; Park, K. S. The Li-Ion Rechargeable Battery: A Perspective. *J. Am. Chem. Soc.* **2013**, *135* (4), 1167–1176. https://doi.org/10.1021/ja3091438.

(12) Bard, A. J.; Faulkner, L. R. *Electrochemical Methods Fundamentals of Electrochemistry*; 2001.

(13) Peljo, P.; Girault, H. H. Electrochemical Potential Window of Battery Electrolytes: The HOMO-LUMO Misconception. *Energy Environ. Sci.* **2018**, *11* (9), 2306–2309.

https://doi.org/10.1039/c8ee01286e.

(14) Chen, W.; Ambrosio, F.; Miceli, G.; Pasquarello, A. Ab Initio Electronic Structure of Liquid Water. *Phys. Rev. Lett.* **2016**. https://doi.org/10.1103/PhysRevLett.117.186401.

(15) Méndez-Hernández, D. D.; Gillmore, J. G.; Montano, L. A.; Gust, D.; Moore, T. A.; Moore, A. L.; Mujica, V. Building and Testing Correlations for the Estimation of One-Electron Reduction Potentials of a Diverse Set of Organic Molecules. *J. Phys. Org. Chem.* **2015**. https://doi.org/10.1002/poc.3413.

(16) Whittingham, M. S. Chemistry of Intercalation Compounds: Metal Guests in Chalcogenide Hosts. *Progress in Solid State Chemistry*. 1978. https://doi.org/10.1016/0079-6786(78)90003-1.

(17) Ferraresi, G.; Villevieille, C.; Czekaj, I.; Horisberger, M.; Novák, P.; El Kazzi, M. SnO2 Model Electrode Cycled in Li-Ion Battery Reveals the Formation of Li2SnO3 and Li8SnO6 Phases through Conversion Reactions. *ACS Appl. Mater. Interfaces* **2018**. https://doi.org/10.1021/acsami.7b19481.

(18) Haynes, W. M. ABUNDANCE OF ELEMENTS IN THE EARTH’S CRUST AND IN THE SEA. In *CRC Handbook of Chemistry and Physics, 97th edition*; 2016; pp 14–17.

(19) National Minerals Information Center https://www.usgs.gov/centers/nmic/commodity-statistics-and-information (accessed Nov 17, 2020).

(20) *CRC Handbook of Chemistry and Physics, 93rd Edition*; 2016. https://doi.org/10.1201/b12286.

(21) Gong, K.; Xu, F.; Grunewald, J. B.; Ma, X.; Zhao, Y.; Gu, S.; Yan, Y. All-Soluble All-Iron Aqueous Redox-Flow Battery. *ACS Energy Lett.* **2016**. https://doi.org/10.1021/acsenergylett.6b00049.

(22) Li, J.; Li, J.; Luo, J.; Wang, L.; He, X. Recent Advances in the LiFeO2-Based Materials for Li-Ion Batteries. *International Journal of Electrochemical Science*. 2011.

(23) Lee, Y. S.; Sato, S.; Sun, Y. K.; Kobayakawa, K.; Sato, Y. A New Type of Orthorhombic LiFeO2 with Advanced Battery Performance and Its Structural Change during Cycling. In *Journal of Power Sources*; 2003. https://doi.org/10.1016/S0378-7753(03)00152-6.

(24) Tabuchi, M.; Nakashima, A.; Shigemura, H.; Ado, K.; Kobayashi, H.; Sakaebe, H.; Tatsumi, K.; Kageyama, H.; Nakamura, T.; Kanno, R. Fine Li(4 - x)/3Ti(2 - 2x)/3FexO2 (0.18 ≤ x < 0.67) Powder with Cubic Rock-Salt Structure as a Positive Electrode Material for Rechargeable Lithium Batteries. *J. Mater. Chem.* **2003**. https://doi.org/10.1039/b209569f.

(25) Bordet-Le Guenne, L.; Deniard, P.; Lecerf, A.; Biensan, P.; Siret, C.; Fournès, L.; Brec, R. Intrinsic Instability of Fe4+ in Electrochemically Oxidized Ramsdellite and Orthorhombic Li(1-x)H(x)FeO2. *J. Mater. Chem.* **1999**. https://doi.org/10.1039/a809947b.

(26) Barpanda, P. Pursuit of Sustainable Iron-Based Sodium Battery Cathodes: Two Case Studies. *Chemistry of Materials*. 2016. https://doi.org/10.1021/acs.chemmater.5b03926.

(27) Delmas, C.; Fouassier, C.; Hagenmuller, P. Structural Classification and Properties of the Layered Oxides. *Phys. B+C* **1980**. https://doi.org/10.1016/0378-4363(80)90214-4.

(28) Zhao, J.; Zhao, L.; Dimov, N.; Okada, S.; Nishida, T. Electrochemical and Thermal Properties of α-NaFeO 2 Cathode for Na-Ion Batteries . *J. Electrochem. Soc.* **2013**. https://doi.org/10.1149/2.007305jes.

(29) Yabuuchi, N.; Yoshida, H.; Komaba, S. Crystal Structures and Electrode Performance of Alpha-NaFeO2 for Rechargeable Sodium Batteries. *Electrochemistry* **2012**. https://doi.org/10.5796/electrochemistry.80.716.

(30) Su, Q.; Xie, D.; Zhang, J.; Du, G.; Xu, B. In Situ Transmission Electron Microscopy Observation of the Conversion Mechanism of Fe2O3/Graphene Anode during Lithiation-Delithiation Processes. *ACS Nano* **2013**. https://doi.org/10.1021/nn403720p.

(31) Li, J.; Hwang, S.; Guo, F.; Li, S.; Chen, Z.; Kou, R.; Sun, K.; Sun, C. J.; Gan, H.; Yu, A.; Stach, E. A.; Zhou, H.; Su, D. Phase Evolution of Conversion-Type Electrode for Lithium Ion Batteries. *Nat. Commun.* **2019**. https://doi.org/10.1038/s41467-019-09931-2.

(32) Zhang, L.; Wu, H. Bin; Lou, X. W. Iron-Oxide-Based Advanced Anode Materials for Lithium-Ion Batteries. *Adv. Energy Mater.* **2014**. https://doi.org/10.1002/aenm.201300958.

(33) Zhao, J.; Zhang, Y.; Wang, Y.; Li, H.; Peng, Y. The Application of Nanostructured Transition Metal Sulfides as Anodes for Lithium Ion Batteries. *Journal of Energy Chemistry*. 2018. https://doi.org/10.1016/j.jechem.2018.01.009.

(34) Yu, X. Y.; Yu, L.; Lou, X. W. Metal Sulfide Hollow Nanostructures for Electrochemical Energy Storage. *Adv. Energy Mater.* **2016**. https://doi.org/10.1002/aenm.201501333.

(35) Xu, Q. T.; Li, J. C.; Xue, H. G.; Guo, S. P. Binary Iron Sulfides as Anode Materials for Rechargeable Batteries: Crystal Structures, Syntheses, and Electrochemical Performance. *Journal of Power Sources*. 2018. https://doi.org/10.1016/j.jpowsour.2018.01.022.

(36) Zou, J.; Zhao, J.; Wang, B.; Chen, S.; Chen, P.; Ran, Q.; Li, L.; Wang, X.; Yao, J.; Li, H.; Huang, J.; Niu, X.; Wang, L. Unraveling the Reaction Mechanism of FeS2 as a Li-Ion Battery Cathode. *ACS Appl. Mater. Interfaces* **2020**. https://doi.org/10.1021/acsami.0c14082.

(37) Zhang, S. S. The Redox Mechanism of FeS2 in Non-Aqueous Electrolytes for Lithium and Sodium Batteries. *Journal of Materials Chemistry A*. 2015. https://doi.org/10.1039/c5ta00623f.

(38) H. W. Jones, C.; E. Kovacs, P.; D. Sharma, R.; S. McMillan, R. An Iron-57 Moessbauer Study of the Intermediates Formed in the Reduction of Iron Disulfide in the Lithium/Iron Disulfide Battery System. *J. Phys. Chem.* **2002**, *95* (2), 774–779. https://doi.org/10.1021/j100155a053.

(39) Conte, D. E.; Pinna, N. A Review on the Application of Iron(III) Fluorides as Positive Electrodes for Secondary Cells. *Mater. Renew. Sustain. Energy* **2014**. https://doi.org/10.1007/s40243-014-0037-2.

(40) Murugesan, V.; Cho, J. S.; Govind, N.; Andersen, A.; Olszta, M. J.; Han, K. S.; Li, G.; Lee, H.; Reed, D. M.; Sprenkle, V. L.; Cho, S.; Nune, S. K.; Choi, D. Lithium Insertion Mechanism in Iron Fluoride Nanoparticles Prepared by Catalytic Decomposition of Fluoropolymer. *ACS Appl. Energy Mater.* **2019**. https://doi.org/10.1021/acsaem.8b01983.

(41) Shi, Y. L.; Wu, N.; Shen, M. F.; Cui, Y. L.; Jiang, L.; Qiang, Y. H.; Zhuang, Q. C. Electrochemical Behavior of Iron(III) Fluoride Trihydrate as a Cathode in Lithium-Ion Batteries. *ChemElectroChem* **2014**. https://doi.org/10.1002/celc.201300069.

(42) Ali, G.; Lee, J. H.; Chang, W.; Cho, B. W.; Jung, H. G.; Nam, K. W.; Chung, K. Y. Lithium Intercalation Mechanism into FeF3·0.5H2O as a Highly Stable Composite Cathode Material. *Sci. Rep.* **2017**. https://doi.org/10.1038/srep42237.

(43) Kuznetsov, D. A.; Han, B.; Yu, Y.; Rao, R. R.; Hwang, J.; Román-Leshkov, Y.; Shao-Horn, Y. Tuning Redox Transitions via Inductive Effect in Metal Oxides and Complexes, and Implications in Oxygen Electrocatalysis. *Joule*. 2018. https://doi.org/10.1016/j.joule.2017.11.014.

(44) Hu, J.; Huang, W.; Yang, L.; Pan, F. Structure and Performance of the LiFePO4cathode Material: From the Bulk to the Surface. *Nanoscale*. 2020. https://doi.org/10.1039/d0nr03776a.

(45) Delacourt, C.; Laffont, L.; Bouchet, R.; Wurm, C.; Leriche, J.-B.; Morcrette, M.; Tarascon, J.-M.; Masquelier, C. Toward Understanding of Electrical Limitations (Electronic, Ionic) in LiMPO[Sub 4] (M=Fe, Mn) Electrode Materials. *J. Electrochem. Soc.* **2005**. https://doi.org/10.1149/1.1884787.

(46) Wolfenstine, J.; Allen, J. Ni3+/Ni2+ Redox Potential in LiNiPO4. *Journal of Power Sources*. 2005. https://doi.org/10.1016/j.jpowsour.2004.11.024.

(47) Zhang, M.; Garcia-Araez, N.; Hector, A. L. Understanding and Development of Olivine LiCoPO4 Cathode Materials for Lithium-Ion Batteries. *Journal of Materials Chemistry A*. 2018. https://doi.org/10.1039/c8ta04063j.

(48) Wang, J.; Sun, X. Understanding and Recent Development of Carbon Coating on LiFePO 4 Cathode Materials for Lithium-Ion Batteries. *Energy and Environmental Science*. 2012. https://doi.org/10.1039/c1ee01263k.

(49) Lee, S.; Park, S. S. Comparative Study of Tavorite and Triplite LiFeSO4F as Cathode Materials for Lithium Ion Batteries: Structure, Defect Chemistry, and Lithium Conduction Properties from Atomistic Simulation. *J. Phys. Chem. C* **2014**. https://doi.org/10.1021/jp502672k.

(50) Barpanda, P.; Ati, M.; Melot, B. C.; Rousse, G.; Chotard, J. N.; Doublet, M. L.; Sougrati, M. T.; Corr, S. A.; Jumas, J. C.; Tarascon, J. M. A 3.90 v Iron-Based Fluorosulphate Material for Lithium-Ion Batteries Crystallizing in the Triplite Structure. *Nat. Mater.* **2011**. https://doi.org/10.1038/nmat3093.

(51) Ben Yahia, M.; Lemoigno, F.; Rousse, G.; Boucher, F.; Tarascon, J. M.; Doublet, M. L. Origin of the 3.6 v to 3.9 v Voltage Increase in the LiFeSO 4F Cathodes for Li-Ion Batteries. *Energy Environ. Sci.* **2012**. https://doi.org/10.1039/c2ee22699e.

(52) Yamada, A.; Lwane, N.; Harada, Y.; Nishimura, S. I.; Koyama, Y.; Tanaka, L. Lithium Iron Borates as High-Capacity Battery Electrodes. *Adv. Mater.* **2010**. https://doi.org/10.1002/adma.201001039.

(53) Nytén, A.; Abouimrane, A.; Armand, M.; Gustafsson, T.; Thomas, J. O. Electrochemical Performance of Li2FeSiO4 as a New Li-Battery Cathode Material. *Electrochem. commun.* **2005**, *7* (2), 156–160. https://doi.org/10.1016/j.elecom.2004.11.008.

(54) Yao, W.; Armstrong, A. R.; Zhou, X.; Sougrati, M. T.; Kidkhunthod, P.; Tunmee, S.; Sun, C.; Sattayaporn, S.; Lightfoot, P.; Ji, B.; Jiang, C.; Wu, N.; Tang, Y.; Cheng, H. M. An Oxalate Cathode for Lithium Ion Batteries with Combined Cationic and Polyanionic Redox. *Nat. Commun.* **2019**. https://doi.org/10.1038/s41467-019-11077-0.

(55) Gnanavel, M.; Pralong, V.; Lebedev, O. I.; Caignaert, V.; Bazin, P.; Raveau, B. Lithium Intercalation into the Jarosite-Type Hydroxysulfate: A Topotactic Reversible Reaction from a Crystalline Phase to an Inorganic Polymer-like Structure. *Chem. Mater.* **2014**, *26* (15), 4521–4527. https://doi.org/10.1021/cm501735t.

(56) Nishimura, S. I.; Nakamura, M.; Natsui, R.; Yamada, A. New Lithium Iron Pyrophosphate as 3.5 v Class Cathode Material for Lithium Ion Battery. *J. Am. Chem. Soc.* **2010**. https://doi.org/10.1021/ja106297a.

(57) Plewa, A.; Kulka, A.; Baster, D.; Molenda, J. An Alluaudite Compounds Na 2 Fe 2 (SO 4) 3 vs. Na 2.5 Fe 1.75 (SO 4) 3 as Earth Abundant Cathode Materials for Na-Ion Batteries. *Solid State Ionics* **2019**. https://doi.org/10.1016/j.ssi.2019.02.007.

(58) Barpanda, P.; Ye, T.; Nishimura, S. I.; Chung, S. C.; Yamada, Y.; Okubo, M.; Zhou, H.; Yamada, A. Sodium Iron Pyrophosphate: A Novel 3.0 v Iron-Based Cathode for Sodium-Ion Batteries. *Electrochem. commun.* **2012**. https://doi.org/10.1016/j.elecom.2012.08.028.

(59) Wang, W.; Wang, S.; Jiao, H.; Zhan, P.; Jiao, S. A Sodium Ion Intercalation Material: A Comparative Study of Amorphous and Crystalline FePO4. *Phys. Chem. Chem. Phys.* **2015**. https://doi.org/10.1039/c4cp05764c.

(60) Xu, Y.; Zheng, S.; Tang, H.; Guo, X.; Xue, H.; Pang, H. Prussian Blue and Its Derivatives as Electrode Materials for Electrochemical Energy Storage. *Energy Storage Mater.* **2017**, *9* (June), 11–30. https://doi.org/10.1016/j.ensm.2017.06.002.

(61) Zakaria, M. B.; Chikyow, T. Recent Advances in Prussian Blue and Prussian Blue Analogues: Synthesis and Thermal Treatments. *Coord. Chem. Rev.* **2017**, *352*, 328–345. https://doi.org/10.1016/j.ccr.2017.09.014.

(62) Gautam, M.; Poudel, K.; Yong, C. S.; Kim, J. O. Prussian Blue Nanoparticles: Synthesis, Surface Modification, and Application in Cancer Treatment. *Int. J. Pharm.* **2018**, *549* (1–2), 31–49. https://doi.org/10.1016/j.ijpharm.2018.07.055.

(63) Yang, H. M.; Hwang, J. R.; Lee, D. Y.; Kim, K. B.; Park, C. W.; Kim, H. R.; Lee, K. W. Eco-Friendly One-Pot Synthesis of Prussian Blue-Embedded Magnetic Hydrogel Beads for the Removal of Cesium from Water. *Sci. Rep.* **2018**, *8* (1), 1–10. https://doi.org/10.1038/s41598-018-29767-y.

(64) Hedley, L.; Porteous, L.; Hutson, D.; Robertson, N.; Johansson, J. O. Electrochromic

Bilayers of Prussian Blue and Its Cr Analogue. *J. Mater. Chem. C* **2018**, *6* (3), 512–517. https://doi.org/10.1039/c7tc04521b.

(65) Zeng, Y.; Chen, G. F.; Jiang, Z.; Ding, L. X.; Wang, S.; Wang, H. Confined Heat Treatment of a Prussian Blue Analogue for Enhanced Electrocatalytic Oxygen Evolution. *J. Mater. Chem. A* **2018**, *6* (33), 15942–15946. https://doi.org/10.1039/c8ta05677c.

(66) Zhang, Y.; Huang, B.; Yu, F.; Yuan, Q.; Gu, M.; Ji, J.; Zhang, Y.; Li, Y. 3D Nitrogen-Doped Graphite Foam@Prussian Blue: An Electrochemical Sensing Platform for Highly Sensitive Determination of H2O2 and Glucose. *Microchim. Acta* **2018**, *185* (2). https://doi.org/10.1007/s00604-017-2631-3.

(67) Patra, C. R. Prussian Blue Nanoparticles and Their Analogues for Application to Cancer Theranostics. *Nanomedicine*. 2016. https://doi.org/10.2217/nnm.16.16.

(68) Wang, B.; Han, Y.; Wang, X.; Bahlawane, N.; Pan, H.; Yan, M.; Jiang, Y. Prussian Blue Analogs for Rechargeable Batteries. *iScience* **2018**, *3*, 110–133. https://doi.org/10.1016/j.isci.2018.04.008.

(69) Kumar, A.; Yusuf, S. M.; Keller, L. Structural and Magnetic Properties of Fe[Fe(CN) 6]·4H 2O. *Phys. Rev. B - Condens. Matter Mater. Phys.* **2005**, *71* (5), 1–7. https://doi.org/10.1103/PhysRevB.71.054414.

(70) Lu, Y.; Wang, L.; Cheng, J.; Goodenough, J. B. Prussian Blue: A New Framework of Electrode Materials for Sodium Batteries. *Chem. Commun.* **2012**, *48* (52), 6544–6546. https://doi.org/10.1039/c2cc31777j.

(71) Rudola, A.; Du, K.; Balaya, P. Monoclinic Sodium Iron Hexacyanoferrate Cathode and Non-Flammable Glyme-Based Electrolyte for Inexpensive Sodium-Ion Batteries. *J. Electrochem. Soc.* **2017**, *164* (6), A1098–A1109. https://doi.org/10.1149/2.0701706jes.

(72) Bueno, P. R.; Ferreira, F. F.; Giménez-Romero, D.; Setti, G. O.; Faria, R. C.; Gabrielli, C.; Perrot, H.; Garcia-Jareño, J. J.; Vicente, F. Synchrotron Structural Characterization of Electrochemically Synthesized Hexacyanoferrates Containing K+: A Revisited Analysis of Electrochemical Redox. *J. Phys. Chem. C* **2008**, *112* (34), 13264–13271. https://doi.org/10.1021/jp802070f.

(73) You, Y.; Yu, X.; Yin, Y.; Nam, K. W.; Guo, Y. G. Sodium Iron Hexacyanoferrate with High Na Content as a Na-Rich Cathode Material for Na-Ion Batteries. *Nano Res.* **2014**, *8* (1), 117–128. https://doi.org/10.1007/s12274-014-0588-7.

(74) You, Y.; Wu, X. L.; Yin, Y. X.; Guo, Y. G. High-Quality Prussian Blue Crystals as Superior Cathode Materials for Room-Temperature Sodium-Ion Batteries. *Energy Environ. Sci.* **2014**, *7* (5), 1643–1647. https://doi.org/10.1039/c3ee44004d.

(75) Liu, Y.; Qiao, Y.; Zhang, W.; Li, Z.; Ji, X.; Miao, L.; Yuan, L.; Hu, X.; Huang, Y. Sodium Storage in Na-Rich NaxFeFe(CN)6 Nanocubes. *Nano Energy* **2015**, *12*, 386?393-393. https://doi.org/10.1016/j.nanoen.2015.01.012.

(76) Li, L.; Nie, P.; Chen, Y.; Wang, J. Novel Acetic Acid Induced Na-Rich Prussian Blue Nanocubes with Iron Defects as Cathodes for Sodium Ion Batteries. *J. Mater. Chem. A* **2019**, *7* (19), 12134–12144. https://doi.org/10.1039/c9ta01965k.

(77) Fu, H.; Liu, C.; Zhang, C.; Ma, W.; Wang, K.; Li, Z.; Lu, X.; Cao, G. Enhanced Storage of Sodium Ions in Prussian Blue Cathode Material through Nickel Doping. *J. Mater. Chem. A* **2017**, *5* (20), 9604–9610. https://doi.org/10.1039/c7ta00132k.

(78) Soloveichik, G. L. Flow Batteries: Current Status and Trends. *Chemical Reviews*. 2015. https://doi.org/10.1021/cr500720t.

(79) Hruska, L. W.; Savinell, R. F. Investigation of Factors Affecting Performance of the Iron-Redox Battery. *J. Electrochem. Soc.* **1981**. https://doi.org/10.1149/1.2127366.

(80) Wen, Y. H.; Zhang, H. M.; Qian, P.; Zhou, H. T.; Zhao, P.; Yi, B. L.; Yang, Y. S. Studies on Iron (Fe[Sup 3+]∕Fe[Sup 2+])-Complex/Bromine (Br[Sub 2]∕Br[Sup −]) Redox Flow Cell in Sodium Acetate Solution. *J. Electrochem. Soc.* **2006**. https://doi.org/10.1149/1.2186040.

(81) Dutrizac, J. E.; Jambor, J. L. Jarosites and Their Application in Hydrometallurgy. *Sulfate Miner. Crystallogr. Geochemistry, Environ. Significance* **2019**, *40*, 405–452. https://doi.org/10.2138/rmg.2000.40.8.

(82) Karamanov, A.; Taglieri, G.; Pelino, M. Iron-Rich Sintered Glass-Ceramics from Industrial Wastes. *J. Am. Ceram. Soc.* **1999**. https://doi.org/10.1111/j.1151-2916.1999.tb02195.x.

(83) Patrick Mubiayi, M.; Elizabeth Makhatha, M.; Titilayo Akinlabi, E. Characterization, Leachate Characteristics and Compressive Strength of Jarosite/Clay/Fly Ash Bricks. In *Materials Today: Proceedings*; 2018. https://doi.org/10.1016/j.matpr.2018.06.105.

(84) Asokan, P.; Saxena, M.; Asolekar, S. R. Hazardous Jarosite Use in Developing Non-Hazardous Product for Engineering Application. *J. Hazard. Mater.* **2006**. https://doi.org/10.1016/j.jhazmat.2006.04.054.

(85) Szymanski, J. T. The Crystal Structure of Plumbojarosite Pb[Fe3(SO4)2(OH)6]2. *Can. Mineral.* **1985**, *23*, 659–668.

(86) Gnanavel, M.; Lebedev, O. I.; Bazin, P.; Raveau, B.; Pralong, V. Reversible Transformation from Amorphouse Na3Fe3(SO4)2(OH)6 to Crystallized NaFe3(SO4)2(OH)6 Jarosite-Type Hydroxysulfate. *Solid State Ionics* **2015**, *278*, 38–42. https://doi.org/10.1016/j.ssi.2015.05.013.

(87) Ding, Y. L.; Wen, Y.; Van Aken, P. A.; Maier, J.; Yu, Y. Jarosite Nanosheets Fabricated via Room-Temperature Synthesis as Cathode Materials for High-Rate Lithium Ion Batteries. *Chem. Mater.* **2015**, *27* (8), 3143–3149. https://doi.org/10.1021/acs.chemmater.5b00849.

(88) Xu, W.; Xie, Z.; Cui, X.; Zhao, K.; Zhang, L.; Mai, L.; Wang, Y. Direct Growth of an Economic Green Energy Storage Material: A Monocrystalline Jarosite-KFe3(SO4)2(OH)6-Nanoplates@rGO Hybrid as a Superior Lithium-Ion Battery Cathode. *J. Mater. Chem. A* **2016**. https://doi.org/10.1039/c5ta10622b.

(89) Sandineni, P.; Yaghoobnejad Asl, H.; Choudhury, A. Kagomé Lattices as Cathode: Effect of Particle Size and Fluoride Substitution on Electrochemical Lithium Insertion in Sodium- and Ammonium Jarosites. *J. Solid State Chem.* **2016**.

https://doi.org/10.1016/j.jssc.2016.02.022.

(90) Dutrizac, J. E. Factors Affecting Alkali Jarosite Precipitation. *Metall. Trans. B* **1983**. https://doi.org/10.1007/BF02653939.

(91) Dutrizac, J. E.; Dinardo, O.; Kaiman, S. Factors Affecting Lead Jarosite Formation. *Hydrometallurgy* **1980**. https://doi.org/10.1016/0304-386X(80)90022-5.

(92) Basciano, L. C.; Peterson, R. C. Jarosite-Hydronium Jarosite Solid-Solution Series with Full Iron Site Occupancy: Mineralogy and Crystal Chemistry. *Am. Mineral.* **2007**. https://doi.org/10.2138/am.2007.2432.

(93) Jambor, J. L.; Dutrizac, J. L. The Synthesis of Beaverite. *Can. Mineral.* **1985**, *23*, 47–51. https://doi.org/10.1002/9780470187326.ch2.

(94) Fleischer, M.; Wilcox, R. E.; Matzko, J. J. MICROSCOPIC DETERMINATION OF THE NONOPAQUE MINERALS. *US Geol. Surv. Bull.* **1984**.

(95) Gutierrez, A.; Benedek, N. A.; Manthiram, A. Crystal-Chemical Guide for Understanding Redox Energy Variations of M 2+/3+ Couples in Polyanion Cathodes for Lithium-Ion Batteries. *Chem. Mater.* **2013**, *25* (20), 4010–4016. https://doi.org/10.1021/cm401949n.

(96) Uchaker, E.; Zheng, Y. Z.; Li, S.; Candelaria, S. L.; Hu, S.; Cao, G. Z. Better than Crystalline: Amorphous Vanadium Oxide for Sodium-Ion Batteries. *J. Mater. Chem. A* **2014**, *2* (43), 18208–18214. https://doi.org/10.1039/c4ta03788j.

(97) Shannon, R. D. Revised Effective Ionic Radii and Systematic Studies of Interatomic Distances in Halides and Chalcogenides. *Acta Crystallogr. Sect. A* **1976**. https://doi.org/10.1107/S0567739476001551.

(98) Ho, C. Application of A-C Techniques to the Study of Lithium Diffusion in Tungsten Trioxide Thin Films. *J. Electrochem. Soc.* **1980**, *127* (2), 343. https://doi.org/10.1149/1.2129668.

(99) Vorotyntsev, M. A.; Levi, M. D.; Aurbach, D. Spatially Limited Diffusion Coupled with Ohmic Potential Drop and/or Slow Interfacial Exchange: A New Method to Determine the Diffusion Time Constant and External Resistance from Potential Step (PITT) Experiments. *J. Electroanal. Chem.* **2004**. https://doi.org/10.1016/j.jelechem.2003.12.014.

(100) Lee, J.; Urban, A.; Li, X.; Su, D.; Hautier, G.; Ceder, G. Unlocking the Potential of Cation-Disordered Oxides for Rechargeable Lithium Batteries. *Science (80-.).* **2014**, *343* (6170), 519–522. https://doi.org/10.1126/science.1246432.

(101) Ghosh, R. S.; Dzombak, D. A.; Luthy, R. G. Equilibrium Precipitation and Dissolution of Iron Cyanide Solids in Water. *Environ. Eng. Sci.* **1999**. https://doi.org/10.1089/ees.1999.16.293.

(102) Cai, D.; Yang, X.; Qu, B.; Wang, T. Comparison of the Electrochemical Performance of Iron Hexacyanoferrate with High and Low Quality as Cathode Materials for Aqueous Sodium-Ion Batteries. *Chem. Commun.* **2017**, *53* (50), 6780–6783. https://doi.org/10.1039/c7cc02516e.

(103) Chen, R.; Huang, Y.; Xie, M.; Wang, Z.; Ye, Y.; Li, L.; Wu, F. Chemical Inhibition Method to Synthesize Highly Crystalline Prussian Blue Analogs for Sodium-Ion Battery Cathodes. *ACS Appl. Mater. Interfaces* **2016**, *8* (46), 31669–31676. https://doi.org/10.1021/acsami.6b10884.

(104) Shiba, F.; Fujishiro, R.; Kojima, T.; Okawa, Y. Preparation of Monodisperse Cobalt(II) Hexacyanoferrate(III) Nanoparticles Using Cobalt Ions Released from a Citrate Complex. *J. Phys. Chem. C* **2012**, *116* (5), 3394–3399. https://doi.org/10.1021/jp210707y.

(105) Martell, A. E.; Motekaitis, R. J.; Chen, D.; Hancock, R. D.; McManus, D. Selection of New Fe(III)/Fe(II) Chelating Agents as Catalysts for the Oxidation of Hydrogen Sulfide to Sulfur by Air. *Can. J. Chem.* **1996**. https://doi.org/10.1139/v96-210.

(106) Aparicio, C.; Machala, L.; Marusak, Z. Thermal Decomposition of Prussian Blue under Inert Atmosphere. *J. Therm. Anal. Calorim.* **2012**, *110* (2), 661–669. https://doi.org/10.1007/s10973-011-1890-1.

(107) Grandjean, F.; Samain, L.; Long, G. J. Characterization and Utilization of Prussian Blue and Its Pigments. *Dalt. Trans.* **2016**, *45* (45), 18018–18044. https://doi.org/10.1039/c6dt03351b.

(108) Samain, L.; Grandjean, F.; Long, G. J.; Martinetto, P.; Bordet, P.; Strivay, D. Relationship between the Synthesis of Prussian Blue Pigments, Their Color, Physical Properties, and Their Behavior in Paint Layers. *J. Phys. Chem. C* **2013**, *117* (19), 9693–9712. https://doi.org/10.1021/jp3111327.

(109) De Tacconi, N. R.; Rajeshwar, K.; Lezna, R. O. Metal Hexacyanoferrates: Electrosynthesis, in Situ Characterization, and Applications. *Chem. Mater.* **2003**, *15* (16), 3046–3062. https://doi.org/10.1021/cm0341540.

(110) Stevens, J. G.; Travis, J. C.; DeVoe, J. R. Mössbauer Spectrometry. *Anal. Chem.* **1972**, *44* (5), 384–406. https://doi.org/10.1021/ac60313a003.

(111) Wang, L.; Song, J.; Qiao, R.; Wray, L. A.; Hossain, M. A.; Chuang, Y. De; Yang, W.; Lu, Y.; Evans, D.; Lee, J. J.; Vail, S.; Zhao, X.; Nishijima, M.; Kakimoto, S.; Goodenough, J. B. Rhombohedral Prussian White as Cathode for Rechargeable Sodium-Ion Batteries. *J. Am. Chem. Soc.* **2015**, *137* (7), 2548–2554. https://doi.org/10.1021/ja510347s.

(112) Ling, C.; Chen, J.; Mizuno, F. First-Principles Study of Alkali and Alkaline Earth Ion Intercalation in Iron Hexacyanoferrate: The Important Role of Ionic Radius. *J. Phys. Chem. C* **2013**, *117* (41), 21158–21165. https://doi.org/10.1021/jp4078689.

(113) Huang, Y.; Xie, M.; Zhang, J.; Wang, Z.; Jiang, Y.; Xiao, G.; Li, S.; Li, L.; Wu, F.; Chen, R. A Novel Border-Rich Prussian Blue Synthetized by Inhibitor Control as Cathode for Sodium Ion Batteries. *Nano Energy* **2017**, *39* (May), 273–283. https://doi.org/10.1016/j.nanoen.2017.07.005.

(114) Wu, X.; Deng, W.; Qian, J.; Cao, Y.; Ai, X.; Yang, H. Single-Crystal FeFe(CN)6 Nanoparticles: A High Capacity and High Rate Cathode for Na-Ion Batteries. *J. Mater. Chem. A* **2013**, *1* (35), 10130–10134. https://doi.org/10.1039/c3ta12036h.

(115) Jiang, Y.; Yu, S.; Wang, B.; Li, Y.; Sun, W.; Lu, Y.; Yan, M.; Song, B.; Dou, S. Prussian

Blue@C Composite as an Ultrahigh-Rate and Long-Life Sodium-Ion Battery Cathode. *Adv. Funct. Mater.* **2016**, *26* (29), 5315–5321. https://doi.org/10.1002/adfm.201600747.

(116) Uchaker, E.; Cao, G. Mesocrystals as Electrode Materials for Lithium-Ion Batteries. *Nano Today*. 2014. https://doi.org/10.1016/j.nantod.2014.06.004.

(117) Sturm, E. V.; Cölfen, H. Mesocrystals: Structural and Morphogenetic Aspects. *Chemical Society Reviews*. 2016, pp 5821–5833. https://doi.org/10.1039/c6cs00208k.

(118) Liu, C.; Zhang, C.; Song, H.; Zhang, C.; Liu, Y.; Nan, X.; Cao, G. Mesocrystal MnO Cubes as Anode for Li-Ion Capacitors. *Nano Energy* **2016**. https://doi.org/10.1016/j.nanoen.2016.02.035.

(119) Hu, M.; Jiang, J. Sen; Lin, C. C.; Zeng, Y. Prussian Blue Mesocrystals: An Example of Self-Construction. *CrystEngComm* **2010**, *12* (10), 2679–2683. https://doi.org/10.1039/c003523h.

(120) Zheng, X. J.; Kuang, Q.; Xu, T.; Jiang, Z. Y.; Zhang, S. H.; Xie, Z. X.; Huang, R. B.; Zheng, L. S. Growth of Prussian Blue Microcubes under a Hydrothermal Condition: Possible Nonclassical Crystallization by a Mesoscale Self-Assembly. *J. Phys. Chem. C* **2007**, *111* (12), 4499–4502. https://doi.org/10.1021/jp065055n.

(121) Ming, H.; Torad, N. L. K.; Chiang, Y. D.; Wu, K. C. W.; Yamauchi, Y. Size- and Shape-Controlled Synthesis of Prussian Blue Nanoparticles by a Polyvinylpyrrolidone-Assisted Crystallization Process. *CrystEngComm* **2012**, *14* (10), 3387–3396. https://doi.org/10.1039/c2ce25040c.

(122) Chen, Q.; Jia, C.; Li, Y.; Xu, J.; Guan, B.; Yates, M. Z. α-Calcium Sulfate Hemihydrate Nanorods Synthesis: A Method for Nanoparticle Preparation by Mesocrystallization. *Langmuir* **2017**, *33* (9), 2362–2369. https://doi.org/10.1021/acs.langmuir.7b00013.

(123) Xie, R.; Feng, Z.; Li, S.; Xu, B. EDTA-Assisted Self-Assembly of Fluoride-Substituted Hydroxyapatite Coating on Enamel Substrate. *Cryst. Growth Des.* **2011**, *11* (12), 5206–5214. https://doi.org/10.1021/cg101708y.

(124) De Yoreo, J. J. Principles of Crystal Nucleation and Growth. *Rev. Mineral. Geochemistry* **2003**, *54* (1), 57–93. https://doi.org/10.2113/0540057.

(125) Dean, J. A. *Lange's Handbook Of Chemistry, 15th Ed.*; 1999.

(126) Greaves, T. L.; Cashion, J. D. Site Analysis and Calculation of the Quadrupole Splitting of Prussian Blue Mössbauer Spectra. *Hyperfine Interact.* **2016**, *237* (1), 1–9. https://doi.org/10.1007/s10751-016-1216-6.

(127) Guo, X.; Wang, Z.; Deng, Z.; Li, X.; Wang, B.; Chen, X.; Ong, S. P. Water Contributes to Higher Energy Density and Cycling Stability of Prussian Blue Analogue Cathodes for Aqueous Sodium-Ion Batteries. *Chem. Mater.* **2019**, *31* (15), 5933–5942. https://doi.org/10.1021/acs.chemmater.9b02269.

(128) Chen, L.; Shao, H.; Zhou, X.; Liu, G.; Jiang, J.; Liu, Z. Water-Mediated Cation Intercalation of Open-Framework Indium Hexacyanoferrate with High Voltage and Fast Kinetics. *Nat. Commun.* **2016**, *7* (May), 1–10. https://doi.org/10.1038/ncomms11982.

(129) Yang, Y.; Liu, E.; Yan, X.; Ma, C.; Wen, W.; Liao, X.-Z.; Ma, Z.-F. Influence of Structural Imperfection on Electrochemical Behavior of Prussian Blue Cathode Materials for Sodium Ion Batteries. *J. Electrochem. Soc.* **2016**, *163* (9), A2117–A2123. https://doi.org/10.1149/2.0031610jes.

(130) Pasta, M.; Wang, R. Y.; Ruffo, R.; Qiao, R.; Lee, H. W.; Shyam, B.; Guo, M.; Wang, Y.; Wray, L. A.; Yang, W.; Toney, M. F.; Cui, Y. Manganese-Cobalt Hexacyanoferrate Cathodes for Sodium-Ion Batteries. *J. Mater. Chem. A* **2016**, *4* (11), 4211–4223. https://doi.org/10.1039/c5ta10571d.

(131) Tang, Y.; Li, W.; Feng, P.; Zhou, M.; Wang, K.; Wang, Y.; Zaghib, K.; Jiang, K. High-Performance Manganese Hexacyanoferrate with Cubic Structure as Superior Cathode Material for Sodium-Ion Batteries. *Adv. Funct. Mater.* **2020**, *30* (10), 1–9. https://doi.org/10.1002/adfm.201908754.

(132) Li, J.; Liu, X.; Tan, L.; Cui, Z.; Yang, X.; Liang, Y.; Li, Z.; Zhu, S.; Zheng, Y.; Yeung, K. W. K.; Wang, X.; Wu, S. Zinc-Doped Prussian Blue Enhances Photothermal Clearance of Staphylococcus Aureus and Promotes Tissue Repair in Infected Wounds. *Nat. Commun.* **2019**, *10* (1). https://doi.org/10.1038/s41467-019-12429-6.

(133) Zhang, L.; Chen, L.; Zhou, X.; Liu, Z. Morphology-Dependent Electrochemical Performance of Zinc Hexacyanoferrate Cathode for Zinc-Ion Battery. *Sci. Rep.* **2015**, *5* (December), 1–11. https://doi.org/10.1038/srep18263.

(134) Jia, X.; Liu, C.; Neale, Z. G.; Yang, J.; Cao, G. Active Materials for Aqueous Zinc Ion Batteries: Synthesis, Crystal Structure, Morphology, and Electrochemistry. *Chemical Reviews*. 2020. https://doi.org/10.1021/acs.chemrev.9b00628.

(135) Hardwood, C. O. F.; Pulp, S. K.; Edta, W. Chelation of Hardwood and Softwood Kraft Pulp. **2010**, *5*, 206–226.

(136) Neale, Z. G.; Liu, C.; Cao, G. Effect of Synthesis PH and EDTA on Iron Hexacyanoferrate for Sodium-Ion Batteries. *Sustain. Energy Fuels* **2020**, *4* (6), 2884–2891. https://doi.org/10.1039/d0se00120a.

(137) Wang, W.; Gang, Y.; Hu, Z.; Yan, Z.; Li, W.; Li, Y.; Gu, Q. F.; Wang, Z.; Chou, S. L.; Liu, H. K.; Dou, S. X. Reversible Structural Evolution of Sodium-Rich Rhombohedral Prussian Blue for Sodium-Ion Batteries. *Nat. Commun.* **2020**, *11* (1), 1–9. https://doi.org/10.1038/s41467-020-14444-4.

(138) Brant, W. R.; Mogensen, R.; Colbin, S.; Ojwang, D. O.; Schmid, S.; Häggström, L.; Ericsson, T.; Jaworski, A.; Pell, A. J.; Younesi, R. Selective Control of Composition in Prussian White for Enhanced Material Properties. *Chem. Mater.* **2019**, *31* (18), 7203–7211. https://doi.org/10.1021/acs.chemmater.9b01494.

(139) Wessells, C. D.; Peddada, S. V.; McDowell, M. T.; Huggins, R. A.; Cui, Y. The Effect of Insertion Species on Nanostructured Open Framework Hexacyanoferrate Battery Electrodes. *J. Electrochem. Soc.* **2011**, *159* (2), A98–A103. https://doi.org/10.1149/2.060202jes.

(140) Mullaliu, A.; Gaboardi, M.; Plaisier, J. R.; Passerini, S.; Giorgetti, M. Lattice

Compensation to Jahn-Teller Distortion in Na-Rich Manganese Hexacyanoferrate for Li-Ion Storage: An Operando Study. *ACS Appl. Energy Mater.* **2020**, *3* (6), 5728–5733. https://doi.org/10.1021/acsaem.0c00669.

(141) Bersuker, I. B. *The Jahn–Teller Effect*; 2006. https://doi.org/10.1017/CBO9780511524769.

(142) Gnanavel, M.; Lebedev, O. I.; Bazin, P.; Raveau, B.; Pralong, V. Reversible Transformation from Amorphouse Na3Fe3(SO4)2(OH)6 to Crystallized NaFe3(SO4)2(OH)6 Jarosite-Type Hydroxysulfate. *Solid State Ionics* **2015**. https://doi.org/10.1016/j.ssi.2015.05.013.

(143) Dutrizac, J. E.; Chen, T. T. The Behaviour of Scandium, Yttrium and Uranium during Jarosite Precipitation. *Hydrometallurgy* **2009**, *98* (1–2), 128–135. https://doi.org/10.1016/j.hydromet.2009.04.009.

(144) Jambor, J. L. Nomenclature of the Alunite Supergroup. *Can. Mineral.* **1999**.

(145) Chang, L.; Wang, Y.; Luo, S.; Liu, H.; Wang, Q. Carbothermal Reduction Preparation and Performance of LiFePO4/C by Using Ammonium Jarosite Extracted from Vanadium Slag as Iron Source. *Ionics (Kiel).* **2019**. https://doi.org/10.1007/s11581-019-03155-6.

(146) Moritomo, Y.; Urase, S.; Shibata, T. Enhanced Battery Performance in Manganese Hexacyanoferrate by Partial Substitution. *Electrochim. Acta* **2016**, *210*, 963–969. https://doi.org/10.1016/j.electacta.2016.05.205.